Final Report

Date of Report: *October 5, 2018*

Contract Number: *DTPH5614HCAP04*

Prepared for: *Dr. James Merritt, PHMSA-DOT*

Project Title: *Optimized Diagnosis and Prognosis for Impingement Failure of PA and PE Piping Materials*

Prepared by: *University of Colorado-Denver, Arizona State University*

Contact Information: *Dr. Yiming Deng and Dr. Yongming Liu*

Project ending date: *September 29, 2018*

Acknowledgements

The work is sponsored by DOT-PHMSA CAAP program (Program Officer: Joshua Arnold，James Prothro, and James Merritt) and the financial support is greatly appreciated. Technical inputs from GTI research experts, Ernest Lever and Daniel Ersoy, is highly appreciated as well

ABSTRACT

The pipeline infrastructure is vital to the economic welfare of the United States. The pipeline systems which have been laid down for decades such as those installed in the early 1900's are still in use, however, a reliable database reporting the mechanical properties, and information about manufacturing and installation is often unavailable, which raises a concern for their safety and integrity. Therefore, an accurate estimation of the pipe material properties is crucial for the integrity and risk assessment of aging pipeline infrastructure systems. The various gaps that thus exist in pipe properties measurement create a desire for development of novel methods and techniques to better characterize the pipe material properties, which provides the impetus for the present research work. The main objective of this project work is the design of a Bayesian Network integrated model for probabilistic strength prediction by fusing information from the multimodal diagnosis of the pipe material properties. A multimodal diagnosis is performed by assessing the mechanical property variation within the pipe in terms of material property measurements, such as microstructure, composition, hardness etc. through experimental analysis, which are then integrated with the Bayesian network model that uses a Markov chain Monte Carlo (MCMC) algorithm. Simulation and prototype testing are carried out for model verification, validation and demonstration. Another major component of the study is the development of a novel Magnetic Barkhausen Noise (MBN) signal is which is sensitive to the multi-properties of ferromagnetic materials such as grain size, composition and thus aids in material property characterization of the pipes. The relationship between the number of turns of pick-up coils and MBN signals in both time-domain and frequency domain is studied for the sensor coil optimization and the results are validated using a Monte Carlo method. The next aspect of the research dwells into the fatigue properties of the pipe specimen to provide a holistic measure of performance of a material in service by studying the variation in the crack growth rate (da/dN) along the pipe wall thickness direction and its relation to the microstructure, material constants for the crack growth have been reported. Next, some well-known statistical models have been employed for the prediction of process parameters of the manufacturing process such as the TMCP to obtain the desired material properties. Lastly, a physics based 3D stochastic reconstruction model is proposed as a part of the scope for future work to obtain a direct and non-destructive way to obtain the elastic and plastic properties. Discussions are provided on the observations and future work.

INTRODUCTION

The present system of natural gas pipelines in the United States comprises of a network of gathering and transmission lines with more than 210 pipeline systems laid across 305000 miles [1]. Pipeline infrastructure forms a vital aspect in improving the U.S. economy and standard of living. Most of the pipelines were installed in the early 1900's and do not have a widely available database on manufacturing & installation, inspection as well as for the mechanical properties. Testing for the aging pipe strength and toughness estimation without interrupting the transmission and operations thus becomes important. The state state-of-the-art techniques for the prediction of pipe strength and other properties often involve destructive testing, those that are non-destructive tend to focus on the single modality deterministic estimation of pipe strength and do not account for inhomogeneity and uncertainties, which form the key gaps existing methods of mechanical properties estimation. The motivation and the main focus of this research work is to develop a methodology to aid in the accurate prediction of pipe strength and consequently the maximum allowable operating pressure. This is a collaborative study by Arizona State University (ASU) and Michigan State University (MSU).

Arizona State University (ASU) focuses on the Bayesian network model formulation and experimental testing for the material properties through SEM, EDS, EBSD, Hardness Tester, Tensile/ Fatigue test machines etc. The study proposes a probabilistic approach with rigorous uncertainty quantification, based on multimodal diagnosis to infer the strength of aging pipeline materials. The methodology involves using Bayesian network as a general information fusion framework, to derive the statistical inference and incorporate the multimodal measurements such as microstructure, chemical composition, and acoustic properties. The research work also looks into exploiting the already existing database using some popular statistical models to predict the process parameters of the manufacturing process such as the TMCP to obtain the desired material properties. Such methods are expected to aid in reducing the complexity of the problems and save some computational costs, improving the quality standards at the same time. Next, the fatigue crack growth behavior of pipe steels is investigated to assess the variation in the crack growth parameters through the pipe wall thickness which forms the final part of the report. The objectives of the present research from ASU are:

a. Development of a novel Bayesian network tool for information fusion from multimodality diagnosis results for the probabilistic pipe strength and toughness estimation (Chapter 1)

- Experimental testing and data analysis of material mechanical property variation with respect to basic chemical and metallurgical properties.
- Development of an information fusion methodology based on Bayesian network inference using multimodality diagnosis and demonstration study using representative pipe specimens.

b. Comparative study of statistical models for manufacturing properties prediction (Chapter 2)

- Prediction using individual models of multivariate linear regression, ML-KNN (multi-label k-nearest neighbor) and GP (Gaussian Process) model.
- Analyzing the effect of model parameter variation on the prediction efficiency.
- Demonstration of a model selection procedure depending on the length and quality of the dataset.

c. Investigation of variation in the fatigue behavior of the steels through the thickness of the pipe sample (Chapter 3)

- Estimation of crack growth characteristics of the pipe samples in relation to the microstructure.
- Investigation of variation in fatigue crack growth parameters through the pipe thickness.

As an expansion and future scope to the research work, Physics based 3D stochastic reconstruction model is proposed. This will aim to provide us with nondestructive means of estimating the macroscopic properties; transport, electromagnetic, and mechanical etc. This integrated computational framework will be independent of the data volume, saving time and providing with sound confidence bounds.

MSU focuses on experimental testing and data analysis to understand the chemical, microstructure of the pipe steel materials through measurement of materials' mechanical, elastic and micromagnetic properties, and prototyping for nonlinear and inhomogeneous acoustic and micro-electromagnetic properties of pipe material. The study employs a multi-modality approach to correlate material mechanical property, chemical properties, metallurgical properties, acoustic and micro-electromagnetic properties. A high-resolution scanning system that capable of imaging different defect profiles using both amplitude and phase information of the reflected signals has been developed and optimized. The method was tested on various datasets with successful implementation of signal recovery using numerical optimization. A multi-modal correlation analysis between mechanical and electromagnetic properties is studied as a potential in-situ & ex-situ application of the system. The results show that the developed system provides good correlation, which demonstrates this fast, non-contact method as a promising alternate modality. A Magnetic Barkhausen Noise(MBN) system has been developed to characterize the microstructure of the sample. Sensor optimization has also been studied. The coils with the different number of turns have been compared for sensitivity. For the optimization for the magnetic core, NSGA III has been introduced and applied to design the sensor with small size, high magnetic field, and suit for different diameter pipelines. MBN are investigated for various mild steels with different microstructure such as grain sizes and carbon contents. With different heat treatment, the samples with different hardness have also been evaluated.

The objectives of the present research from MSU are:

a. Development and optimization of a Microwave Imaging system (Chapter 3)

- Multi-channel sensor design and prototyping
- Rapid data acquisition method and Compressive Sensing method to improve the accuracy and speed of the scanning
- Experiment and simulation of the multi-modality approach to estimate the material's mechanical properties using its electromagnetic properties

b. Development and optimization of a Magnetic Barkhausen Noise system for the material's microstructure characterization (Chapter 2)

- Magnetic Barkhausen Noise system design and prototyping
- Sensor optimization using NSGA method
- Experiment and simulation study of the MBN signal on samples with different microstructures

Estimation and prediction of the materials' properties such as grain size, carbon content and hardness using MBN signal

ASU Contributions

CHAPTER 1: BAYESIAN NETWORK TOOL FOR INFORMATION FUSION FROM MULTIMODALITY DIAGNOSIS RESULTS FOR THE PROBABILISTIC PIPE STRENGTH ESTIMATION

Introduction

In the present work, a methodology for better prediction of mechanical properties for in-situ Natural gas pipeline systems has been proposed. The current in-line inspection techniques such as Smart PIGs (Pipeline Inspection Gauge) use non-destructive evaluation methods such as magnetic, ultrasonic etc. [2] for assessing the condition of a pipeline to identify defects in the form of mechanical dents, corrosion, cracks etc. However, in order to ensure correct responsiveness of the pipe to these defects, to be able to characterize the pipeline for the remaining life and the pressure rating, it is necessary to have a good estimate of the mechanical properties such as yield and tensile strength. As per the American Petroleum Institute (API) standards, the maximum allowable operating pressure (MAOP) can be directly related to the minimum yield strength, and the ratio specification of yield to tensile strength [3], whereas, many studies can correlate the shape and size of the defects to the remaining useful life of the pipelines [4]. In the present day, about 63 percent of these systems cannot be inspected via conventional PIGs due to them being either too old, or with turns and twists not allowing PIGs to operate in them [5]. A reliable estimate of the strength and remaining life of the pipelines is therefore often difficult to obtain. The techniques for estimation of pipe strength and toughness, such as the hardness testers, Automated Ball Indenter, [6] and others, rely on surface-based measurement of hardness and stress-strain measurements etc. Unlike the hardness-based strength estimation method, no ASME (American Society of Mechanical Engineers) standards exist for the ABI measurement method for pipe strength and toughness estimation [9]. Moreover, the Nondestructive evaluation (NDE) techniques such as acoustic [10], micro-magnetic [11], acoustic emission [12] etc. predict the mechanical properties based on single modality measurements[13]. The magnetic flux leakage technique, eddy current inspection, and ultrasound inspection are all based on analysis of the distorted signal pattern around the defect and are limited by the pipe wall thickness and the flaw size [14]. Although some NDE techniques like Magnetic Flux Leakage have shown the capability to be able to correlate with hardness, and correspondingly with strengths, there is a large uncertainty in such type of estimation which, on one hand, may work well for some systems and not for others [15]. The above-listed techniques predict the strength based on the assumption that the material is homogenous, and do not provide a holistic measure of the properties. For the pipeline systems, a number of factors could contribute to the presence of material inhomogeneities, such as the manufacturing process or structure changes due to strain aging may due to the long-term operation of pipelines [16]. This may initiate a phenomenon such as decarburization, resulting in a varied chemical composition and deterioration in mechanical properties that would finally cause surface properties to be different from the bulk ones [9]. Uncertainties in the system are another gap in the prediction of the mechanical properties[17]. These can manifest in terms of material properties, pipe geometries, manufacturing process, operational conditions, etc. Therefore, it is well understood that single modality analysis, not accounting for material inhomogeneity and the various uncertainties are the major gaps in the estimation of mechanical properties from the existing methods [9] [18].

Therefore, the focus of this task is on the rigorous information fusion framework with various identified features from multimodality diagnosis results as all of them contain certain amount of

valuable information which will be integrated here to obtain a more accurate prediction of pipe strength. The experimental procedure will consist of laboratory testing to investigate the material properties through the thickness of the pipe, namely chemical composition through EDS, microstructure through Optical microscope/ SEM, hardness through Vickers Hardness Tester and the tensile and fatigue properties through the Servo-hydraulic testing machine for the different grades of pipe steel, to specify them as the input parameters for the Bayesian Network model for prediction and validation of mechanical properties. This model will be based on an updating principle based on Bayes' theorem. This provides a statistical rigorous way to infer posterior distribution (i.e., fused or updated information) using prior distribution (i.e., existing information or experiences) and likelihood function (i.e., new measurements). Let M be a Bayesian model class and $p(\theta, M)$ denote the prior distribution of the parameter θ in the model. Then, for a new observed evidence or system response x' , the posterior distribution, $q(\theta, M)$ is given as:

$$q(\theta, M) \propto p(x' | \theta, \mathrm{M})\, \mathrm{p}(\theta, \mathrm{M}) \tag{1.2}$$

Here, $p(x' | \theta, \mathrm{M})$ is referred to as likelihood function of θ. The updated probability of each model in M is given by the posterior PDF when the new information x' is incorporated[26]. The present model also includes an error term e which is a variable with 0 mean normal distribution which can be denoted as $e \sim N(0, \sigma_e)$ and is used to define the relationship between the model M and the updating variable x' for updating the parameter, θ, giving us with the following relation:

$$x' = \mathrm{M} + e$$

The above shown information fusion is for a single modality/source of information. One major task in the study is to extend this idea to a generalized Bayesian network for multimodality diagnosis information fusion. A Bayesian network is a probability-based graphic tool to infer systems with stochastic parameters. A schematic of the proposed network is illustrated in Fig. 7 for the pipe strength and toughness estimation.

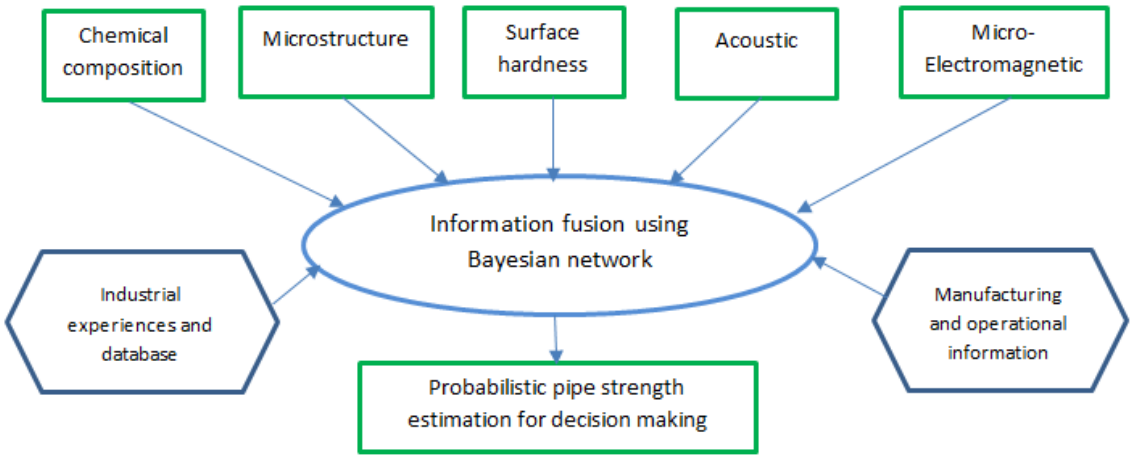

Fig. 1 Schematic of the proposed Bayesian Network model

2.1 Investigation and analysis of basic material properties:

Setup and Procedure

Microstructure Characterization:

For the experimental analysis, a few samples were carved out along the thickness direction 10 um^2 cross-section units and polished as per the guidelines for metallographic inspection. Etching was done using 2% Nital solution, holding the samples for 10-20 seconds to reveal the grain and phase structures. The samples were viewed under Optical/Scanning Electron Microscope (SEM). Grain size of ferrite was studied along with the volume fraction of the constituent phases with the use of a commercially available software ImageJ.

Chemical composition analysis:

The chemical composition of the specimen was studied through semi-quantitative Energy Dispersive Spectroscopy (EDS) in an Electron probe micro analyzer (EPMA). Both point analysis and area analysis was carried out to determine the average composition across the phases. Polished and etched samples from microstructure analysis were used for composition testing. Fig.3 shows the spot analysis SEM image and spectrum.

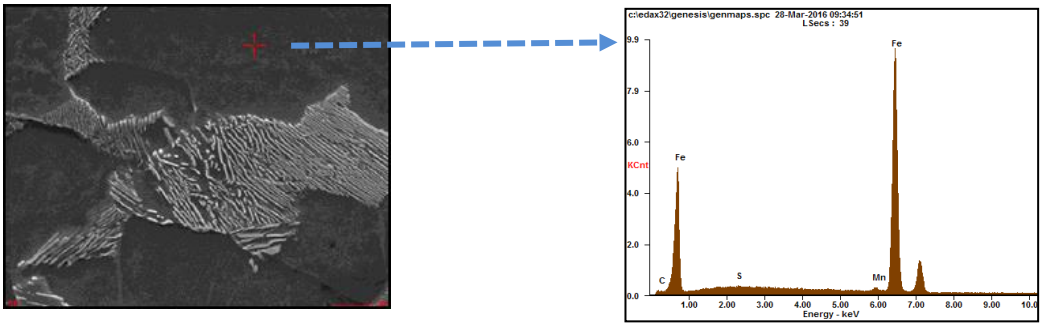

a) b)

Fig. 2 Images of the EDS analysis: a) SEM image b) EDS Spectrum

Hardness Test

Hardness of the samples were examined with the Vickers Hardness tester, a tester for small area measurements [9]. 1kg small load was used for the purpose of testing as the samples were only 1mm thick. Blocks of 10mm X 10mm X 1mm were used for the experiment.

Tensile Test

The stress-strain characteristics were studied through tensile tests of flat strip test samples carved out from the pipe in the hoop orientation (Fig.4 a, b) [7]. The samples were tested both with the use of a Tensile Stage machine (along layers) and Servo-Hydraulic MTS machine(Fig.4 c), (bulk analysis), and were custom made in as per the dimensions allowed by the machines.

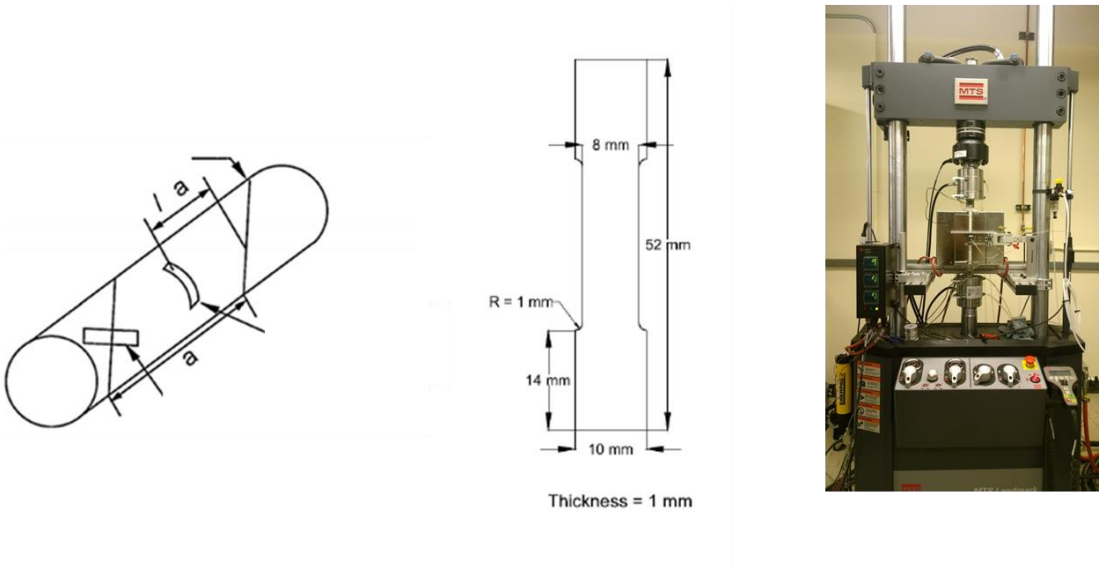

a) b) c)

Fig. 3 a) Orientation of flat strip tensile specimen within the pipe sample [7], b) Dimensions of flat strip tensile specimen c) Servo Hydraulic MTS machine

The experiments were repeated for different depths along the pipe wall thickness in order to examine their variation along the thickness. The thickness at different depths was measured using an Ultrasonic thickness gauge.

Results from the experimental analysis

Two samples from transmission pipelines were used in the present study belonging to the year of installation ranging from 1949 to1961. The pipe samples arrived with the installation year and Pipe grade information. The suspected grade and microstructure were deduced from the image analysis and year of installation information.

Table 1: Pipe grades information

Pipe Number	Installation year	Pipe grade	Suspected grade	Suspected microstructures
45 (1)	1949	1525	X50	FERRITE - PEARLITE
47 (2)	1964	1025	X60	FERRITE – PEARLITE
44 (3)	-	1513	-	-

2.1.1 Microstructure

The microstructure of the two pipe samples was studied through Secondary Electron Microscope and is reported in Fig. 5. The microstructure was seen to be comprised to two phases, ferrite and pearlite, hence the likelihood model in the network takes into account effect of dual phase strength.

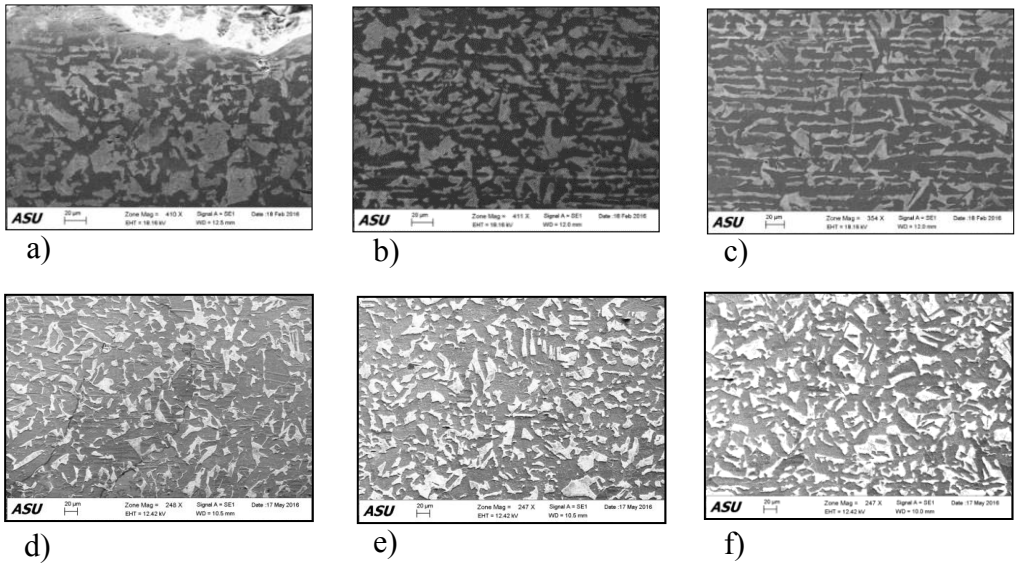

Fig. 4 Figure showing dual phase microstructure along the thickness direction, a), b) and c) are the images from successive depths of Pipe 45 and d), e) and f) are the images from successive depths of Pipe 47

The figures from left to right correspond to the different depths (along the pipe wall direction) within a sample; and are only shown for three consecutive depths.

Next are the micrographs from pipe 44, presented below:

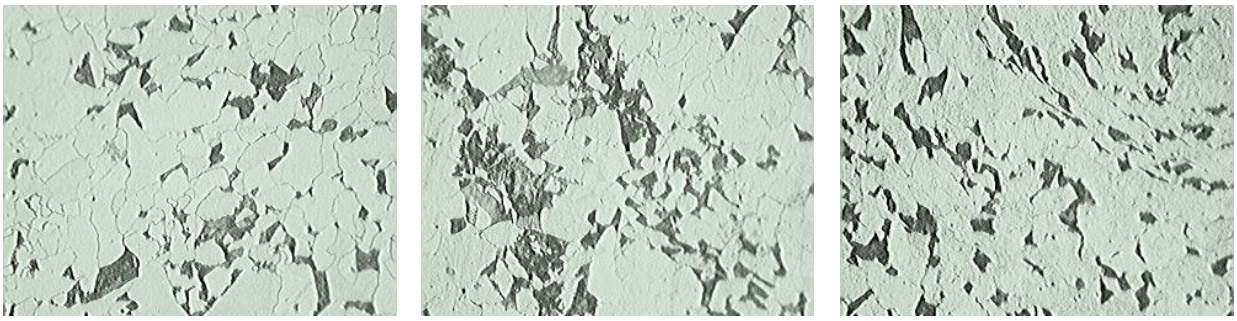

a) Edge 1 b) Edge 2 d) Edge 4

Fig.5.1 Optical images showing the microstructure of Pipe 44; a) Outer pipe wall surface b) Middle surface 1 c) Middle surface 2 d) Inner pipe wall surface

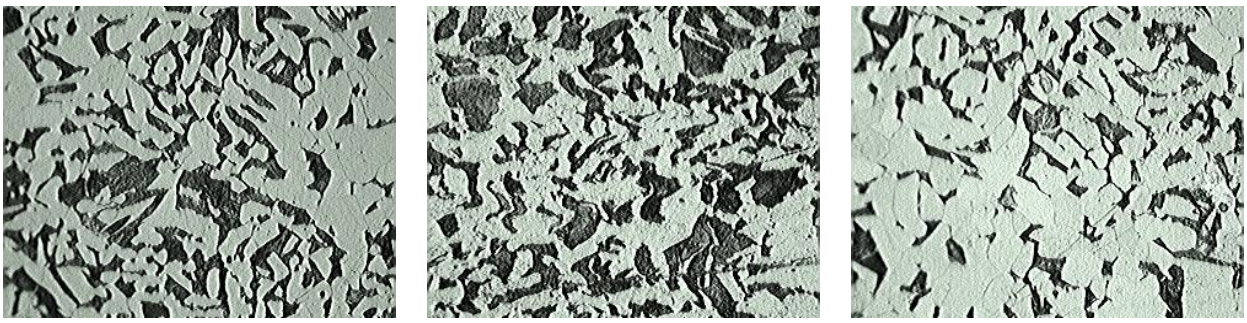

a) Edge 1 b) Edge 2 c) Edge 3

Fig.5.2 Optical images showing the microstructure of Pipe 32; a) Outer pipe wall surface b) Middle surface c) Inner pipe wall surface

These pipe images from pipe 44 and pipe 32 depict a very obvious texture, potentially manufacturing process related. Fine grains can also be observed from both the pipe samples that would aid in studying the grain size and volume fraction. These are used to derive the volume fraction of the constituent phases as well as the grain size, as presented below.

2.1.1 Volume fraction of the phases:

The complete analysis was done for the distribution of phases in terms of the volume fraction with use of image analysis software Image J, as stated previously. The result is shown below in Fig. 6; overlapped for comparison.

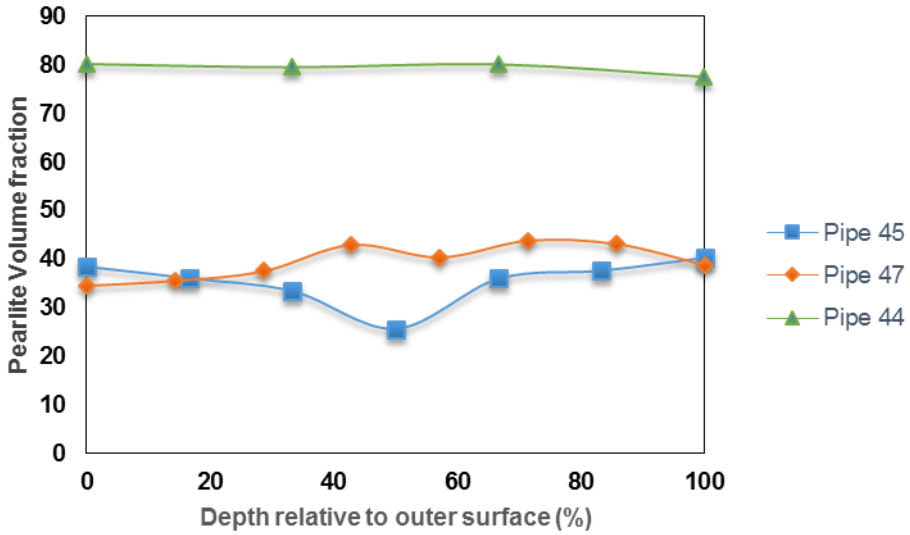

Fig. 6 Plot showing change in the pearlite content across the pipe wall thickness

The number of measurements for each pipe specimen are limited by the thickness of the specific pipes. Therefore, the depth is listed as a function of overall thickness in Fig. 4, considering pipe sample 1 was about 8mm thick while pipe sample 2 was only 5.5mm in thickness. A total of 7-8 measurements were taken per sample. The figure shows the variation in the phase volume fraction with increasing depth from the surface. Pipe 1 shows a decrease in the pearlite content in the middle region, whereas Pipe 2 shows a slight opposite behavior where the pearlite content being higher in the middle region and lower towards the surface. Pipe 3 shows a constant higher percentage of pearlite though the entire thickness. The predicted trend and the cause of variation is out of the scope of the study and hence not presented in detail here, instead the quantitative values along the thickness are used as input in the Bayesian Model.

2.1.3 Ferrite Grain Size

Grain size analysis was done for the samples using the lineal intercept procedure as per the ASTM standards [7]. The measurements were done for each layer from outside to inside surface. The

average grain size for both samples was observed to be 24um for the first two samples, and 19 um for the Pipe 44. The observed values are listed below:

Table 2: Grain size details for pipe 45, 47 and 44 and 32 :

S.No	Pipe 45		Pipe 47	
	Layers	Grain Size (um)	Layers	Grain size (um)
1	Outer region	22.86	Outer region	24.13
2	Middle region-1	21.8	Middle region-1	20.5
3	Middle region-2	25.59	Middle region-2	27.44
4	Inner region	27.69	Inner region	25.4

S.No	Pipe 44		Pipe 32	
	Layers		Layers	Grain size (um)
1	Outer region	1	Outer region	17.4
2	Middle region-1	2	Middle region	16.9
3	Middle region-2	3	Inner region	16.66
4	Inner region	4		

The grain sizes for Pipe 45 and 47 seem to show a little increase towards the inner region, probably due to differential cooling during the manufacturing process. Pipe 44 appears to have smaller grain size at both surface zones and higher grain size in the middle regions, again asserting to the TMCP process and cooling process afterwards. The values are used for model training and prediction.

2.1.4 Chemical composition

The chemical constituent of the phases was analyzed using EDS, and was observed to be Ferrite + Pearlite system for all the specimens. The elements of interest were chosen based on their direct or indirect correlation to the Yield and Ultimate Tensile strengths, obtained from literature [27]. The primary elements of interest were found to be Fe, Mn, Si, and N.

Table 3a: Composition (weight percentage) of the pipe sample 45

Region	Elements					
	C	N	Si	Mn	Fe	Ni
Outer region	0.09	0.23	0.26	1.29	97.92	0.31
Middle region-1	0.06	0.12	0.04	1.19	98.29	0.17
Middle region-2	0.2	0.01	0.03	1.28	97.97	0.15
Inner region	0.15	-	0.06	1.23	98.13	0.16

Table 3b: Composition (weight percentage) of the pipe sample 47

Region	Elements					
	C	N	Si	Mn	Fe	Ni
Outer region	0.05	0.11	0.02	1.18	98.25	0.2

Middle region-1	0.21	-	0.01	0.89	98.69	0.05
Middle region-2	0.07	-	0.04	1.26	98.34	0.19
Inner region	0.08	0.02	0.02	0.93	98.66	0.23

Table 3c: Composition (weight percentage) of the pipe sample 44

Region	Elements						
	C	N	Si	Cr	Mn	Fe	Ni
Top Layer	-	-	0.23	0.04	1.77	95.42	-
Middle region-1	0.06	-	0.25	-	1.7	97.76	0.1
Middle region-2	-	-	0.27	0.05	1.8	97.41	0.11
Bottom layer	-	-	0.26	-	1.73	97.33	0.19

The composition for the elements of interest did not seem to vary too much along the thickness and therefore only the average values are listed here.

2.1.5 Hardness

Hardness was studied through Vickers Hardness Tester for two of the pipe specimen (1 & 2). The following tables show the results for the same for the two pipe samples; Outer region represents the outermost surface exposed to the surrounding going towards the thickness being represented by middle region 1 and 2, and inner region being the one towards the inner surface of the pipe. The results are reported for reference in the below tables:

Table 4 a): Hardness Specimen 1-Pipe 45 b): Hardness Specimen 2-Pipe 47

Samples	Mean Hardness (HV)	Samples	Mean Hardness (HV)
Outer region	220.2	**Outer region**	208.17
Middle region-1	178	**Middle region-1**	217.27
Middle region-2	203.06	**Middle region-2**	221.73
Inner region	219.3	**Inner region**	226.03

c): Hardness Specimen 3-Pipe 44

Samples	Mean Hardness (HV)
Outer region	188

Middle region-1	188.2
Middle region-2	206.5
Inner region	200

These values show that for pipe sample 45, the Hardness of the pipe walls, inside and outside is more than the middle regions. For pipe sample 47, the inside pipe wall appeared to have the highest hardness that correspondingly decreased towards the outer pipe wall surface. Pipe 44 appears to be stronger towards the inner regions. Although the trends observed are reported here, but they were not investigated being out of the scope of the paper, and only quantitative measures were used as input for the model.

2.1.6 Tensile Properties

The pipe specimen were tested using the Tensile-stage along the thickness, and the corresponding stress-strain curves were analyzed. The plots (Fig. 7) as well as the values of Yield and Tensile Strengths were extracted from the same, and are listed here.

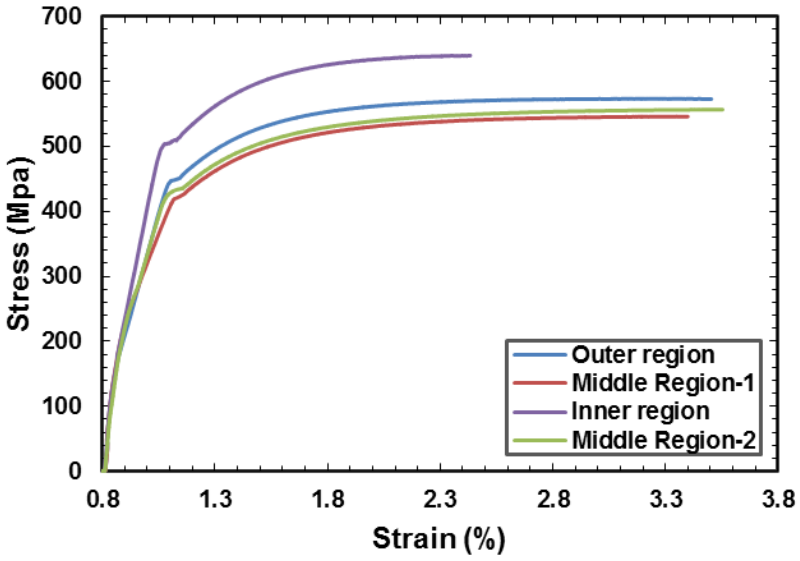

a)

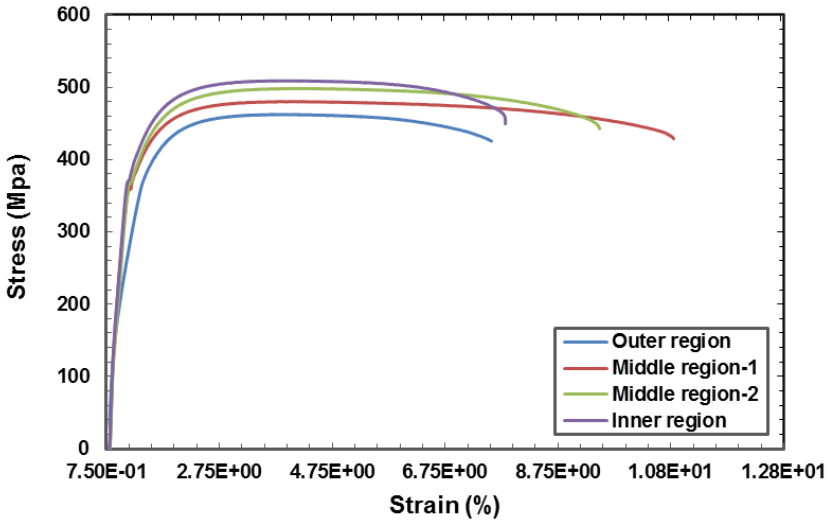
600
500
400
300
200
100
0
Stress (Mpa)
7.50E-01
2.75E+00
4.75E+00
6.75E+00
8.75E+00
1.08E+01
1.28E+01
Strain (%)
Outer region
Middle region-1
Middle region-2
Inner region

b)

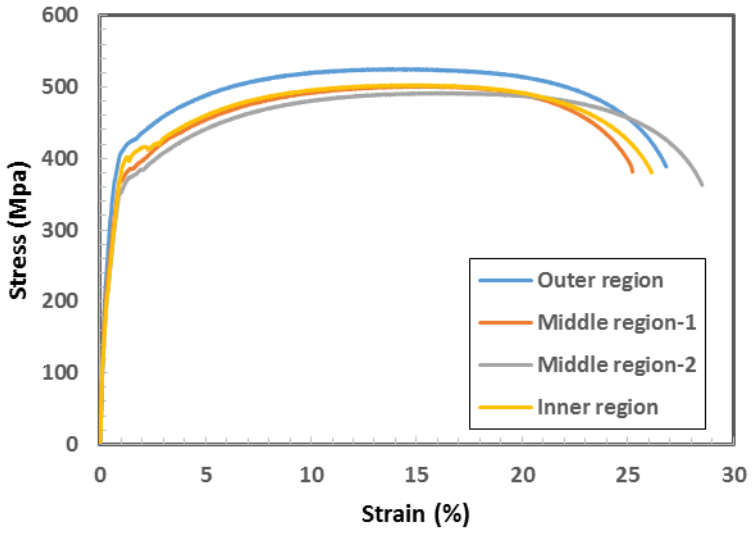
600
500
400
300
200
100
0
Stress (Mpa)
0
5
10
15
20
25
30
Strain (%)
Outer region
Middle region-1
Middle region-2
Inner region

c)

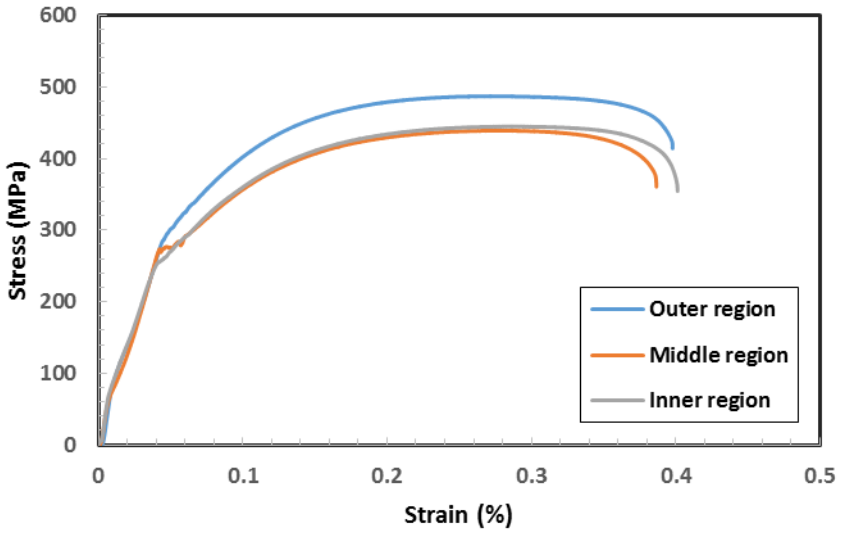

d)

Fig. 7 Plot showing stress-strain behavior a) Pipe 45 b) Pipe 47 c)Pipe 44 d) Pipe 32

Table 5 a): Stress-Strain data for Pipe 45

Samples	YS (MPa)	UTS (MPa)
S1(Top Layer)	450	572.99
S2(Layer 2)	425	538.4
S3(Layer 3)	435	555.6
S4(Layer 4)	506	637.5

Table 5 b): Stress-Strain data for Pipe 47

Samples	YS (MPa)	UTS (MPa)
S1(Top Layer)	355.5	462.2
S2(Layer 2)	358.4	479.4
S3(Layer 3)	366.2	497.8
S4(Layer 4)	371.08	508.4

Table 5 c): Stress-Strain data for Pipe 44

Samples	YS (MPa)	UTS (MPa)
S1(Top Layer)	406	524.2
S2(Layer 2)	373	500.4
S3(Layer 3)	367	489.6
S4(Layer 4)	397	501.5

Table 5 d): Stress-Strain data for Pipe 32

Samples	YS (MPa)	UTS (MPa)
S1(Top Layer)	274.8	486
S2(Layer 2)	268	444
S3(Layer 3)	261	444.4

Following the trend from the hardness study, the tensile properties of the two pipe specimens also showed similar behavior, appearing to be stronger on the pipe walls for pipe sample 1 and weaker on the inside. Also, for pipe sample 2, inside pipe wall seemed to be the strongest with middle regions being little weaker and the outermost pipe wall surface being the weakest. Once again, the reported trends are not investigated, but the values are used for model validation.

2.2 Bayesian Model formulation

2.2.1 Model formulation:

The yield strength or ultimate tensile strength of pipeline specimen in service can be estimated in several indirect ways, through measurement of surface material properties and correlating them to strength through available literature data [27][28][7]. The material properties such as hardness and composition can be obtained experimentally without interrupting the operation of the pipeline. The current model makes use of this data and the available relationships to fuse them together and provide a more precise multimodal prediction of strength[29][30]. The general model for yield strength prediction appears as follows, where YS prior is updated using data from Hardness, H, Chemical composition, C and Volume fraction, V. YS and σ_{ys} have been used interchangeably here.

$$p(YS \mid H,C,V,\mathrm{M}) \propto p(H,C,V \mid YS,\mathrm{M})p(YS,\mathrm{M}) \tag{0.1}$$

where, $\mathrm{p}(YS \mid H,C,V,\mathrm{M})$ is the posterior yield strength, $p(YS,\mathrm{M})$ is the prior yield strength, and $p(H,C,V \mid YS,\mathrm{M})$ is the likelihood function in the model. To start with, each of these nodes have been provided equal weightage, which can be modified later with a sensitivity analysis approach, currently outside the scope of this paper. More formally, the likelihood model of YS is given as,

$$l(\sigma_{YS}) = \mathrm{A}(\sigma_{H|YS}) + \mathrm{B}(\sigma_{C|YS}) + \mathrm{C}(\sigma_{V|YS}) \tag{0.2}$$

where, $l(\sigma_{YS})$ is the likelihood model with $\sigma_{H|\mathrm{YS}}$ $\sigma_{C|YS}$ and $\sigma_{V|YS}$ as the individual yield strength values derived from Hardness, chemical composition and volume fraction, as stated above. Due to the equal weightage assignment, each of the coefficients A, B and C in the likelihood model are each equal to 1/3. Fig.8.1 depicts the general schematic of the model.

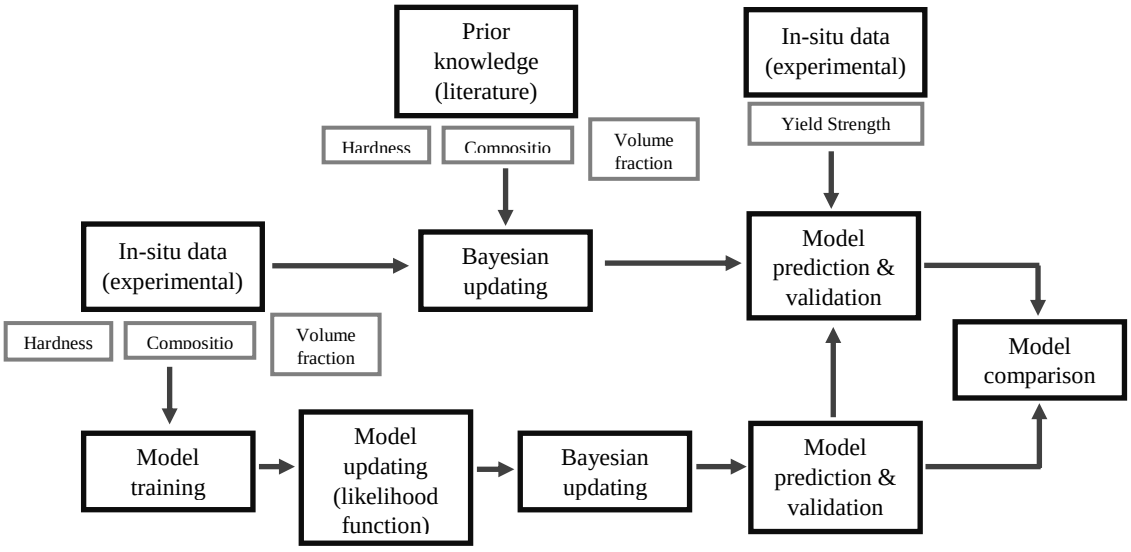

Fig.8.1 General flow of the model prediction and validation

Each of the individual relationships are described below.

The relationship between yield strength and material chemical composition as well as grain size is realized as follows:

$$\sigma_{YS|C} = 53.9 + 32.34(X_{Mn}) + 83.2(X_{Si}) + 354.2(X_{Nf}) + 17.4(d^{-1/2}) \quad [27] \qquad (0.3)$$

where, $\sigma_{YS|C}$ is the yield strength of the material derived from the compositional parameters, X_{Mn} is the weight percentage of Manganese, X_{Si} is the weight percentage of Silicon, X_{Nf} is the weight percentage of Nitrogen, and d is the grain size of ferrite (mm).

Similarly, for a two phase microstructure system, the overall yield strength is assumed as the weighted average of yield strength of the individual phases.

$$\sigma_{YS|V} = \sigma_{(f)}(V_f) + \sigma_{(p)}(1 - V_f) \quad [28] \qquad (0.4)$$

where, $\sigma_{YS|V}$ is the yield strength of the dual phase material derived from volume fraction alone, $\sigma_{(f)}$ is the yield strength of the ferrite phase and $\sigma_{(p)}$ is the yield strength of the pearlite phase and V_f is the volume fraction of ferrite.

Next, the yield strength of the low carbon steel is related to the hardness as:

$$\sigma_{YS|H} = 2 * H + 105 \quad [7] \qquad (0.5)$$

where, $\sigma_{YS|H}$ is the yield strength derived from Hardness, and H is Vickers hardness.

The material ultimate tensile strength also have similar relationships. The ultimate tensile strength is related to average chemical composition, volume fraction and grain size as follows:

$$\sigma_{UTS|C,V} = 294.1 + 27.7(X_{Mn}) + 83.2(X_{Si}) + 3.9(V_p) + 7.7(d^{-1/2}) \quad [27] \qquad (0.6)$$

where, $\sigma_{UTS|C,V}$ is the ultimate tensile strength derived from compositional and microstructural parameters, V_p is the volume fraction of pearlite, and the other symbols have the usual meanings.

Additionally, it is related to hardness as follows:

$$\sigma_{UTS|H} = 1.3 * H + 344 \quad [7] \qquad (0.7)$$

where, $\sigma_{UTS|H}$ is the ultimate tensile strength derived from Hardness and H is the Vickers hardness.

Known priors were used for each of these, derived from the literature knowledge of the system of API Steels with ferrite-pearlite microstructure [27][28][7]. The prior values (means) of the composition were given as; X_{Si} = 0.02 for weight percent of silicon, X_{Mn}=0.2 for weight percent manganese, X_{Nf} =0.02 as the weight percent of free nitrogen. Prior grain size, d was 10um, prior volume fraction of ferrite V_f was listed as 0.5 or 50% and prior Vickers hardness was assumed as 150 HV

The updating scheme makes use of Metropolis-Hastings algorithm to draw random samples form the probability distributions and perform updating by using the specified number of samples and allowing a margin for a burn-in period. All the priors and likelihoods follow a Gaussian distribution, for the purpose of simplicity and demonstration.

Strength prediction through Bayesian updating

The statistical averaging model for the yield strength being of the form as listed below:

$$YS = Ax + By + Cz + \varepsilon, \quad (0.8)$$

Where, x, y and z are pdfs representative of the equations (1.5), (1.6), (1.7), and ε is the random error component in the system, and A, B and C are the model coefficients corresponding to the variables. The resultant model is depicted in Fig. 8.2 YS and UTS represent the yield and ultimate tensile strength correspondingly.

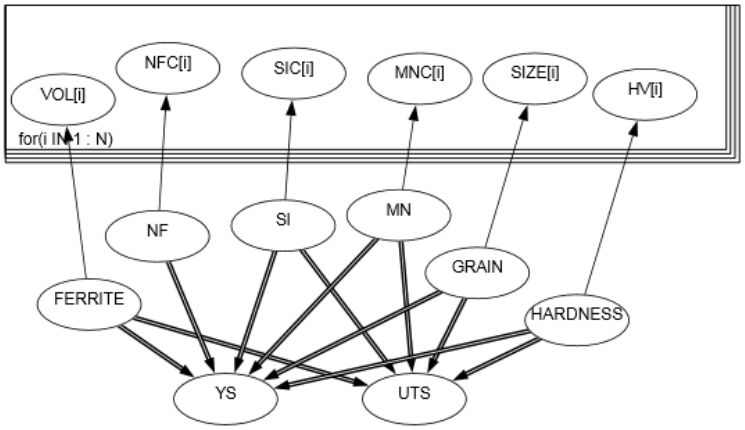

Fig. 8.2 Schematic representation of the Bayesian Network Model for Yield and Ultimate Strength prediction

The above model for prediction of yield and ultimate strength depicts several nodes. Node FERRITE refers to volume fraction of ferrite, NF, SI and MN are the compositional parameters referring to weight percentages of free Nitrogen content, Silicon, and Manganese. Node GRAIN refers to the grain size and HARDNESS refers to Hardness of the material. The nodes VOL[i], NFC[i], SIC[i], MNC[i], SIZE[i] and HV[i] are all used for updating the corresponding primary nodes FERRITE, NF, SI, MN, GRAIN and HARDNESS, respectively, when a new observation is available. The model offers several unique features that are not available in most existing methodologies. First, continuous uncertainty reduction can be achieved if continuous observation from multimodality measurements is available for the interested material system. Another natural and important outcome from the proposed model is the node sensitivity. The predicted response could be more sensitive to one or more of the interconnected nodes, compared to the others, and this dictates the weightage assigned to the nodes. This information will be valuable for future optimization of inspection (i.e., only focusing on more sensitive node for information acquisition). Detailed the discussion on this topic is beyond the scope of the proposed study and needs further investigation.

Another feature is that all the nodes in the model are co-dependent and updating can be performed in terms of data analysis for prediction as well as for the missing values, and hence all the nodes in the system can be updated, irrespective of a direct or indirect correlation with the updating node. This helps to converge the parameter values and quantifying the uncertainty of the system as the model is updated in the view of new information from various measurements.

The next section describes the experimental procedures utilized to gather data for performing training and validation of the Bayesian Network Model. The metrics analyzed here are the ones known to have a response in the present system, based on the equations (1.6) through (1.10).

2.2.2 Model Validation for Prediction of Strength

The present results as shown in Fig. 9 are for the different pipe samples. The input for the model are obtained from the data in Section 3, for the microstructure, hardness and composition, and are used to predict the corresponding Yield Strength and Ultimate Tensile Strength. The predictions are done for likelihood models with just one node for each of hardness, composition and volume fraction, as well as model with the nodes combined together as a weighted average, and are then compared to the actual experimental results from the tensile testing of the samples to measure the closeness of the predicted values with the experimental ones

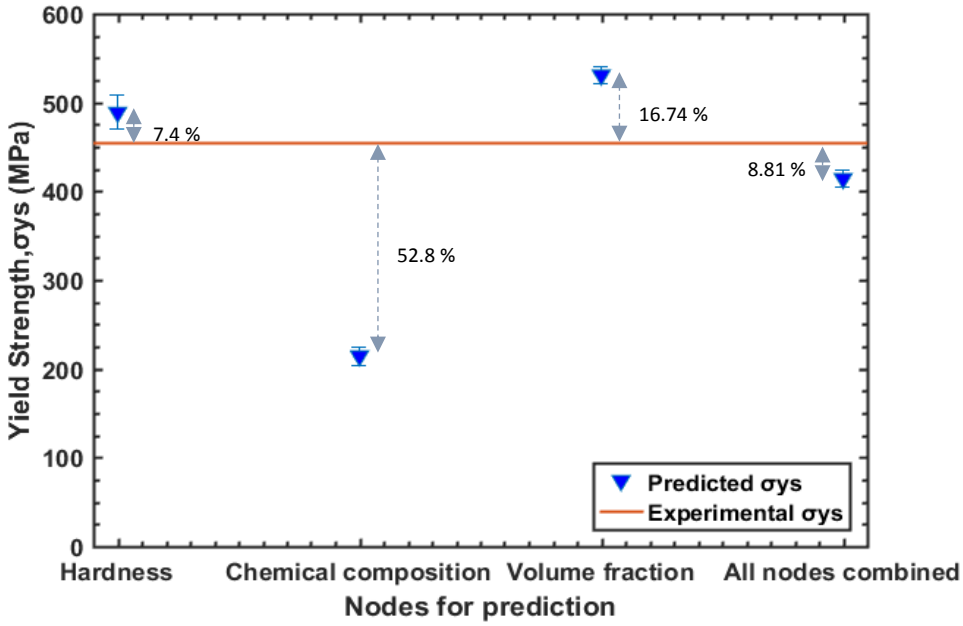

a)

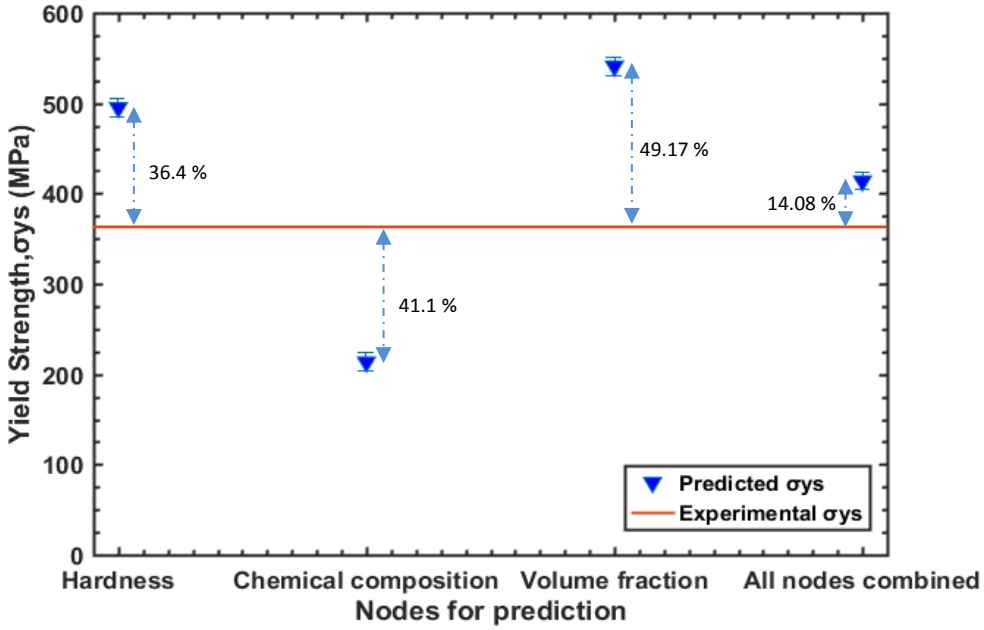

b)

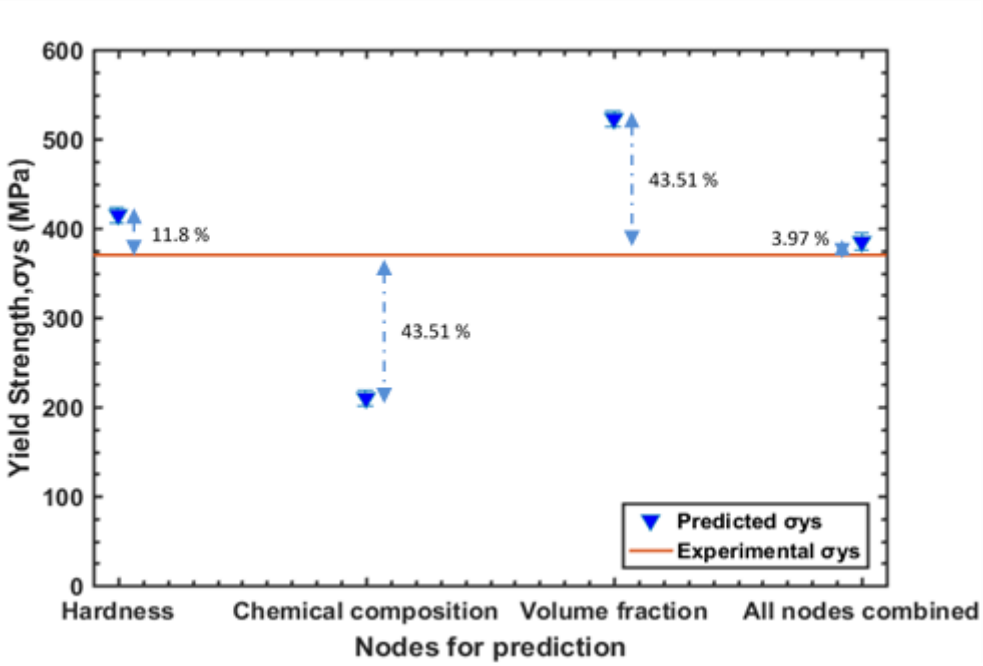
600
500
400
300
200
100
0
Yield Strength,σys (MPa)
11.8 %
43.51 %
43.51 %
3.97 %
Predicted σys
Experimental σys
Hardness
Chemical composition
Volume fraction
All nodes combined
Nodes for prediction

c)

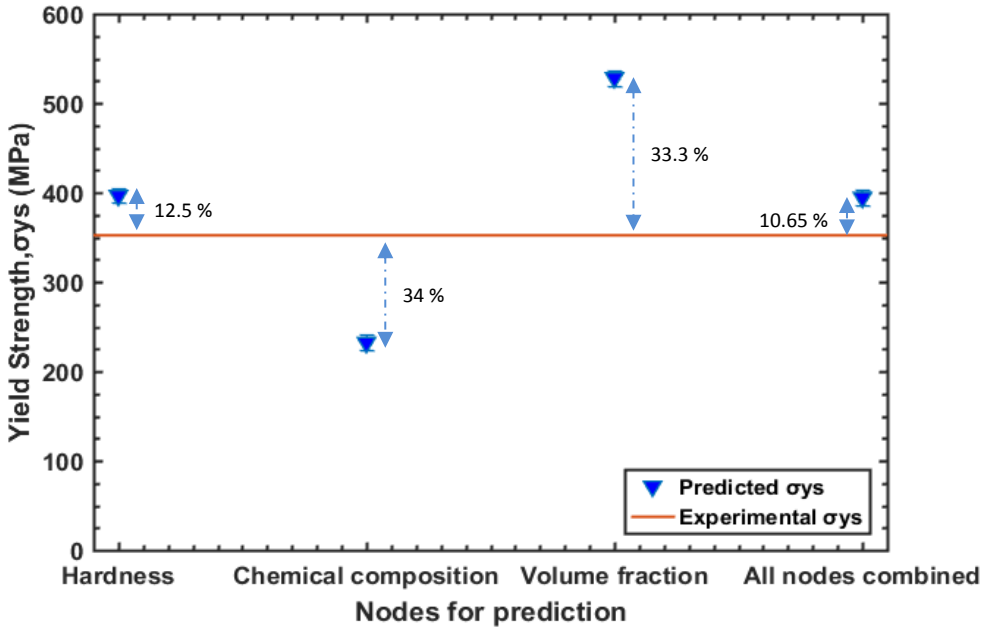
600
500
400
300
200
100
0
Yield Strength,σys (MPa)
12.5 %
33.3 %
34 %
10.65 %
Predicted σys
Experimental σys
Hardness
Chemical composition
Volume fraction
All nodes combined
Nodes for prediction

d)

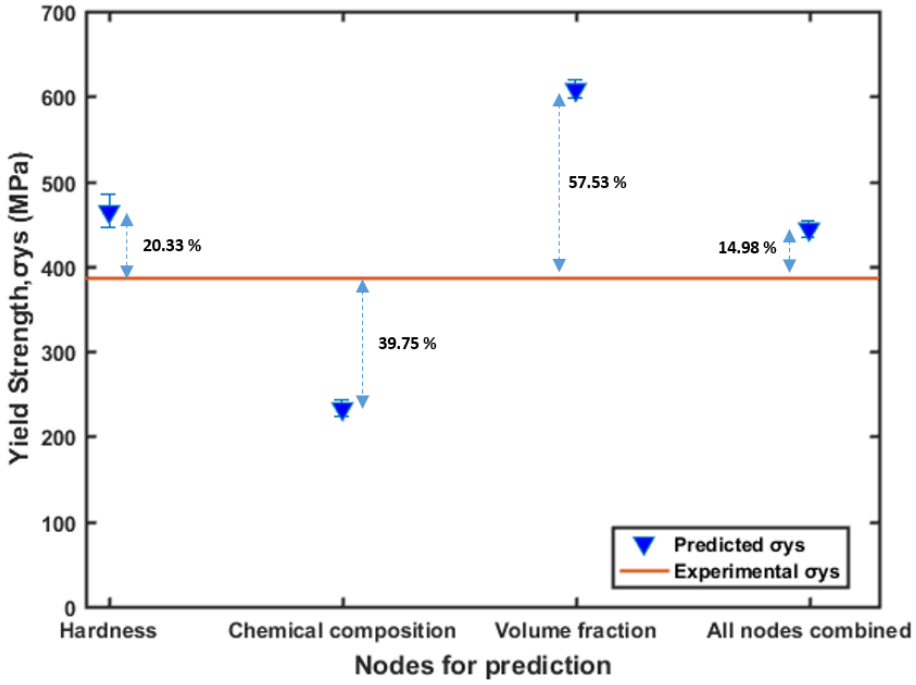

e)

Fig. 9 Plot for prediction of Yield strength from individual nodes as well as put together a) Pipe 45(1) b) Pipe 47(2) c) Pipe X42R d) Pipe X42N e) Pipe 44 (3)

For the first case a), it appears that prediction with node Hardness is 488.78, being 7.4% away from the experimental value of 454 and the best prediction, followed by prediction from all nodes combined being 414 or 8.81% away from the experimental value and prediction from chemical composition being the furthest away as 52.8%. For case b), the smallest deviation from true value was from all the nodes combined was 413.63, making it 14.08% from the true value of 362.79 and the largest one being 540.85 or 49.17% from node volume fraction.
For c), the prediction from all nodes combined was 394.3 MPa or 10.65% away from the experimental value of 352 MPa being the closest prediction, whereas prediction from node volume fraction was 528.38 MPa being the farthest away of 33.3%. For case d), once again, the prediction from all nodes combined was 384.69 being the closest to the true experimental value of 370 MPa in the range of 3.97% and the farthest prediction was shown by node chemical composition, resulting in a value of 209.66 MPa or 43.51% away from the true value.

2.2.3 Nodes codependency

The Bayesian Network features codependency of the nodes that may or may not be directly correlated. This is demonstrated by changing the updating value for node Hardness and observing a change in the posterior distribution of other nodes like Silicon and Ferrite, as depicted in Fig. 10.

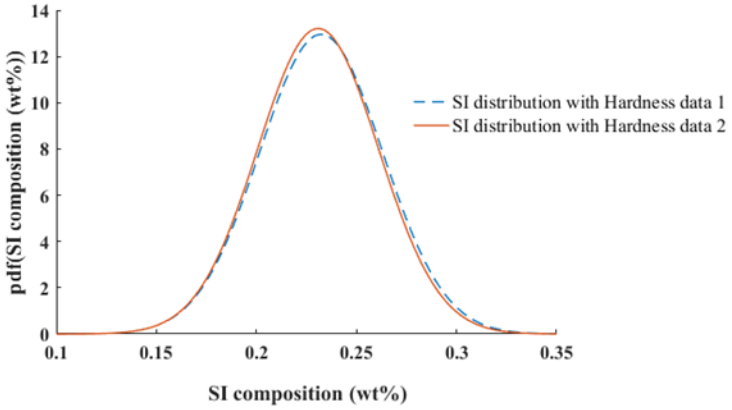

a)

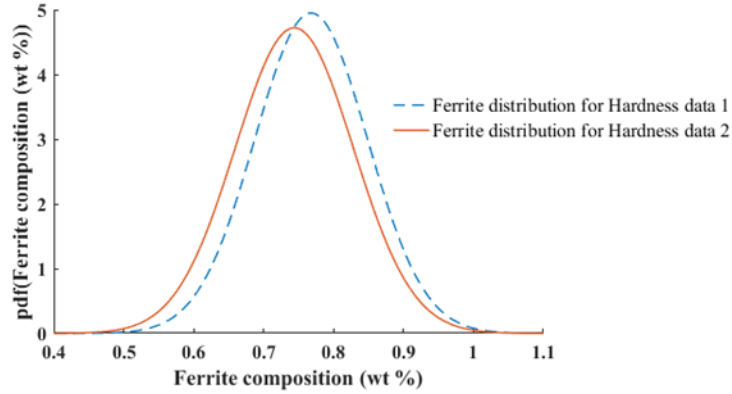

b)

Fig. 10 Ilustration of nodes co-dependency a) Change in node HARDNESS followed by a change in node SILICON b) Change in the node HARDNESS followed by change in the node FERRITE

The extent of change in the posterior densities of the nodes may differ, as can be seen from the above figures. This codependency can be useful in in order to derive (predict) missing information about one or more nodes, in an event such information is hard to obtain experimentally.

2.2.4 Model Regression Coefficients Verification

The various relationship between Yield Strength and material properties listed in the equations (1.5) through (1.10) were obtained from literature for different pipe systems pertaining to similar microstructure composition. As presented in section 4.1, these system of equations combined together predict a value of yield strength that can vary from 1.34 % to 14.01 % from the actual value of yield strength derived experimentally. Therefore, in an integrated form, these relationships may not be a holistic representative of the behavior of a particular system in view. In order to improve the prediction from the present Bayesian Network model, more information in terms of both data points and new metrics would have to be added in the model. Another way to improve prediction would be to update the relationship between yield strength and material properties derived from literature. This can be done by training the individual relationships with data for a specific system of pipes and then using the updated model coefficients for prediction. In this manner, if a complete data set (including tensile properties) is available for pipeline systems in a specific area, it could be used for training the present model coefficients and improving the

prediction of connected pipeline systems in a different region where destructive testing may not be available. In the present study, the data from X65 steels, obtained from literature [31], is used for a demonstration of the same. Data training and validation is performed by training the model and obtaining updated values of the model regression coefficients, and are validated by comparing the predictions of the tensile properties from both the initial and the updated model. The procedure of this study is listed below:

This study is done for the correlation of Yield Strength to Hardness, Composition and Volume fraction of Ferrite.

Original relation from literature:

$$\sigma_{YS} = (53.9 + 32.34(X_{Mn}) + 83.2(X_{Si}) + 354.2(X_{Nf}) + 17.4(d^{-1/2}) + \sigma_{(f)}(V_f) + \sigma_{(p)}(1\text{-}V_f) + 2*H + 105)/3 \quad (4.1)$$

Of the form $$YS = (a + b*X_{Mn} + c*X_{Si} + d*X_{Nf} + e*d^{-1/2} + f*V_f + g*H + \varepsilon)/3 \quad (4.2)$$

Where, $\varepsilon = N(0, \sigma^2)$, is a model error term.

In the general case, these coefficients based on the literature equation are reported as:

a = 158.9, b = 32.34,c = 83.2, d = 354.2, e = 17.4, f = , g = 2

Training of the model with the literature data for a system of X65 pipelines yielded the following results:

a =266.67, b= 28.46, c= 33.05, d= 162.33, e= 5, f= -8.67, g= 0.7

The two models were used to predict the yield strength for the other API X65 pipeline systems. The comparative prediction with the updated coefficients for the likelihood model are listed and shown with the help of Fig. 11 a) & b):

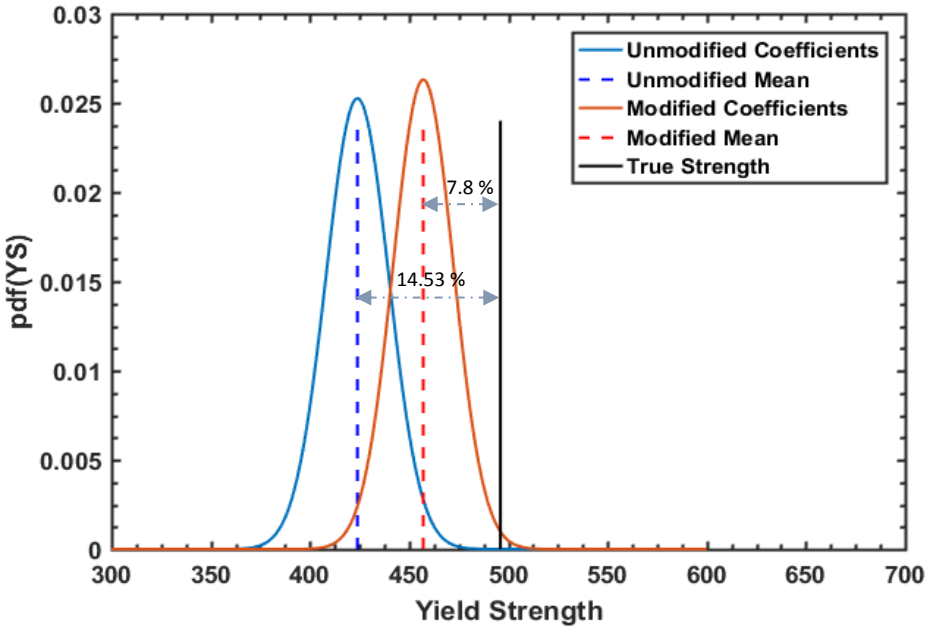

a)

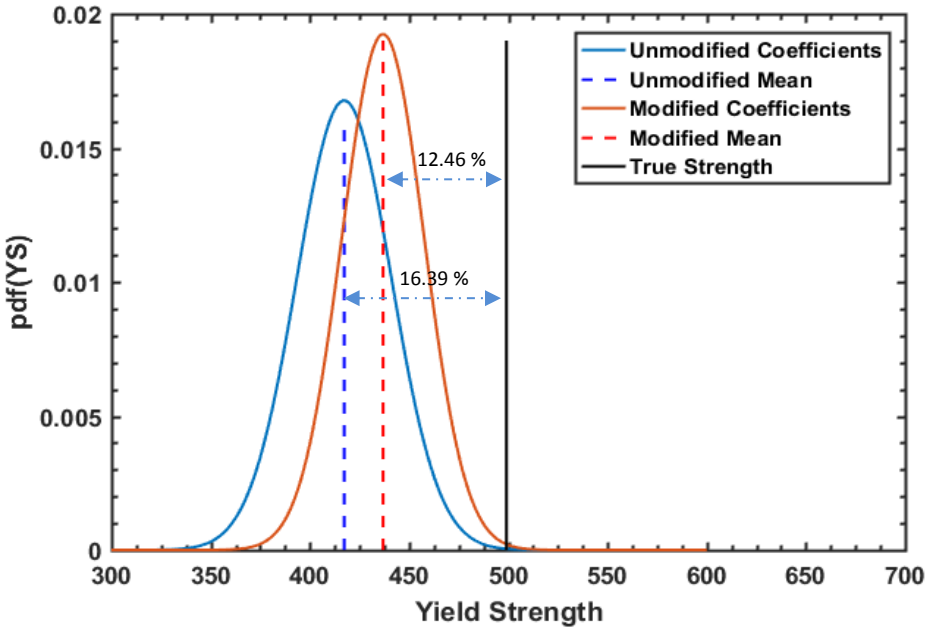

b)

Fig. 11 Plot showing Yield Strength vs pdf values with the original and modified coefficients for the two samples a) Pipe X65 1 b) Pipe X65 2

Similar training was conducted for the pipe sample 2, as the complete data set was already available as presented before in experimental analysis section. The pipe 2 had four samples extracted from the thickness direction, as stated previously, the data points from two of which were used for training and the remaining two were used for prediction from the updated values. The original relation and the form remained the same as listed in eqn (7) and (8). The updated coefficients from the training of pipe 2 are listed below:

a =688.7, b= 83.8, c= 913.6, d= 859.4, e= 15.48, f= 72.2, g= 1.31

Fig. 10 c) shows the improved prediction from the updated coefficients.

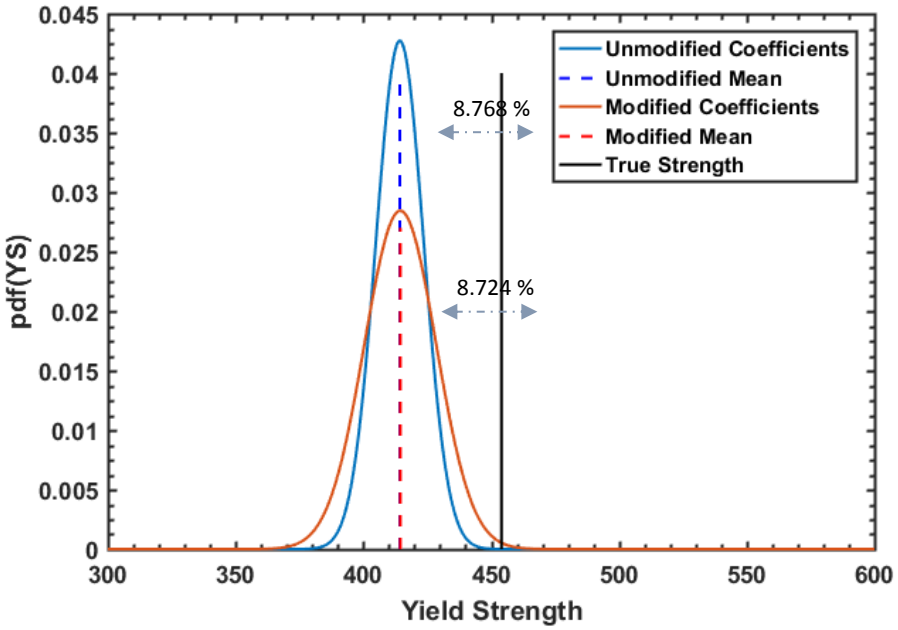

c)

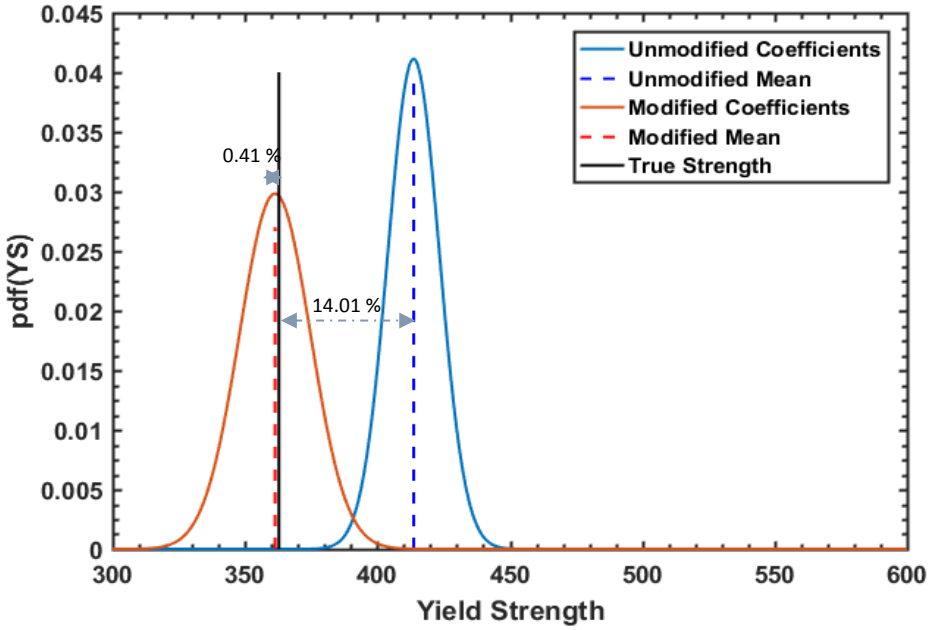

d)

Fig. 11 c) & d) Plot showing Yield Strength vs pdf values with the original and modified coefficients for the two samples c) Pipe 45 (1) d) Pipe 47 (2)

It can be seen that in all the three cases the prediction from the updated likelihood model shows a prediction value closer to the theoretical strength, and hence data training of the model can help improve prediction. It was also tested to predict the strength of other systems such as X52, X60 etc, but it was observed that the training for a particular system of pipelines is restricted to improve the prediction of the similar systems, and specific training needs to be performed for the other grades of the pipeline systems to improve their prediction.

2.2.5 Node Sensitivity

A parametric sensitivity analysis was carried out to test for the most influential factor governing the prediction of Yield Strength. Information on the nodes was varied by +/- 30%, one at a time, and corresponding variation in the predicted results was noted. Two literature data (X65, X42) and two experimental data (Pipe 45 & 47) have been used for the demonstration of the same. The results are presented below:

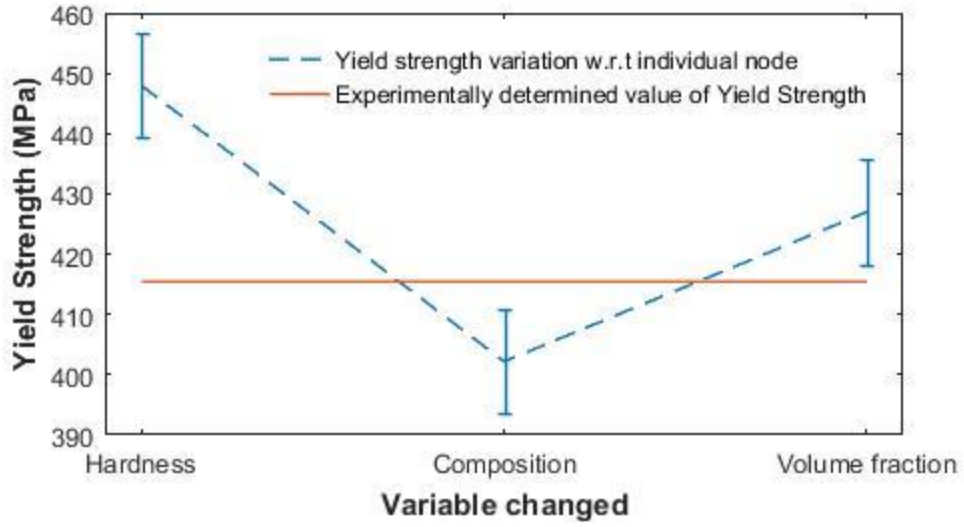

a) X45

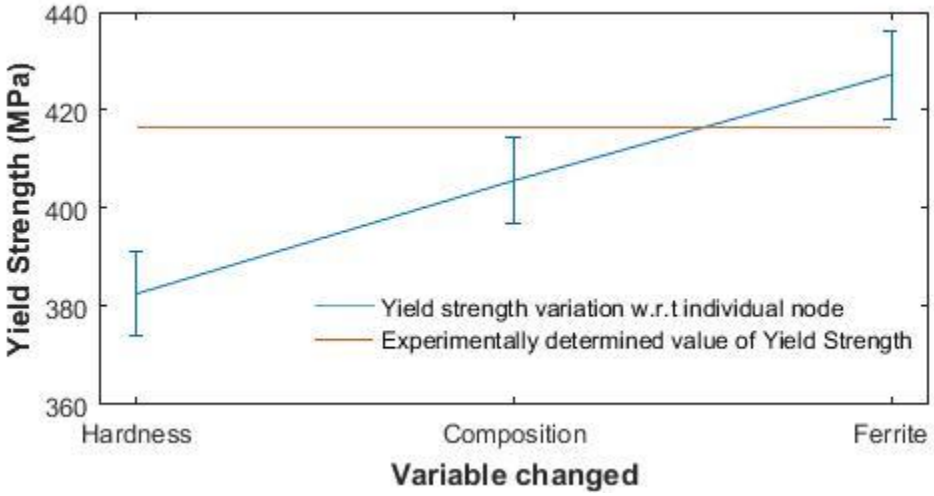

b) X47

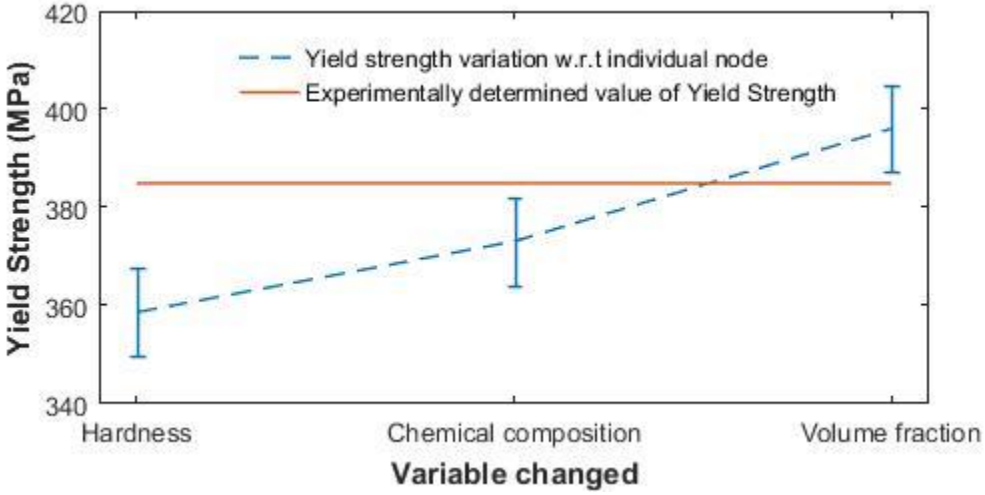

c) X42 R

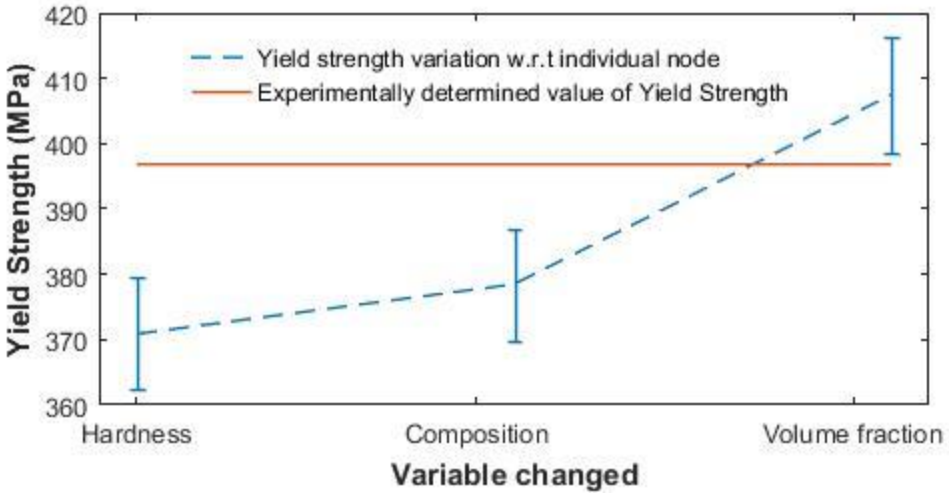

d) X42 N

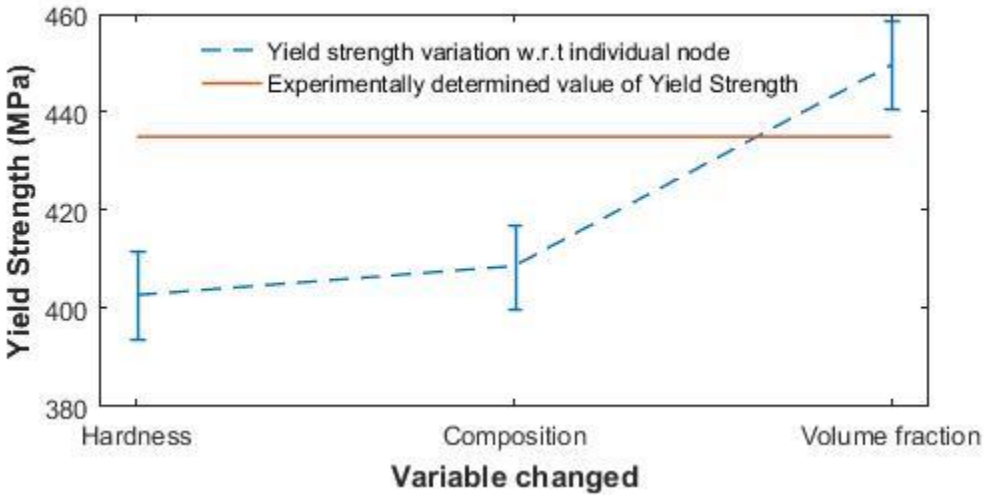

e) X65I

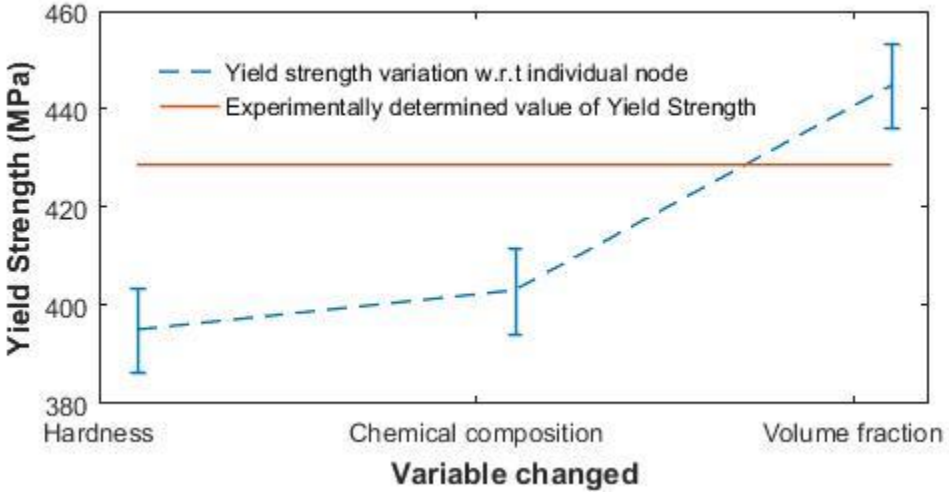

f) X65II

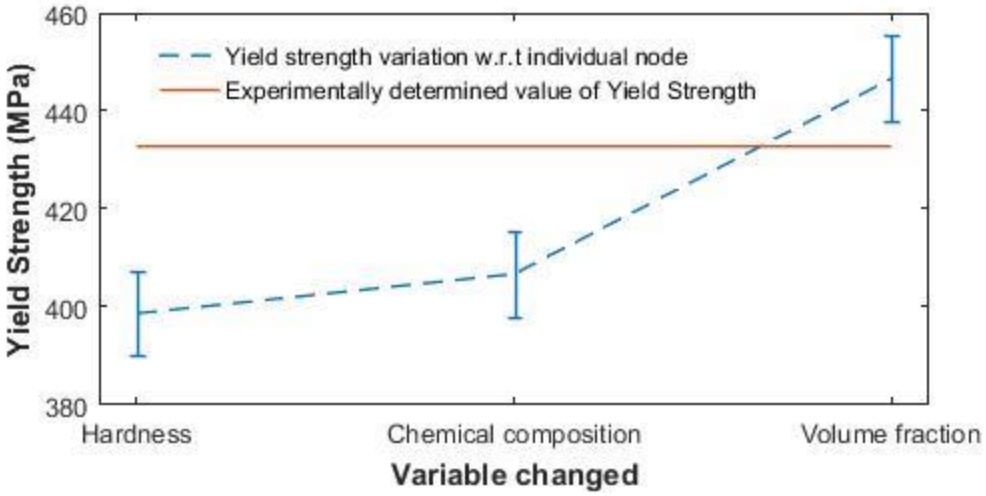

g) X65III

Fig.12 a) to g) Demonstration of variable change on the prediction capability of the different pipes

As evident, hardness seems to be the most influential factor in all the above studies. The experimental Pipes 45 and 47 showed a variation close to 8% with hardness, and about 2.5% with both volume fraction and composition analysis. For the literature data of X42R and X42N, the change in YS predicted was about 3-4% with composition and volume fraction, and about 6.5% with Hardness. Finally with the system of X65 literature pipes, the variation in predicted YS was about 3% with volume fraction change, 6% with chemical composition change, and about 7.5% with Hardness change. The X65 being the only system with a high impact from the composition side. Overall Hardness seemed to be the most influential parameter followed by composition and then volume fraction. This information will be used later to assign varied node weights to balance out these effects.

CHAPTER 2: COMPARATIVE STUDY OF STATISTICAL MODELS FOR MANUFACTURING PROPERTIES PREDICTION

Introduction

The increasing demand in the production and consumption of oil and natural gas requires continuous improvement in both the transportation efficiency and the performance of the steel pipes[19]. The properties at this expanse are higher strength accompanied with sufficient toughness and ductility which are determined by the proportion of multiple microstructures consisting of well-selected phases and refined grain sizes. For the currently used high-strength steels, the determining factors to achieve the above-listed superior properties relies in a combination of alloy composition design, metallurgical technology, thermomechanical processing or heat treatment[20]. These steels are characterized by the low Sulphur content and reduced amount of detrimental second phases such as oxides, inclusions and pearlite[19]. As the composition is limited to a certain value, the improvement in the mechanical properties heavily depends on the complex thermomechanical controlled processing (TMCP) routes. The optimization of the process parameters of the TMCP is vital in order to achieve the desired mechanical properties. Nowadays, exhaustive production control and diverse simulation techniques are used to optimize the processing parameters for producing a desired microstructure, both of which are extremely expensive and only achieve good results in an a posteriori fashion. [21] A lot of work has been reported on analyzing the effect of the TMCP processing parameters on the microstructure and mechanical properties such as the evolution of microstructure and precipitation state of high- level pipeline steel through TMCP process, in which the effects of processing parameters of TMCP, such as finish cooling temperature (FCT), finish rolling temperature (FRT) and coiling temperature on the microstructure and mechanical properties of low C-Mn steel were reported [19].

Thus, the manufacturing process parameters play an important role in the design and synthesis of new pipe grades with improved mechanical properties. In order to simplify the extensive need of process control and simulation techniques, the present work aims to utilize the pre-existing database of the effect of manufacturing process on the material properties to make a prediction of the required process parameters to obtain the desired microstructure design. Some well-known statistical models are employed for making such predictions and compared amongst themselves viz; Multivariate Linear Regression, Gaussian Process Modeling and multi-label K-nearest neighbors (ML-KNN) model and the efficiency of these models is compared. The input for these models can be the mechanical properties such as yield strength, fracture toughness required, whereas, the output will be process parameters such as cooling rate and coiling temperature. The classical linear regression is performed for multiple datasets using the generalized least square method, by minimizing the sum of squared error. The Gaussian process models are another way to perform Bayesian supervised learning. These are provided with a mean function, covariance function, and some hyperparameters for their prediction model. The final method is specifically known as ML-KNN or multi-label K-nearest neighbor, which is an extension of the traditional KNN method. This algorithm identifies k-nearest neighbors from the training data, based on the proximity of closeness from the given unknown samples.

3.1 Model for prediction of processing conditions

The focus of this section is on the application of the different statistical models to predict the process conditions during pipeline manufacturing process such as cooling rate, cooling temperature etc. The input can be used as the desired mechanical properties such as Yield Strength, percentage elongation etc.

The table below shows the input and the desired output [11]:

Labels				Features	
Rolling finish Temp (deg C)	Cooling start Temp (deg C)	Cooling End Temp (deg C)	Cooling rate (deg C/sec)	Elongation (%)	Yield Strength (MPa)
845	795	100	16	22	516
845	795	200	19	28	523
845	795	430	9.4	26	525
735	700	240	14.5	21	533
735	700	330	11	28	489
735	700	420	9.3	22	561

The prediction scheme used here are of three different types; Classical Linear Regression, Gaussian process model[32], and Multi-Label K-nearest neighbor method. The classical linear regression is performed for multiple datasets using the generalized least square method, by minimizing the sum of squared error.
The Gaussian process models are another way to perform Bayesian supervised learning[32]. These are essentially composed of mean function, covariance function, and some hyperparameters for their prediction model. The most widely used functions in here are the meanConst mean function which has a constant mean that can be specified with a single value hyperparameter, and a covSEiso which is a Squared Exponental covariance function. It has been used for regression based problems as well[33][34].

The final method is specifically known as ML-KNN or multi-label K-nearest neighbor[35], which is an extension of the traditional KNN method. This algorithm identifies k-nearest neighbors from the training data, based on the proximity of closeness from the given unknown samples. Given an unknown sample and a training set, all the distances between the unknown sample and all the samples in the training set can be computed. The distance with the smallest value corresponds to the sample in the training set closest to the unknown sample. Different types of distances can be used, Euclidean distance being most widely used. Given a training set (x1,y1) (x2,y2)….the regression model can be built.
The Euclidean distance,D is given as:

$$D(x,p) = \sqrt{(x-p)^2}$$

Where, p is the unknown test instance.
The prediction from the KNN model is the average of the outcome of the k-nearest neighbors:

$y = \frac{1}{K}\sum_i^k y_i$, where yi is the ith case of the examples sample and y is the prediction (outcome) of the query point [36].

3.1.1 Prediction from the different models:

Three small and different datasets were used for demonstration of prediction of the manufacturing conditions from the desired mechanical properties, and have been compared. At least 60% of the data was used for training and 40% used for prediction analysis for each dataset. For these comparison, Simple Linear regression follows the general scheme, the Gaussian process model uses meanConst as the mean function and covSEiso as the covariance function, and finally, the ML-KNN method uses the nearest neighbors value for k as 3, and a smoothing parameter, s as 1.

The results have been shown for the first dataset here; this is a small dataset with 12 data points, 7 of which are used for training, and the remaining 5 are used for prediction:

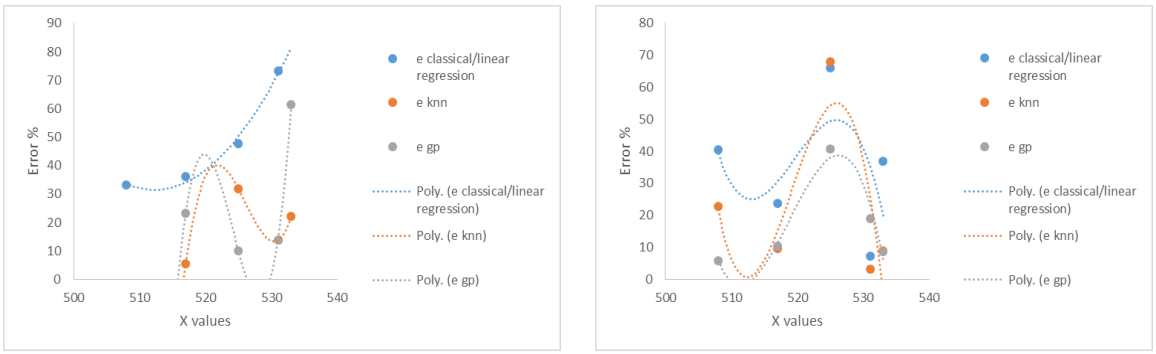

Fig.13 a) Y1 prediction b) Y2 prediction

It is observed that the prediction capability of Gaussian process model and ML-KNN work better than classical linear regression for this particular dataset. Some anomalies have been extracted to provide a better view of the model outcomes. This dataset outcome shows a relatively large error for the best prediction model to be within 40% at some places which needs to be investigated.

Dataset 2:

This dataset consists of 15 points in total, 8 of which have been used for training, and the remaining 7 have been used for prediction. There are a total of four outcomes for this particular dataset, as shown below:

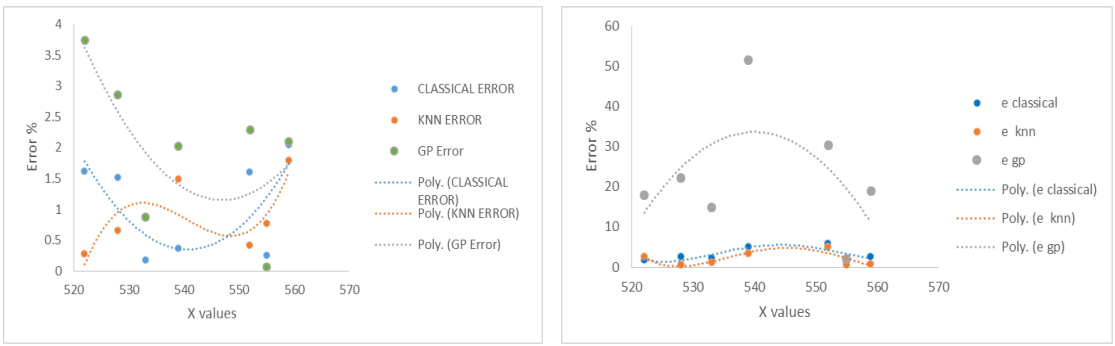

Fig.14 a) Y1 Start Rolling Temperature prediction b) Y2 Finish Rolling Temperature prediction

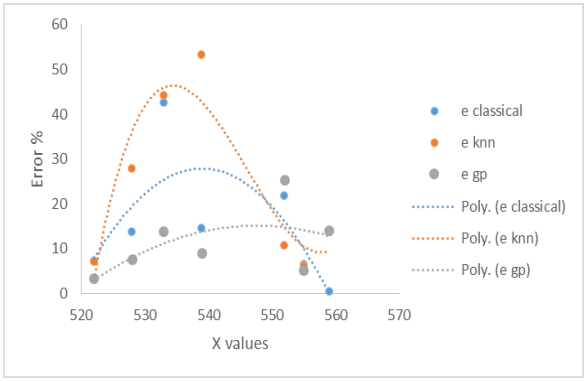

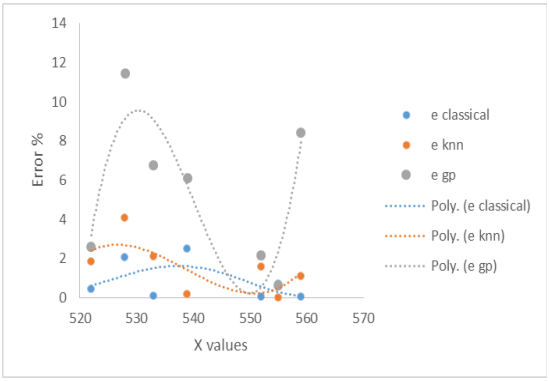

Fig.15 c) Y3 Cooling Rate prediction d) Y4 Finish Cooling Temperature prediction

It can be seen that for three of the four outcomes, the ML-KNN works either equally best or better than the classical regression (SL) model or the gaussian process (GP) model. The exception in the prediction of cooling rate may be as the data set were not normalized initially; where GP model works the best. In general, for this dataset, the error value can be kept below 15%, which is a helpful aid in the prediction of these manufacturing conditions.

Data set 3:

This is a small dataset with only 8 datapoints in total,therefore, 5 points have been used for training, and the prediction outcome is shown for 3 points initially, and the other graph shows the prediction for trainign data size 4, and prediction data size 4 as well.

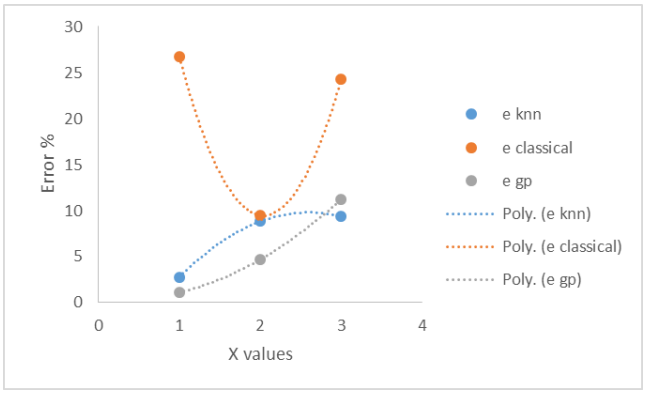

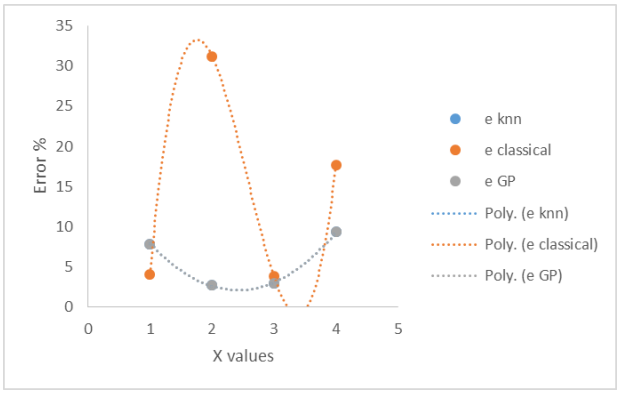

Fig. 16 a) Y1 prediction with training data size 5 b) Y1 prediction with training data size 4

Similar to the above assessments, it can also be observed in this case that the ML-KNN and GP model work well for both training size of the data, although in this case GP works slightly better or comparable to ML-KNN. The error for this dataset can be within 10% margin which also works well for prediction.

It can be seen from all the three datasets that these methods provide a good capability in the prediction of the manufacturing conditions for the desired mechanical properties. For the last two datasets, with the best prediction model, the error value can be controlled to be less than 10-15% at the maximum. In general ML-KNN works well for the three datasets.

3.1.2 Model parameter variation for the different datasets:

The parameters of the ML-KNN and the GP model have been varied, and the effect on the prediction has been reported.
The below results are for Dataset 1 for variation of k in ML-KNN method:

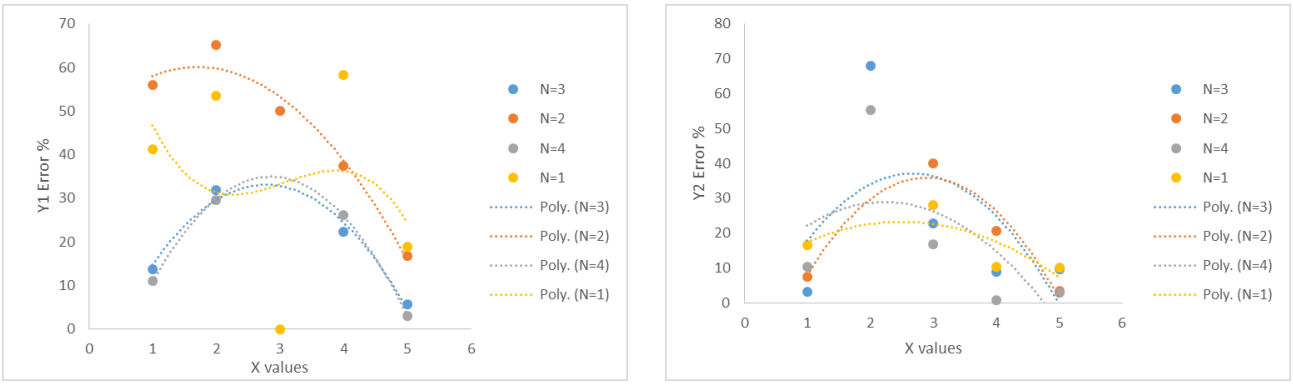

Fig.17 a) Y1 Finish cooling Temperature prediction b) Y2 cooling rate prediction

The above figures represent the impact of the variation of the number of nearest neighbors, N in the prediction outcome. It appears that N value of 3, 4 work well for Y1 prediction, whereas N values of 1 & 4 work well for Y2.

Next, the results are shown for Dataset 1 for GP model parameter variation:

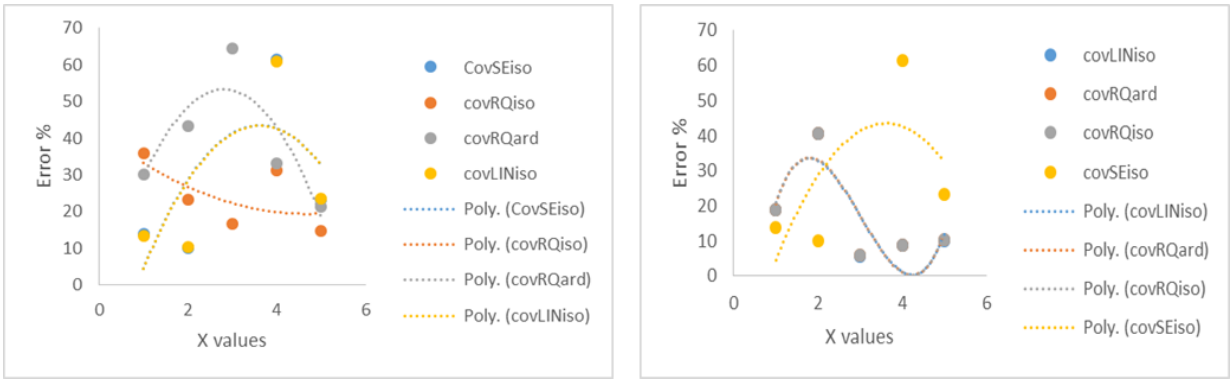

Fig.18 a) Y1 Finish cooling Temperature prediction b) Y2 cooling rate prediction

The variation in the covariance function shows that covRQiso works well for Y1, and most of the other covariance functions work well for Y2.

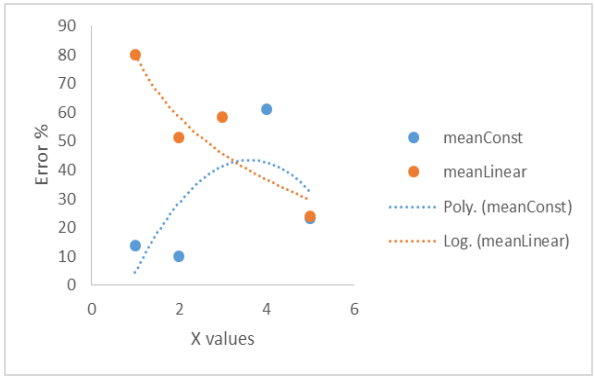

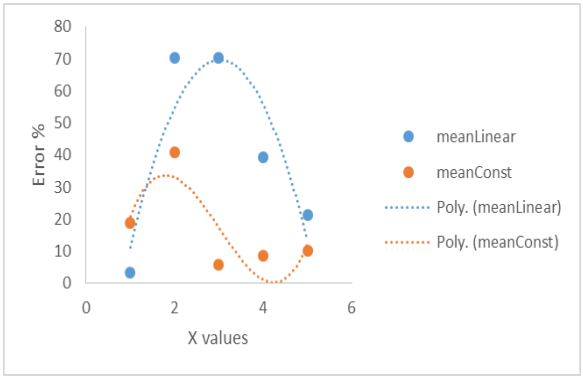

Fig.18 c) Y1 Finish cooling Temperature prediction d) Y2 cooling rate prediction

The mean function variation shows opposite trends for both Y1 and Y2 and hence no conclusion could be drawn for better mean function.

The next results are shown for Data set 2:

ML-KNN parameter variation:

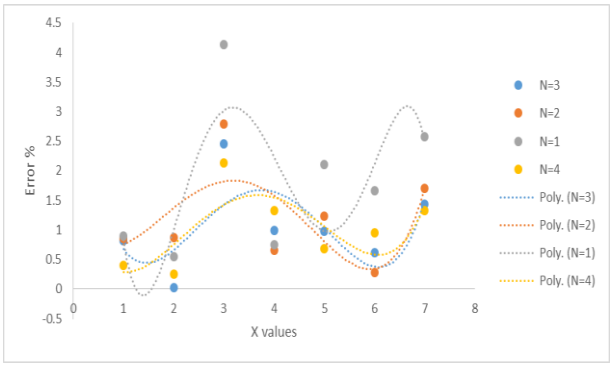

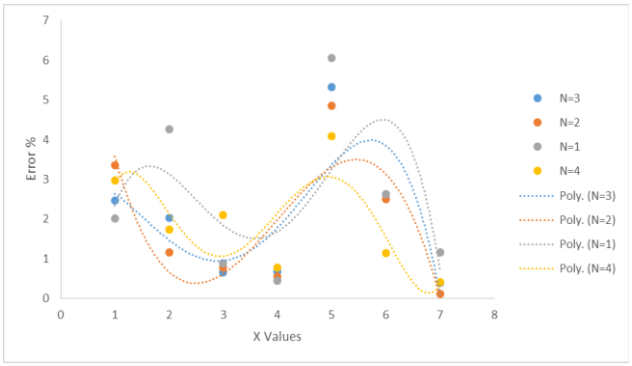

Fig.19 a) Y1 Start Rolling Temperature prediction b) Y2 Finish Rolling Temperature prediction

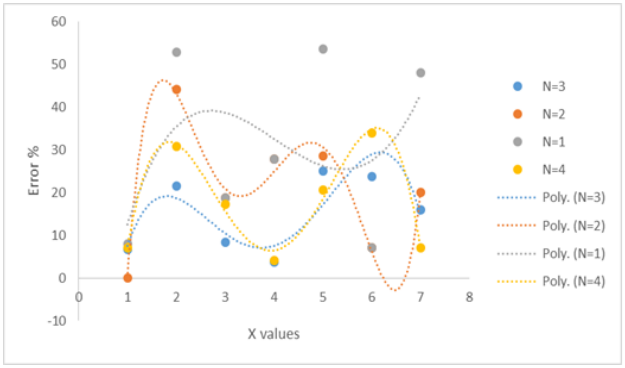

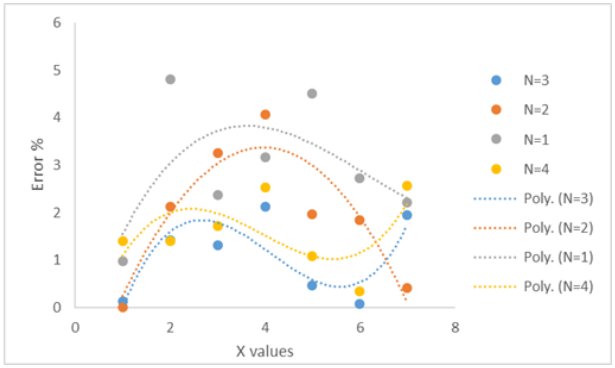

Fig.20 a) Y3 Cooling Rate prediction b) Y4 Finish Cooling Temperature prediction

The N value was varied between 1 to 4. It appears that a N value of 3 and 4 works well for all the predictive outcomes.

Next, the smoothing parameter, s, was varied between 1 to 10, and no significant change was observed, as indicarted below:

				N=3				
Y1	-0.8123	-0.0307	-2.458	0.9932	0.975	0.6184	1.4386	
Y2	-2.4664	2.0377	-0.6608	0.6696	-5.3289	2.6166	-0.3867	
Y3	6.6667	21.5686	8.3333	-3.7037	-25	23.8095	-16	
Y4	0.1287	-1.4103	1.3123	2.1164	-0.4575	-0.0647	1.9411	S=1
Y1	-0.8123	-0.0307	-2.458	0.9932	0.975	0.6184	1.4386	
Y2	-2.4664	2.0377	-0.6608	0.6696	-5.3289	2.6166	-0.3867	
Y3	6.6667	21.5686	8.3333	-3.7037	-25	23.8095	-16	
Y4	0.1287	-1.4103	1.3123	2.1164	-0.4575	-0.0647	1.9411	S=2
Y1	-0.8123	-0.0307	-2.458	0.9932	0.975	0.6184	1.4386	
Y2	-2.4664	2.0377	-0.6608	0.6696	-5.3289	2.6166	-0.3867	
Y3	6.6667	21.5686	8.3333	-3.7037	-25	23.8095	-16	
Y4	0.1287	-1.4103	1.3123	2.1164	-0.4575	-0.0647	1.9411	S=3
Y1	-0.8123	-0.0307	-2.458	0.9932	0.975	0.6184	1.4386	
Y2	-2.4664	2.0377	-0.6608	0.6696	-5.3289	2.6166	-0.3867	
Y3	6.6667	21.5686	8.3333	-3.7037	-25	23.8095	-16	
Y4	0.1287	-1.4103	1.3123	2.1164	-0.4575	-0.0647	1.9411	S=4
Y1	-0.8123	-0.0307	-2.458	0.9932	0.975	0.6184	1.4386	
Y2	-2.4664	2.0377	-0.6608	0.6696	-5.3289	2.6166	-0.3867	
Y3	6.6667	21.5686	8.3333	-3.7037	-25	23.8095	-16	
Y4	0.1287	-1.4103	1.3123	2.1164	-0.4575	-0.0647	1.9411	S=5
Y1	-0.8123	-0.0307	-2.458	0.9932	0.975	0.6184	1.4386	
Y2	-2.4664	2.0377	-0.6608	0.6696	-5.3289	2.6166	-0.3867	
Y3	6.6667	21.5686	8.3333	-3.7037	-25	23.8095	-16	
Y4	0.1287	-1.4103	1.3123	2.1164	-0.4575	-0.0647	1.9411	S=10

GP model parameter variation:

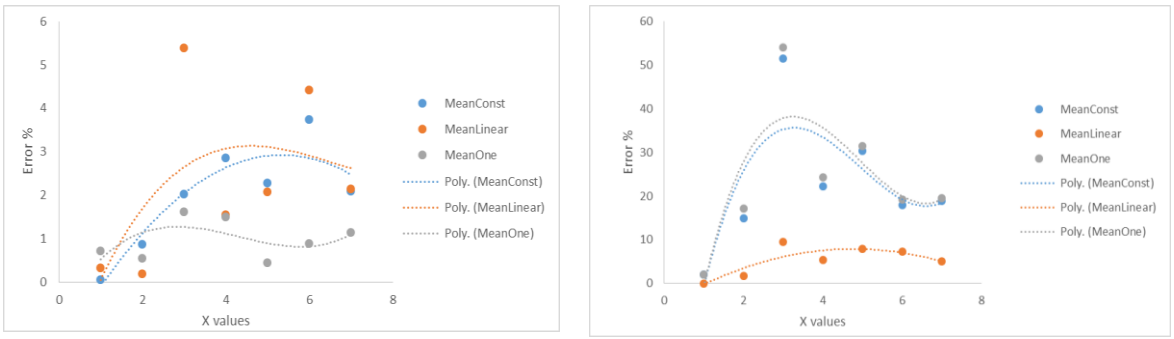

Fig.21 a) Y1 Start Rolling Temperature prediction b) Y2 Finish Rolling Temperature prediction

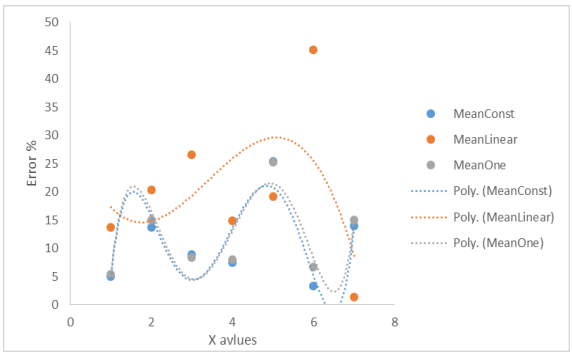

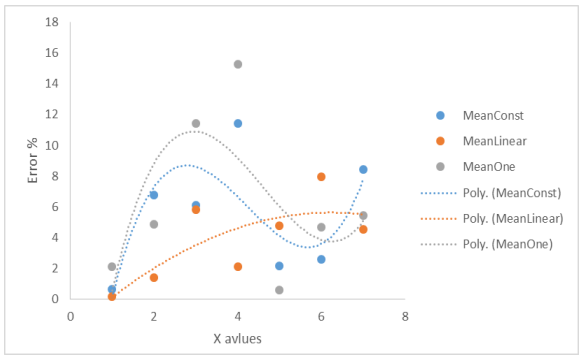

Fig.22 a) Y3 Cooling Rate prediction b) Y4 Finish Cooling Temperature prediction

It appears that MeanLinear and Meanconstant both work well for most of the predictive outcomes for this data set for the mean function variation.

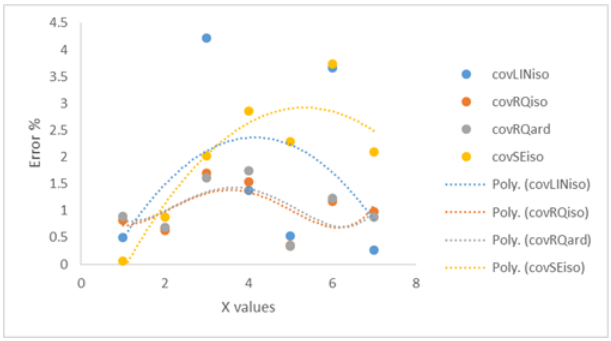

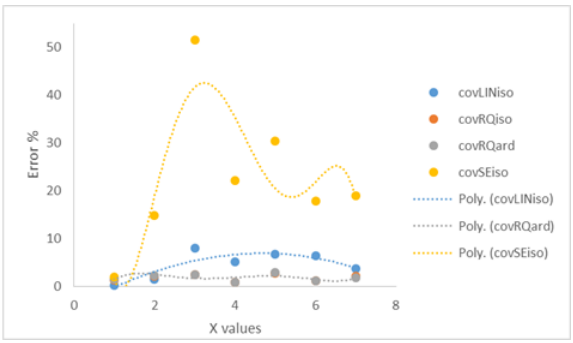

Fig.23 a) Y1 Start Rolling Temperature prediction b) Y2 Finish Rolling Temperature prediction

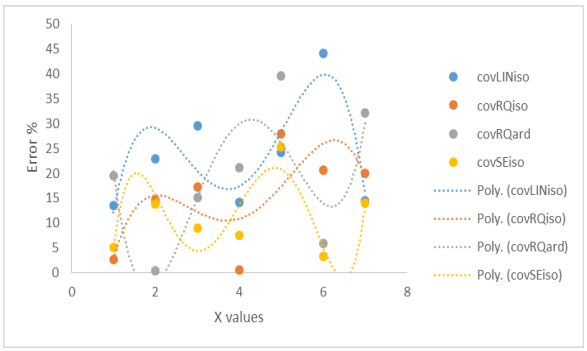

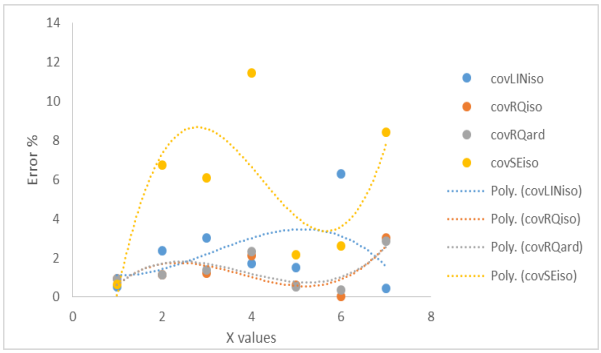

Fig.24 a) Y3 Cooling Rate prediction b) Y4 Finish Cooling Temperature prediction

It can be seen that for the covariance function variation, covRQard and covRQiso work well for atleast three out of four prediction outcomes.

Predictions for Dataset 3:

ML-KNN parameter variation:

The number of nearest neighbor was varied from 1 to 3 for this dataset. There is only a single outcome for this dataset as indicated earlier.

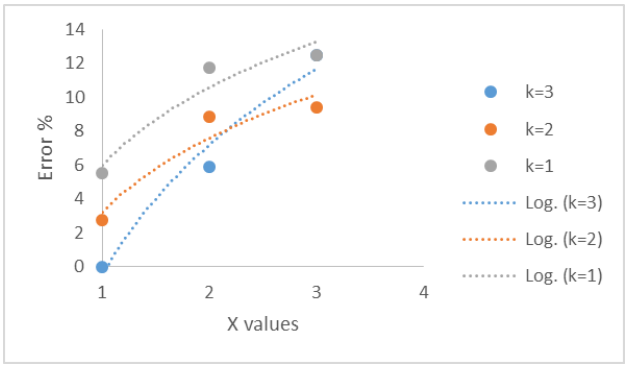

Fig.25 Y1 prediction

It appears that k value of 2 works best to keep the error below 10% for this particular dataset.

GP model parameter variation:

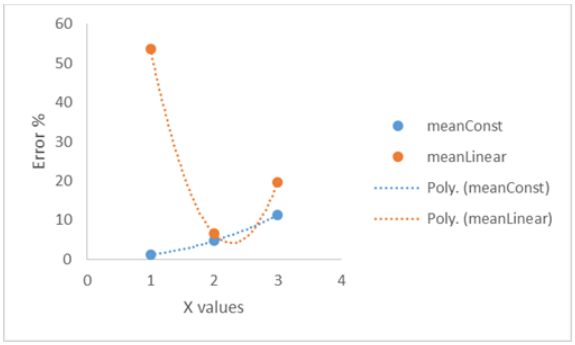

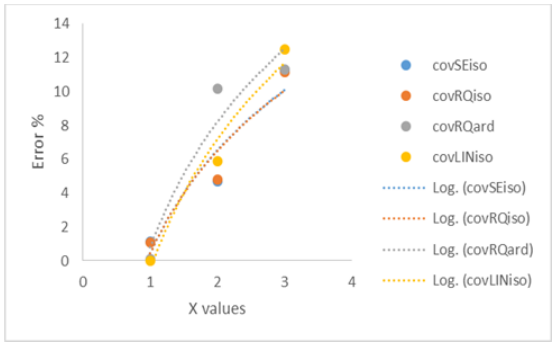

Fig.26 a) Y1 Mean function variation b) Y1 Convariance function variation

It can be observed that meanConst works well for meanfunction and covRQiso covariance function works well for this particular dataset to keep the error value to be about 10%.

It can be inferred from the above results that the value of number of nearest neighbor depends on the number of points in the dataset, and in general a value of N=3 would work for smaller datasets upto 15-20 points.

Also, the covariance function covRQiso works well for similar smaller datasets, whereas meanConst mean function works well for the model parameters of Gaussian process.

CHAPTER 3: INVESTIGATION OF VARIATION IN THE FATIGUE BEHAVIOR OF THE STEELS THROUGH THE THICKNESS OF THE PIPE SAMPLE

Introduction

The cyclic loadings during transportation (transit fatigue) and during service life, pipelines used in the oil and gas exploration suffer from significant fatigue damage, which if not enough to lead to a fracture, may severely affect the structural integrity of these entities. The fatigue damage in the pipe may occur even before they enter in service due a mechanism called transit fatigue. During transportation, pipes are subjected cyclic stresses, related to inertial and gravitational forces which are responsible for the nucleation and growth of fatigue cracks inside them, which compromise their structural integrity. The offshore line pipes may also suffer from fatigue damage during their service life due to the structures being subjected to cyclic loading originated from: cyclic pressure and thermal expansion loads and waves movement induced loads. Another way to have fatigue failures is in the pipelines used to transport hydrogen, especially at lower frequencies[22]. The resulting hydrogen embrittlement results in a loss of ductility and therefore the ASME codes impose the use of pipe with specified minimum yield strengths less than 360 MPa (52 ksi) for the transportation of hydrogen. This leaves steels with an API grade of X52 or lower for the same purpose, which are the steel grades associated with the present research work[23]. The effect of hydrogen gas on the fatigue properties of pipeline steels is not as well documented as tensile properties, however, because fatigue is not an uncommon contributor to failures observed in the operation of pipelines, fatigue properties may provide a better metric of the performance of a material in service. The research works therefore aims to investigate how the fatigue growth rates of cracks vary in the circumferential direction along the pipe wall thickness[24]. The specimens are drawn from different depths and growth rates has been done through the analysis of da/dN x ΔK curves, focusing on their Region II (Fig.) where the cyclic growth of the fatigue crack is linear (on a log-log plot) and can be predicted by the Paris-Erdogan Law[22]:

$$\frac{da}{dN} = C\Delta K^m \tag{0.1}$$

where da/dN is the fatigue crack growth rate, C and m are scaling constants and ΔK is the stress intensity factor range. The Paris-Erdogan Law only considers the ΔK increasing for the fatigue crack growth rate evaluation, and ignores the effect of the other parameters such as the load ratio and load frequency which also may impact the values of C and m. Therefore, for a given material, the evaluation of crack growth rates are to be done when the environmental conditions, temperature as well the load ratio and frequency are fixed, to reduce the influence on C and m.

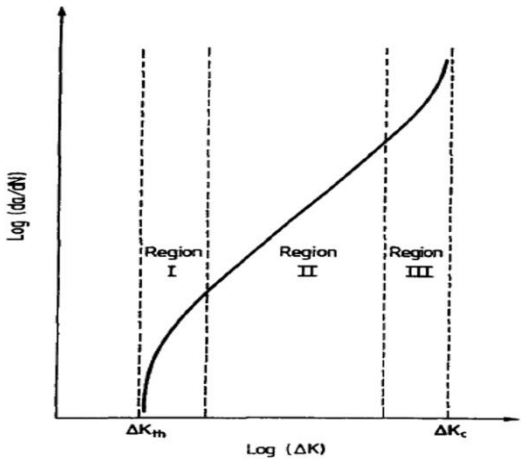

Fig. 27 Typical fatigue crack growth curve for metals showing its Regions I, II and III[22]

3.2 Test set up for Fatigue property analysis

The fatigue behavior of three pipe steels have been analyzed here. The experimental investigation of fatigue behavior was conducted in the Servo-hydraulic MTS machine. This detail presented is for the top surface layer, which is going to be extended to through-thickness study of the fatigue behavior of the sample. The experiment was conducted at room temperature with a load level of 1300~1500 N to start the pre-cracking and a corresponding load shedding was performed until 1000N to observe about 20 data points for crack growth. The R-ratio used was 0.1, and the frequency was 5 Hz. A single-edged specimen with notch was used for testing, as depicted in the picture below:

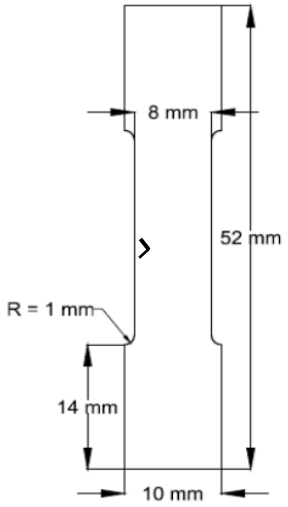

Figure 28: Dimension of fatigue test specimen with notch

The notch is sharpened further prior to the experiment to ease in crack initiation. The fatigue property analysis includes studying the crack growth rate of the specimen with respect to the number of cycles, and are not tested till complete failure. The images for the crack initiation are presented here:

3.3 Crack growth behavior of the pipe steel

The crack growth is assessed in terms of Number of cycles and crack length. The results are shown below for the three pipes.

Pipe 47:

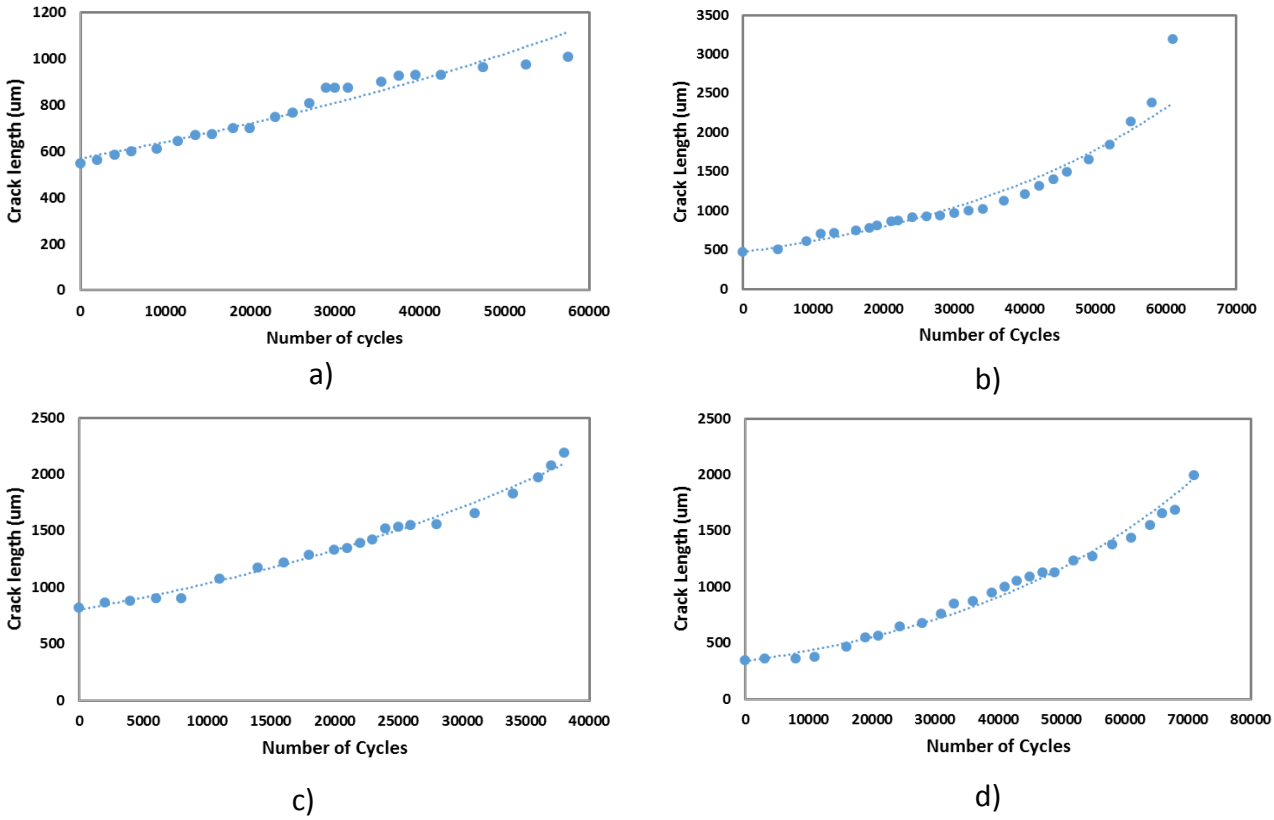

Fig. 29 Fatigue crack growth, da/dN curves for Pipe 47 along the depth; a) Outer surface b)Middle region-1 c) Middle region-2 d)Inner surface

The total crack length in the pipe 47 was seen to be 1007 um for sample 1 towards the outer region, Sample 2 or middle region-1was tested until failure and the crack length before failure was 3200um. Sample 3 or the middle region-2 had a crack length of 2080 um, and lastly sample 4 towards the outer region was tested until the crack length of 1993 um.

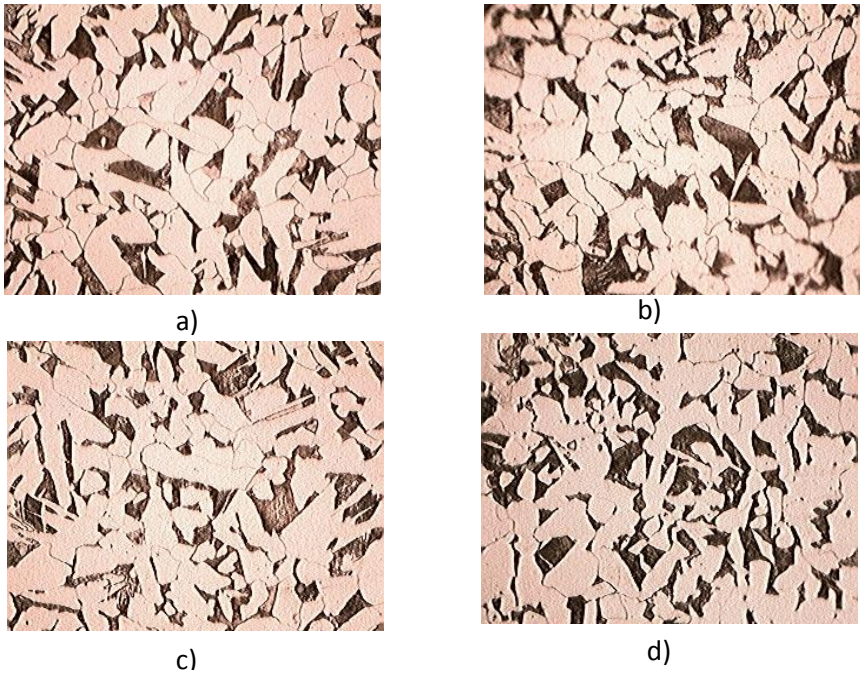

Fig. 30 Grain structure after deformation of Pipe 47 a) Outer region 1 b) Middle region-2 c) Inner region-1 d) Inner region-2

Crack growth characteristic of Pipe 47:

In order to investigate the pattern of crack growth (intergranular or transgrannular), etching was done on the sample and the crack was viewed under SEM. The following images show the crack growth pattern for Pipe 4

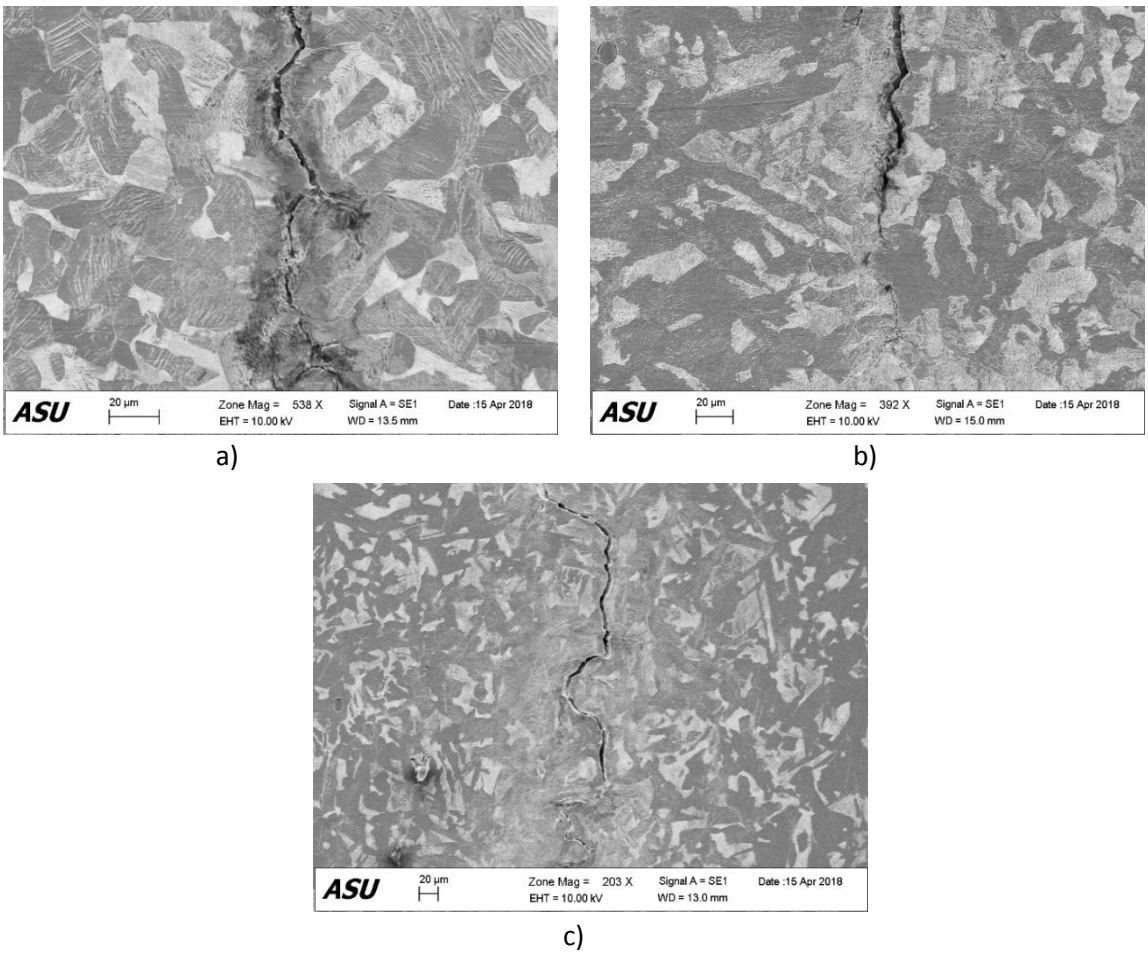

Fig. 31 Crack growth pattern of Pipe 47 a) Outer region 1 b) Middle region-2 c) Inner region

As can be observed by the above images, a clear analysis could not be drawn about the growth characteristic for the crack. The preferential etching after the test made the view not clear enough to be able to analyze the same with a SEM technique. The next step here would be to either etch the sample prior to testing to avoid preferential etching, or in a more advanced manner, conduct an EBSD around the crack to see the presence of grains and also the changes in the texture from the base metal

Pipe 44:

The crack growth curves for Pipe 44 are:

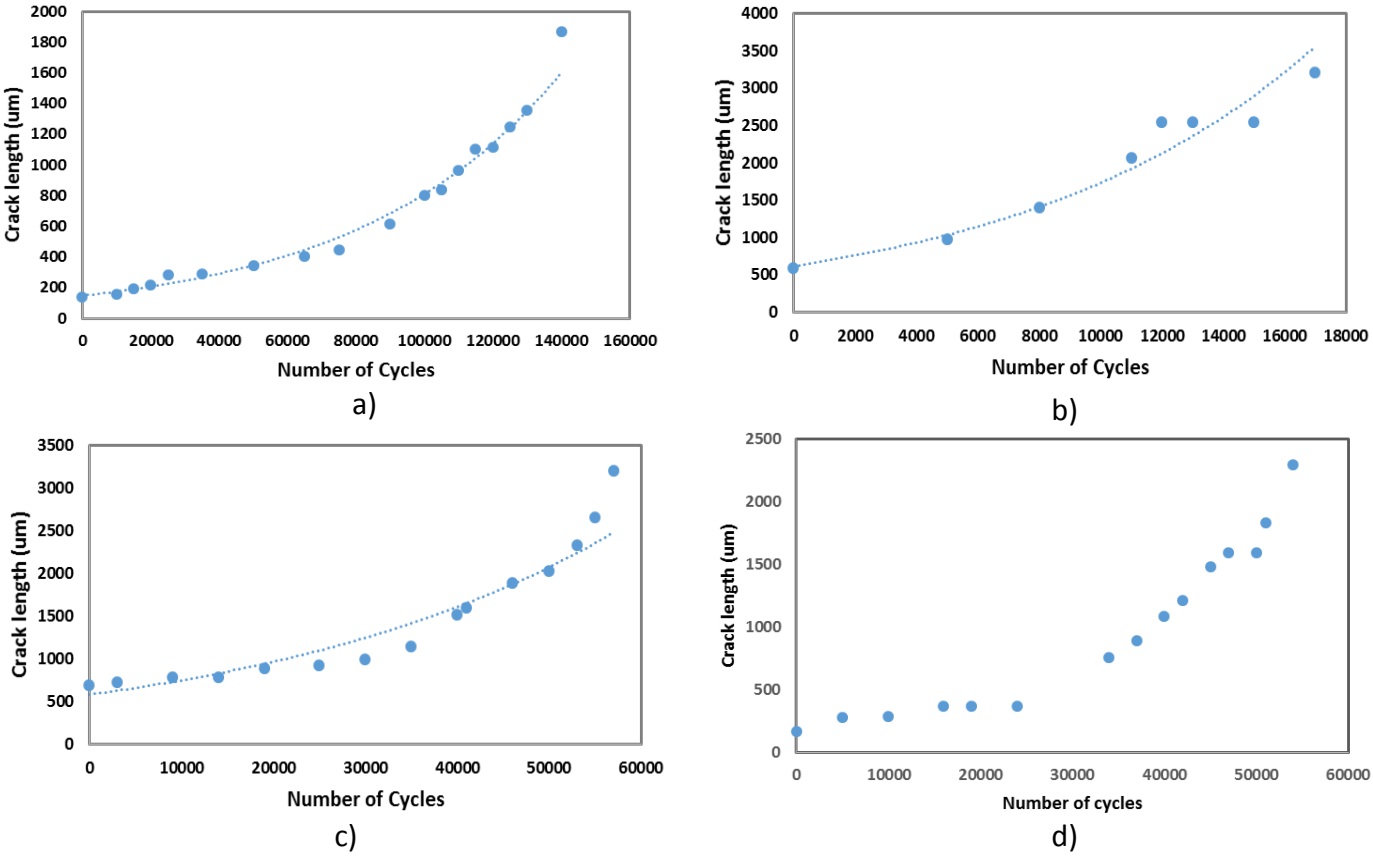

Fig. 32 Fatigue crack growth, da/dN curves for Pipe 44 along the depth; a) Outer surface b)Middle region-1 c) Middle region-2 d)Inner surface

The total length of the crack before failure for the pipes were 1920 um for the top layer, 3126 for the middle region-1,3289 for middle region-2, 2405 for the inner region.

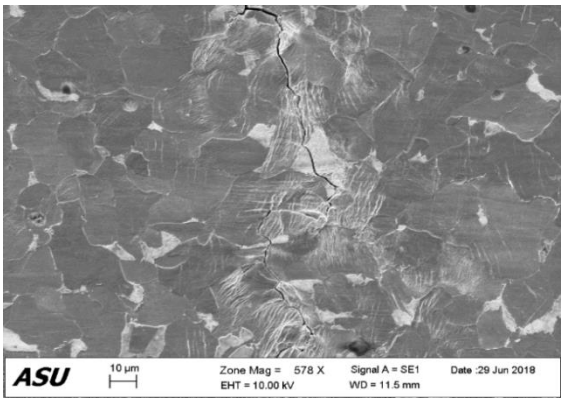

a)

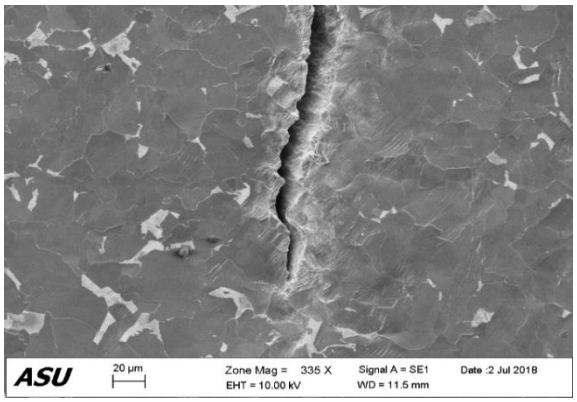

b)

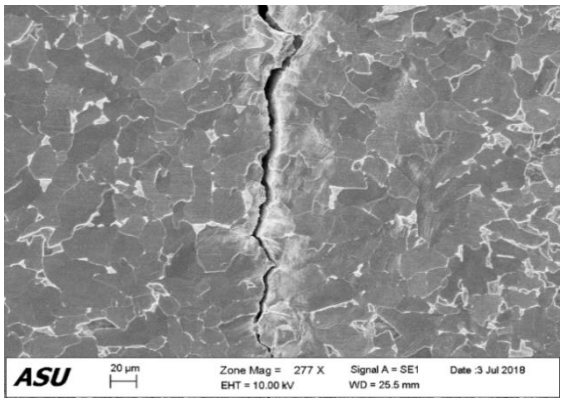

c)

Fig. 33 Crack growth pattern of Pipe 44 a) Outer region 1 b) Middle region-2 c) Inner region

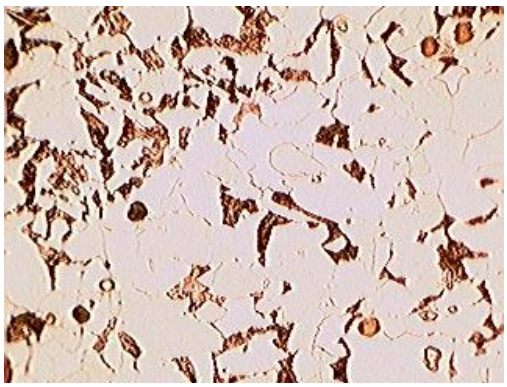

a)

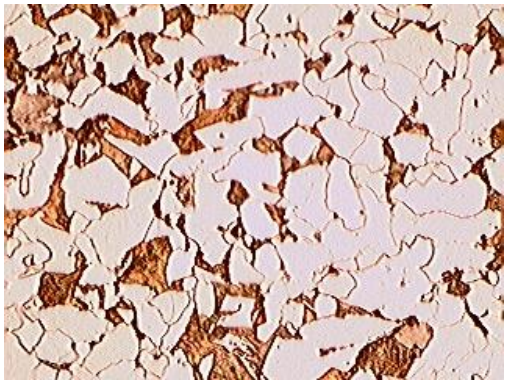

b)

c)

Fig. 34 Grain structure after deformation of Pipe 47 a) Outer region 1 b) Middle region-2 c) Inner region-1 d) Inner region-2

Pipe 35:

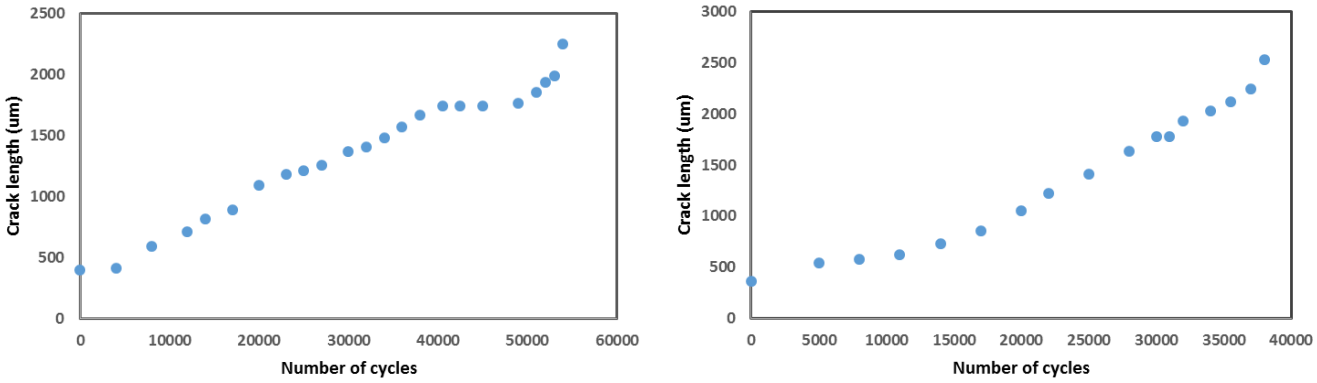

a) b)

Fig. 35 Fatigue crack growth, da/dN curves for Pipe 44 along the depth; a) Outer surface b)Middle region-1 c) Middle region-2 d)Inner surface

The final crack length for pipe 35 samples are 2300 for top region, and 2600 for the bottom region.

The parameters of fatigue crack growth are depicted in the table below:

Table

Pipe Layers	Pipe 44		Pipe 44		Pipe 35	
	m	C	m	C	m	C
Outer region	3.20	$10^{-11.91}$	3.2	$10^{-10.9}$	3.2	$10^{-11.29}$
Middle region-1	1.58	$10^{-8.9}$	2.43	$10^{-10.4}$		
Middle region-2	4.37	$10^{-13.4}$	3.52	$10^{-11.9}$		
Inner region	3.47	$10^{-11.9}$	2.38	$10^{-10.5}$	3.19	$10^{-11.27}$

CHAPTER 4: 3-D STOCHASTIC RECONSTRUCTION MODEL

Introduction

This reduction in the data volume will be achieved through the development of a 3-D reconstruction model, of the stochastic type, from the 2-D morphological information available from the surface depths, primarily for a two phase system, to be a representative of the bulk structure of the material.

The methodology used for this is based on the stochastic reconstruction scheme developed by Yeong and Torquato [25]. Key structural features, known as statistical descriptors are extracted from the 2D images that can contain various correlation functions. A typical 2-point correlation function for a statistically inhomogeneous system is;

$$S_2^{(i)}(x_1, x_2) = \langle I^{(i)}(x_1) I^{(i)}(x_2) \rangle = S_2^{(i)}(|x_1 - x_2|) \tag{0.2}$$

Where x1 and x2 are two arbitrary points and $S_2^{(i)}(x_1,x_2)$ is the probability of finding the two points in the same phase. A state of minimum "energy" is then computed from the given set of local minima, by the phase pixel interchange procedure in the digitized media.

$$E = \sum_i [f_s(r_i) - f_s(r_i)]^2 \tag{0.3}$$

Where, $f_0(r)$ is the known two-point correlation function of the reference system, and $f_s(r)$ of the reconstructed digitized system, with r being the distance between two points in the system. The resultant energy from the phase interchange method is obtained as E', with the energy difference as E-E'. The probability of the phase interchange given by the Metropolis method is given as:

$$P\left(E_{old} \rightarrow E_{new}\right) = \begin{cases} 1, & \Delta E < 0 \\ \exp\left(-\frac{\Delta E}{T}\right), & \Delta E \geq 0 \end{cases} \tag{1.1}$$

Where T represents temperature, and is adjusted with the simulation annealing method to converge the energy to a global minimum.

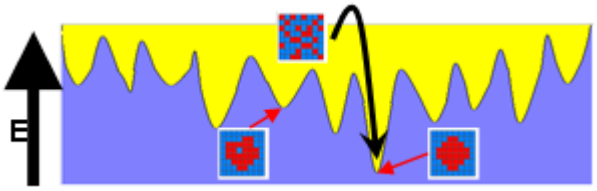

Fig.36 The local minima, with the arrow towards the global minimum

5.1 3-D stochastic reconstruction model for Pipe 45

The 3-D reconstruction was performed for two surface layers of Pipe 45, outer and middle region using a 2-D correlation function in perpendicular directions. The reconstructed images are presented below:

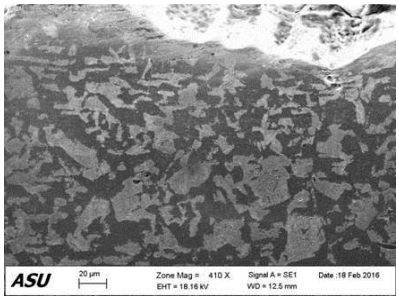

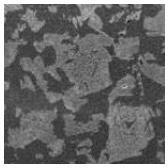

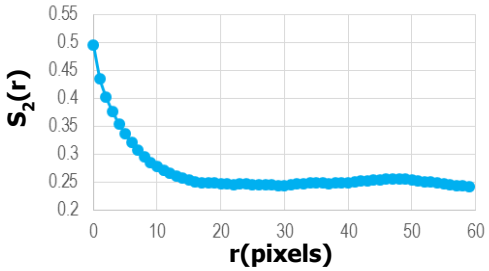

Fig.14 a) Raw Images

Fig.14 b) 2D Correlation function

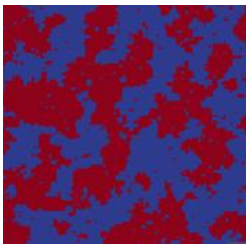

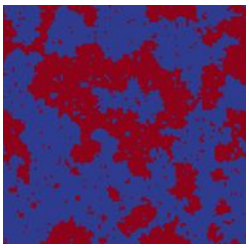

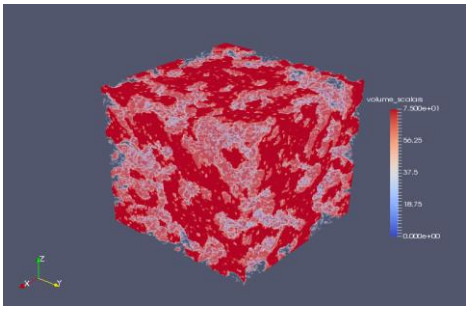

Fig.14 c) 2D slices

Fig.14 d) 3D Reconstruction

Fig. 37 3-D reconstruction for outer surface of Pipe 45

The reconstruction representation has the base image, followed by the cropped image fed for reconstruction. The extracted 2-D correlation function is presented and the final obtained reconstructed slices and 3-D image are presented

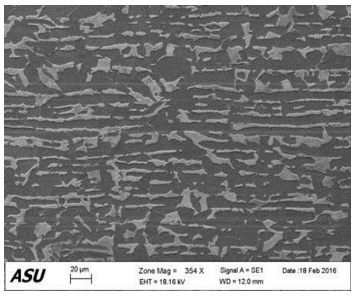

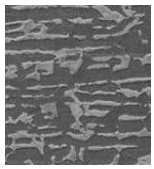

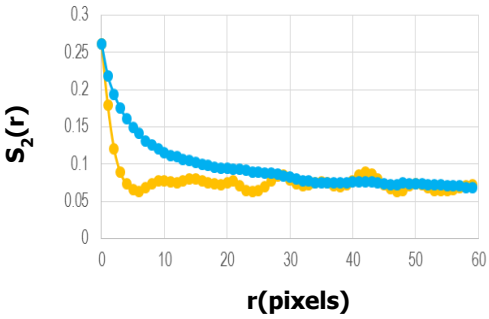

Fig.15 a): Raw Images

Fig.15 b): 2D Correlation function

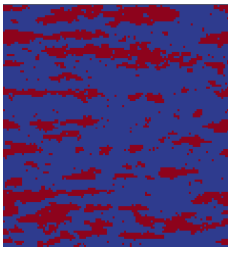

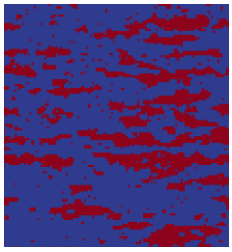

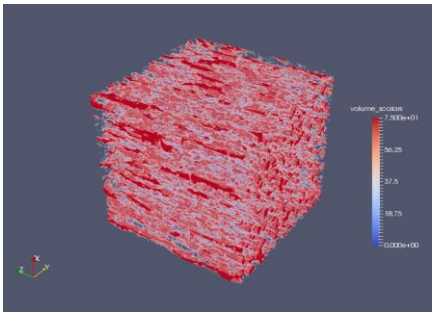

Fig.15 c): 2D slices

Fig.15 d): 3D Reconstruction

Fig. 38 3-D reconstruction for middle surface region of Pipe 45

It can be seem that there is a considerable difference in the features of the outer and the middle region, which can be very well picked up by the reconstruction algorithm as well. The next step would be to extract linear elastic properties from these reconstructed segments using techniques such as Finite Element Method and compare them against the true properties for validation. This can be followed by plastic properties depending on the performance of the elastic properties prediction.

6. Summary and Conclusion:

The integrity assessment of the aging Natural gas pipeline system is proposed through the design of the Bayesian Network framework model, which integrates the different material properties derived from in-situ measurements. The model is validated from the results of experimental measurements to show an improved accuracy of strength prediction. Three field samples and a few literature databases were investigated to obtain the data for the model prediction and training. Next, a few popular statistical models were employed to aid in prediction of manufacturing process parameters and the impact of the parameter variation was studied for each dataset. Finally, fatigue behavior of the Pipe 47 was studied for variations in crack growth rate. The major conclusions from the present study are depicted here:

1. Model validation performed by comparing the results of yield strength prediction from individual nodes versus prediction from all nodes together, showed an improved prediction with the latter. It was observed that prediction of yield strength with individual node Hardness resulted in a value being in a proximity of 11.8-36.4 % of the true experimental value. Similarly, prediction with node Chemical composition alone showed a large deviance of 34-49.17% from the experimental value, prediction with node volume fraction showed a deviation of 27.34-49.14%, and when taken all together, the combined prediction with all the nodes showed the smallest deviation of 1.34-14.8% from the true experimental value.

2. Another important feature extracted out of this model was the ability to update all the nodes by modifying one of the nodes (updating information on Hardness resulted in change in the probability distributions of Silicon and Ferrite related node), signifying a systematic flow of information through the network. This feature can be exploited in terms of obtaining a probabilistic estimate for any missing component.

3. Next, the model was trained to modify the regression coefficients by making use of data points from the similar system and an improvement in the prediction capability of about 4-13% was observed.

4. The node sensitivity study for the Bayesian network model suggested that Hardness was the most sensitive node for which a change of 30% is followed by a change in 10% in the

prediction capability, whereas the volume fraction was the least sensitive node that changed the prediction capability by 4% approximately.

5. The performance of KNN model depends on of number of nearest neighbor which in turn depends on the number of points in the dataset. A value of k=3 seemed to work for smaller datasets up to 15-20 points.

6. For the Gaussian process model, the covariance function covRQiso appears to work better for such smaller datasets, whereas mean function that works well for the same is meanConst.

7. The fatigue crack growth pattern was observed to be transgranular through the specimen. The microstrcuctural features such as the grain size and volume fraction of ferrite depicted a slight change after deformation, compared to the base metal.

8. The parameters of fatigue crack growth depicted a slight change through the thickness of the pipe sample relating to the microstructure. The constant m was found in the range of 2.5~4.5, whereas the constant C was observed to be in the range of 10^{-9} ~ 10^{-13}

7. Future scope:

7.1 Bayesian Network validation, coefficients modification and sensitivity analysis for prediction of UTS

As the current system is mainly focused on the prediction of Yield strength, the same can be replicated for the ultimate tensile strength for all the samples. The prediction can be tested for validation against the individual prediction nodes, parametric analysis of the individual nodes, as well as if the modification of coefficients is able to make an improvement in the prediction.

The present model is designed with an equal weightage of all nodes, which can be modified through extensive training with a large data set by performing sensitivity analysis to obtain a more precise prediction of the strength, or through numerical simulation approaches. The model can be further explored in terms of accommodating the acoustic and electromagnetic properties, to obtain a holistic prediction of strength from a complete set of material properties data. This study, overall, can be extended to a larger volume of data to improve the prediction capability of the model system, and training and validation can also be performed on specific grades of interest

7.2 Analyzing Impact of Training data and model selection for the datasets

As indicated for the study based on comparison of the models for the prediction of the manufacturing process parameters, 60 percent of the data was used for training and the remaining was used for prediction. An interesting thing to analyze would be the performance of these models to varying sizes of training data (limited due to the small datasets). Some other approaches will be investigated to complete this section.

7.3 Texture study of the fatigue and tensile tested samples

Texture of the samples will be studies using Electron backscatter diffraction (EBSD) analysis. Sample preparation will the same as for microstructure examination as described in section 4.1.1. A change in the texture will be noted after the deformation through Tensile and Fatigue Test, and also along the pipe wall thickness direction. A correlation between the mechanical properties and texture will then be investigated.

8. References

[1] "US Energy Information Administration website," *June 2007*. [Online]. Available: https://www.eia.gov/naturalgas/archive/analysis_publications/ngpipeline/index.html. [Accessed: 07-Nov-2017].

[2] "Oil Pipeline Testing Methods," 2015.

[3] T. Support, E. G. Kirkpatrick, A. D. Eastman, C. G. Transmission, C. Public, U. Commission, G. Order, T. Support, P. Dimensions, and L. Pressure, "Approved by : A-34 A :," pp. 1–26.

[4] D. Zelmati, O. Ghelloudj, and A. Amirat, "Correlation between defect depth and defect length through a reliability index when evaluating of the remaining life of steel pipeline under corrosion and crack defects," *Eng. Fail. Anal.*, vol. 79, pp. 171–185, 2017.

[5] US news | NBC News, "Most gas lines don't use latest inspection technology," 14-Sep-2010.

[6] Haggag, "In-Situ Measurement of Pipeline Mechanical Properties Using Stress-Strain Microprobe – Validation of Data for Increased Confidence & Accuracy," 2007.

[7] S. H. Hashemi, "Strength-hardness statistical correlation in API X65 steel," *Mater. Sci. Eng. A*, vol. 528, no. 3, pp. 1648–1655, 2011.

[8] A. N. Network and F. E. Simulation, "Property Estimation with Automated Ball Indentation Using Artificial Neural Network and Finite Element Simulation," vol. 4, no. 4, pp. 503–506, 2010.

[9] B. Amend, "In-situ Analyses to Characterize the Properties and Metallurgical Attributes of In-Service Piping." NACE International.

[10] A. Vary, "Concepts and Techniques for Ultrasonic Evaluation of Material Mechanical Properties," in *Mechanics of Nondestructive Testing*, W. W. Stinchcomb, J. C. Duke, E. G. Henneke, and K. L. Reifsnider, Eds. Boston, MA: Springer US, 1980, pp. 123–141.

[11] G. Dobmann, N. Meyendorf, and E. Schneider, "Nondestructive characterization of materials A growing demand for describing damage and service-life-relevant aging processes in plant components," *Nucl. Eng. Des.*, vol. 171, pp. 95–112, 1997.

[12] E. D. Merson, M. M. Krishtal, D. L. Merson, A. A. Eremichev, and A. Vinogradov,

"Effect of strain rate on acoustic emission during hydrogen assisted cracking in high carbon steel," *Mater. Sci. Eng. A*, vol. 550, pp. 408–417, 2012.

[13] G. Dobmann, M. Kröning, W. Theiner, H. Willems, and U. Fiedler, "Nondestructive characterization of materials (ultrasonic and micromagnetic techniques) for strength and toughness prediction and the detection of early creep damage," *Nucl. Eng. Des.*, vol. 157, no. 1–2, pp. 137–158, 1995.

[14] R. Bickerstaff, M. Vaughn, G. Stoker, M. . Hassard, and M. Garrett, "Review of Sensor Technologies for In-line Inspection of Natural Gas Pipelines," *Sandia Natl. ...*, no. Ili, pp. 1–10, 2002.

[15] L. Smart and L. J. Bond, "Material Property Relationships for Pipeline Steels and the Potential for Application of NDE," in *AIP Conference Proceedings 1706, 160003*, 2016.

[16] H. M. Nykyforchyn, O. T. Tsyrul'Nyk, D. Y. Petryna, and M. I. Hredil', "Degradation of steels used in gas main pipelines during their 40-year operation," *Strength Mater.*, vol. 41, no. 5, pp. 501–505, 2009.

[17] Kamtornkiat Musiket; Mitchell Rosendahl; and Yunping Xi, "Fracture of Recycled Aggregate Concrete under High Loading Rates," *J. Mater. Civ. Eng.*, vol. 25, no. October, pp. 864–870, 2016.

[18] D. Ersoy, "Existing gaps between current diagnosis techniques and true material states for pipe integrity assessment," 2015.

[19] D. B. Rosado, W. De Waele, and D. Vanderschueren, "Latest developments in mechanical properties and metallurgycal of high strenght line pipes," *Sustain. Constr. Des.*, vol. 4, no. 1, pp. 1–10, 2013.

[20] M.-C. Zhao, K. Yang, and Y. Shan, "The effects of thermo-mechanical control process on microstructures and mechanical properties of a commercial pipeline steel," *Mater. Sci. Eng. A*, vol. 335, no. 1–2, pp. 14–20, 2002.

[21] I. Santos, J. Nieves, Y. K. Penya, and P. G. Bringas, "Machine-learning-based mechanical properties prediction in foundry production," *2009 Iccas-Sice*, pp. 3–8, 2009.

[22] A. M. Korsunsky, D. Dini, and M. J. Walsh, "Fatigue crack growth rate analysis in a titanium alloy," *Key Eng. Mater.*, vol. 385–387, no. June 2017, 2008.

[23] E. Drexler and R. Amaro, "No Title," 2017.

[24] Z. Lu and Y. Liu, "An incremental crack growth model for multi-scale fatigue analysis," no. May, pp. 1–9, 2009.

[25] C. L. Y. Yeong and S. Torquato, "Reconstructing Random Media I and II," *Phys. Rev. E*, vol. 58, no. 1, pp. 224–233, 1998.

[26] T. Peng, A. Saxena, K. Goebel, Y. Xiang, S. Sankararaman, and Y. Liu, "A novel Bayesian imaging method for probabilistic delamination detection of composite materials," *Smart Mater. Struct.*, vol. 22, no. 12, 2013.

[27] B. L. Bramfitt and B. S. Corporation, "Structure / Property Relationships in Irons and

Steels," *Met. Handb. Desk Ed. Second Ed.*, pp. 153–173, 1998.

[28] Z. Li, S. Schmauder, and M. Dong, "A simple mechanical model to predict fracture and yield strengths of particulate two-phase materials," *Comput. Mater. Sci.*, vol. 15, no. 1, pp. 11–21, 1999.

[29] C. J. Butz, S. Hua, J. Chen, and H. Yao, "A simple graphical approach for understanding probabilistic inference in Bayesian networks," *Inf. Sci. (Ny).*, vol. 179, no. 6, pp. 699–716, 2009.

[30] W. Liu, K. Yue, and J. Zhang, "Augmenting learning function to Bayesian network inferences with maximum likelihood parameters," *Expert Syst. Appl.*, vol. 36, no. 2 PART 2, pp. 3497–3504, 2009.

[31] J.-P. Tovee, "Microstructural influence on the effects of forward and reverse mechanical deformation in HSLA X65 and X80 line pipe steels," p. 231, 2014.

[32] J. Kocijan, R. Murray-Smith, C. E. Rasmussen, and A. Girard, "Gaussian process model based predictive control," *Response*, vol. 3, no. DP-8710, pp. 2214–2219, 2004.

[33] J. Qu Nonero-Candela, J. M. De, C. E. Rasmussen, and C. M. De, "A Unifying View of Sparse Approximate Gaussian Process Regression," *J. Mach. Learn. Res.*, vol. 6, pp. 1939–1959, 2005.

[34] D. Büche, N. N. Schraudolph, and P. Koumoutsakos, "Accelerating Evolutionary Algorithms With Gaussian Process Fitness Function Models," *Syst. Man, Cybern. Part C Appl. Rev. IEEE Trans.*, vol. 35, no. 2, pp. 183–194, 2005.

[35] M. L. Zhang and Z. H. Zhou, "ML-KNN: A lazy learning approach to multi-label learning," *Pattern Recognit.*, vol. 40, no. 7, pp. 2038–2048, 2007.

[36] S. B. Imandoust and M. Bolandraftar, "Application of K-Nearest Neighbor (KNN) Approach for Predicting Economic Events : Theoretical Background," *Int. J. Eng. Res. Appl.*, vol. 3, no. 5, pp. 605–610, 2013.

[37] S. Y. Han, S. Y. Shin, S. Lee, J. H. Bae, and K. Kim, "Effect of cooling conditions on microstructures and mechanical properties in API X80 linepipe steels," *J. Korean Inst. Met. Mater.*, vol. 47, no. 9, pp. 523–532, 2009.

[38] F. Tahir, S. Dahire, and Y. Liu, "Image-based creep-fatigue damage mechanism investigation of Alloy 617 at 950 °C," *Mater. Sci. Eng. A*, vol. 679, no. October 2016, pp. 391–400, 2017.

[39] S. Dahire, F. Tahir, Y. Jiao, and Y. Liu, "Bayesian Network inference for probabilistic strength estimation of aging pipeline systems," *Int. J. Press. Vessel. Pip.*, vol. 162, no. January, pp. 30–39, 2018.

MSU contributions

Outline:

LIST OF FIGURES

LIST OF TABLES

CHAPTER 1 Near-field Microwave Imaging system design and optimization

Advances in material science and manufacturing has produced complex engineering structures that can operate in fatigue and/or harsh environment. Infrastructure involving these structures in growing at very fast for which rapid inspection techniques are needed for their periodic maintenance. This is critical for ensuring the quality of service and reliability of structures in harsh environments. Thus, rapid nondestructive evaluation (NDE) technologies that can detect and characterize damage is of great interest at present. The developing of the micro-electromagnetic sensing prototype is continued from CAAP14 as proposed in the project. Although the Near-field Microwave Imaging (NMHI) system is able to provide desirable diagnostic capabilities for applications in several areas. Speed is a big issue of current single sensor imaging. To improve the scanning speed and develop a reliable rapid NMHI system, fast imaging researches include multi-channel sensor design, innovative continuous data acquisition and sparse sensing method have been studied. This system is capable of imaging different defect profiles as well as sub-surface defects in dielectric materials using both amplitude and phase information of the reflected signals. The method was tested on various datasets with successful implementation of signal recovery using numerical optimization. A multi-modal correlation analysis between Digital Image Correlation (DIC) and NMHI data is studied as a potential in-situ & ex-situ application of the system. The results show that the developed system provides good correlation with measured tensile strain and the dielectric properties of PA11 material, which demonstrates this fast, non-contract method as a promising alternate modality.

1.1. Multi-channel sensor prototyping

A multi-channel scanning sensor and the control circuit for the multi-channel scanning sensor for improving the scanning speed. The innovative design of the control circuit shows in Fig. 1-1(a). Compared with the current experiment, shown in Fig. 1(b), the control circuit compresses the directional coupler, RF to AC converter and data collection together to perform the same function. The control circuit uses a microcontroller to control the input and receive signal. There is no connection between data processing and receiving signal in the control circuit design, which will reduce the scanning time.

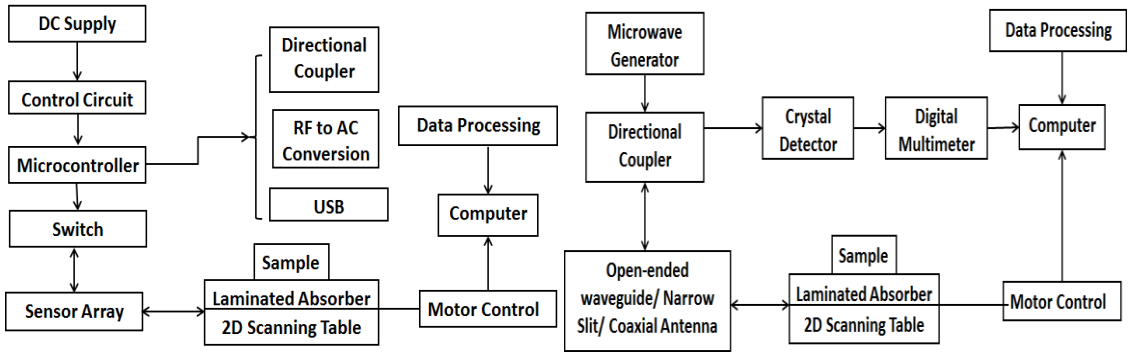

(a) Improved design with Control circuit (b) Current experiment design

Figure 1-1 Design comparison of control circuit and current experiment setup

The control circuit schematic is shown in above figure. Several difficulties have been overcome while designing the control circuit. First is how to split the signal equally to each channel. This is important to the experiment to make sure the signal level is equal. Since the operation frequency of the scanning sensor is at 3GHz, it is difficult to avoid the noise if a long traces are used on PCB. Therefore, instead of building a splitter, a high speed switch has been selected to control the signal. The switch will allow the signal transfer to each probe sequentially. This will avoid the noise generated between the traces, also help avoid the noise that generate between the probes. The second problem we encountered during the design was how to store the return signal data. The goal of the design is for the field testing in the future. How to effectively store the data is important. Instead of using NI DAQ card as we do in our experiment, we chose to use a USB port for storing data for later processing. This will allow the design to be portable for future field testing. The USB port will also help reduce the scanning time since there is no data processing involved. The last question we had during the design process is how to generate the maximized input the signal. Even though the scanning sensors are designed for 3GHz signal, there will be slightly difference between each probe due to the machine error. To be able to adjust the frequency to maximize the signal would be another requirement for the control circuit. We chose Voltage Control Oscillator (VCO) to control the input signal. This will give us the freedom to adjust the input signal to obtain the better resolution.

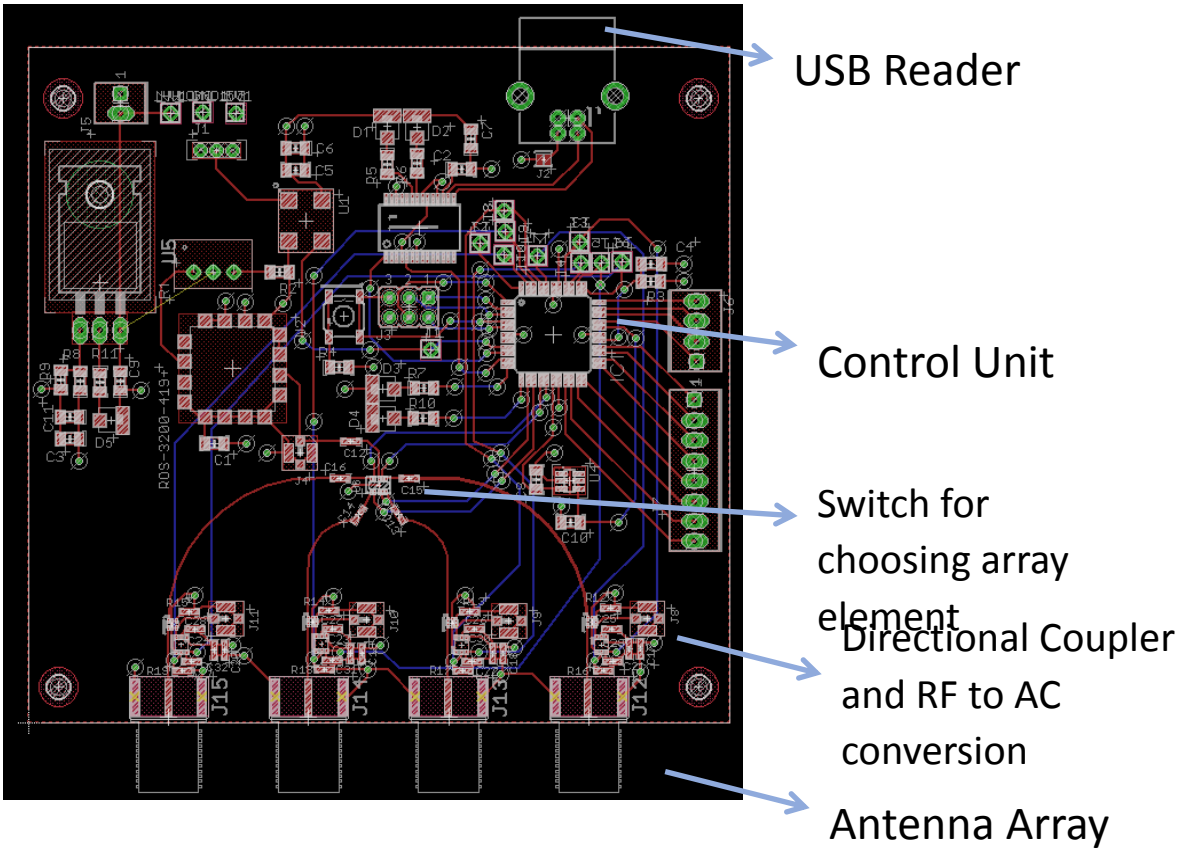

Figure 1-2 Control Circuit Design

The fabricated control circuit board and array antenna show in the following figure. The size of the circuit is approximately 8cm by 8cm. The next step is to program the IC to control the high speed switch for each element of array to radiate and receive signal. The design of the control circuit also has the ability for future expansion to up to 8 channels.

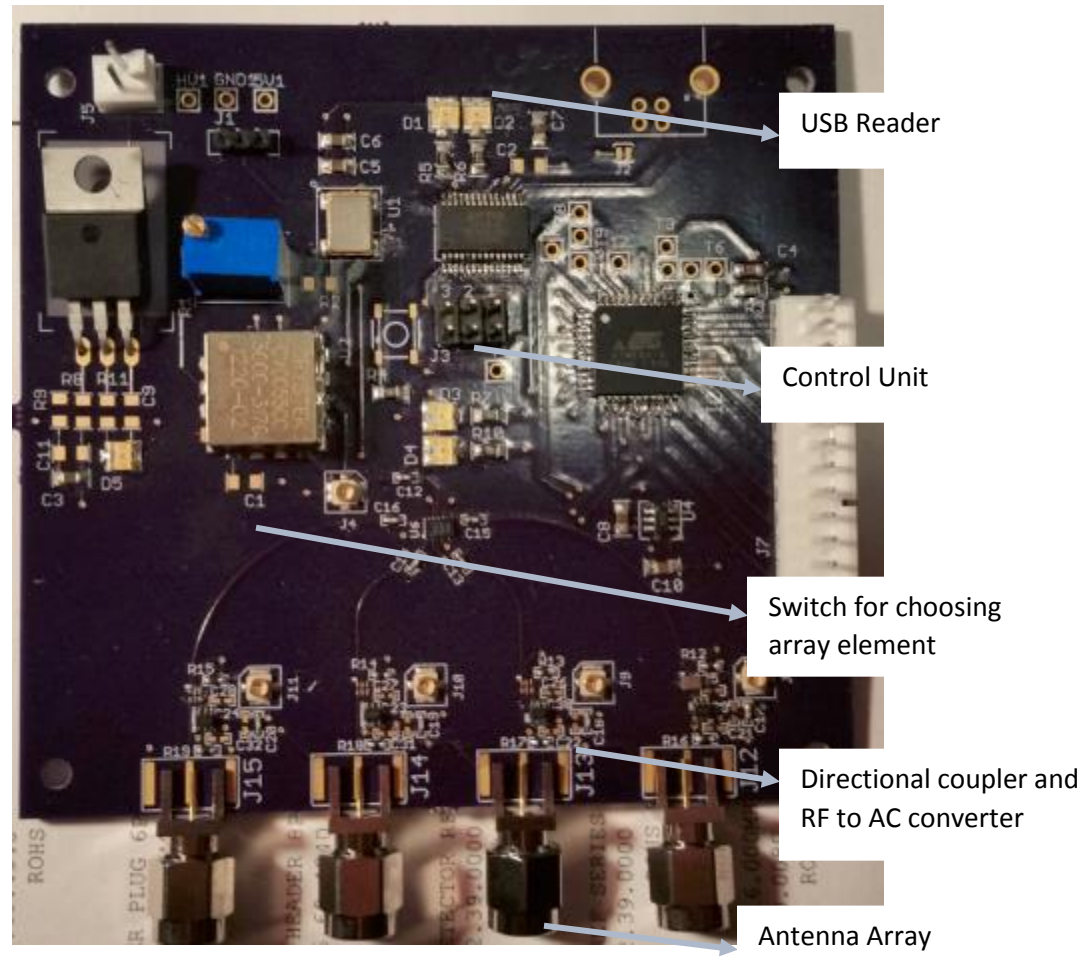

Figure 1-3 Control Circuit and Antennas for multi-channel sensor.

1.2. 3D Model of Near-field Microwave Sensing

In order to have a better understanding of the NMHI system and have a good reference to the experiment results, a 3D numerical simulation have been studied. For ideal lossless dielectric with excitation J, Maxwell equation can be written as:

$$-\nabla \times \mathrm{E} = \mathrm{j}\omega\mu\mathrm{H} \quad (1)$$

$$\nabla \times \mathrm{H} = \mathrm{j}\omega\epsilon + \mathrm{J} \quad (2)$$

$$\nabla \cdot \mathrm{E} = \frac{1}{\epsilon}\rho \quad (3)$$

$$\nabla \cdot \mathrm{H} = 0 \quad (4)$$

The electric field and Magnetic Field introduce by excitation J can be described by

$$\mathrm{E} = -\mathrm{j}\omega\mu\mathrm{A} - \nabla\varphi \quad (5)$$

$$\mathrm{H} = \nabla \times \mathrm{A} \quad (6)$$

According to Lorentz gauge, the relationship between magnetic vector potential A and electric scalar potential ϕ is:

$$\nabla \cdot \mathrm{A} = -\mathrm{j}\omega\varepsilon\varphi \quad (7)$$

Substitute (5),(6),(7) into (1),(2):

$$\nabla^2 A + k^2 A = -J \quad (8)$$

$$\nabla^2 \varphi + k^2 \varphi = \frac{1}{j\omega\varepsilon}\nabla \cdot J \quad (9)$$

For lossless media, $\mathrm{k} = \omega\sqrt{\mu\varepsilon}$

The solution of vector and scalar Helmholtz equation in the infinite space can be expressed as:

$$\mathrm{A(r)} = \int_v J(r')G(R)dv' \quad (10)$$

$$\varphi = \frac{-1}{j\omega\epsilon}\int_v \nabla' \cdot \mathrm{J}(r')\mathrm{G(R)}\, dv' \quad (11)$$

G(R) is the green function in the infinite space. R is the distance between observation point and the middle of the antenna. $\mathrm{G(R)} = \frac{e^{-jkR}}{4\pi R}$

The Integral form of the EM field can be described by substituting (10),(11) into (5) ,(6) and do vector transformation:

$$\mathrm{E(r)} = -\mathrm{jkZ}\int_v [J(r')G(R) + \frac{1}{k^2}\nabla'.J(r')\nabla G(R)]dv' \quad (12)$$

$$\mathrm{H(r)} = -\int_v J(r') \times \nabla G(R)dv' \quad (13)$$

By applying equivalence principle algorithm, we can get the electric field integral equation of the surface of nylon plate. Equivalence principle algorithm (EPA) was first proposed by Chew in 2006. It based on the Huygens' Principle and exploits cubical surfaces to support equivalent sources. Consider an area with boundary, if the distribution of the source inside of the area is unchanged and outside of the area distribute different source. If the fields generated by those source satisfy the same boundary condition then the uniqueness theorem guarantees that there is only one solution to the problem which means we can find the relationship between source and field from the other pair. For some cases it will bring great convenience to the solve problem with the equivalent source instead of the actual source.

If the V_1 (ε_0, μ_0) is the free space and V_2 (ε_1, μ_0) is a polyamide plate. S is the surface of the polyamide plate and n_1, n_2 are the exterior normal and inner normal.

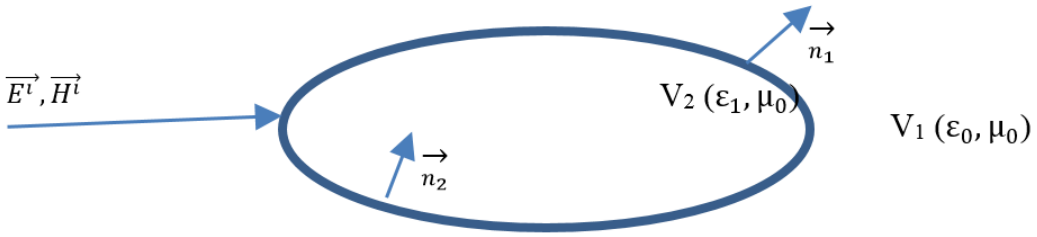

Figure 1-4 Equivalence principle Schematic

V_2 is passive. Surface current and surface magnetic current of S is:

$$\overrightarrow{J_s} = \overrightarrow{n_1} \times \overrightarrow{H_1} \ , \quad \overrightarrow{M_s} = -\overrightarrow{n_1} \times \overrightarrow{E_1} \quad (14)$$

$\overrightarrow{E_1}, \overrightarrow{H_1}$ is the electric field and magnetic field on the S. According to uniqueness theorem, $\overrightarrow{J_s}$ and $\overrightarrow{M_s}$ are the equivalence source of V_2. Set an antenna locate in V_1 perpendicular to V_2. Under the excitation of $\overrightarrow{E^i}$, $\overrightarrow{E_1}$ and $\overrightarrow{H_1}$ on the S can be described as:

$$\overrightarrow{E_1} = \overrightarrow{E^i} + \overrightarrow{E^s} \ , \ \overrightarrow{H_1} = \overrightarrow{H^i} + \overrightarrow{H^s} \quad (15)$$

Therefore $\overrightarrow{J_s}$ and $\overrightarrow{M_s}$ can be written as:

$$\overrightarrow{n_1} \times \overrightarrow{E_1}(\bar{r}) = \overrightarrow{n_1} \times \overrightarrow{E^i}(\bar{r}) + \overrightarrow{n_1} \times \oint [-j\omega u_0 \, g_0 \overrightarrow{J_s} - \frac{j}{\omega \varepsilon_0} \nabla \cdot \overrightarrow{J_s} \nabla g_0] ds \quad (16)$$

$$\overrightarrow{n_2} \times \overrightarrow{E_2}(\bar{r}) = \overrightarrow{n_2} \times \oint [-j\omega u_0 \, g_0 \overrightarrow{J_s'} - \frac{j}{\omega u_1} \nabla \cdot \overrightarrow{J_s'} \nabla g_2 + \overrightarrow{M_s'} \times \nabla g_2] ds \quad (17)$$

$$\overrightarrow{n_1} \times \overrightarrow{E_1}(\bar{r}) = \overrightarrow{n_1} \times \overrightarrow{E^i}(\bar{r}) + \overrightarrow{n_1} \times \oint [-j\omega u_0 \, g_0 \overrightarrow{J_s} - \frac{j}{\omega \varepsilon_0} \nabla \cdot \overrightarrow{J_s} \nabla g_0] ds \quad (16)$$

$$\overrightarrow{n_2} \times \overrightarrow{E_2}(\bar{r}) = \overrightarrow{n_2} \times \oint [-j\omega u_0 \, g_0 \overrightarrow{J_s'} - \frac{j}{\omega u_1} \nabla \cdot \overrightarrow{J_s'} \nabla g_2 + \overrightarrow{M_s'} \times \nabla g_2] ds \quad (17)$$

$$g_i = \frac{e^{jk_i|\bar{r}-\bar{r'}|}}{4\pi|\bar{r}-\bar{r'}|} \quad , k_i = \omega\sqrt{\mu\varepsilon_i} \ (i = 0,1) \quad (18)$$

Since the tangential component of E is continuous across the interface,

$\overrightarrow{n_1} \times \left(\overrightarrow{E_1} - \overrightarrow{E_2}\right) = 0$, $\overrightarrow{n_1} \times \left(\overrightarrow{H_1} - \overrightarrow{H_2}\right) = 0$ (19)

Consider (19), and:

$\overrightarrow{n_1} = -\overrightarrow{n_2}$, $\overrightarrow{J_s'} = -\overrightarrow{J_s}$, $\overrightarrow{M_s'} = -\overrightarrow{M_s}$ (20)

The sum of (17) and (18) is

$\overrightarrow{n_1} \times \overrightarrow{E^i}(\bar{r}) = \overrightarrow{n_1} \times \oint[-j\omega u_0 \overrightarrow{J_s}(g_0 + g_1) + \frac{j}{\omega\varepsilon_0}\nabla \cdot \overrightarrow{J_s}\nabla(g_0 + \frac{\varepsilon_0}{\varepsilon_1}g_1) - \overrightarrow{M_s} \times \nabla(g_0 + g_1)]ds$ (21)

$\overrightarrow{n_1} \times \overrightarrow{H^i}(\bar{r}) = \overrightarrow{n_1} \times \oint[j\omega u\varepsilon_0 \overrightarrow{M_s}(g_0 + \frac{\varepsilon_1}{\varepsilon_0}g_1) + \frac{j}{\omega\mu_0}\nabla \cdot \overrightarrow{M_s}\nabla(g_0 + g_1) + \overrightarrow{J_s} \times \nabla(g_0 + g_1)]ds$ (22)

For far field, $\overrightarrow{E^i}$ can be considered as a plane wave and the value will be constant. For near field, $\overrightarrow{E^i}$ is a spherical wave

$\overrightarrow{E^i}(\bar{r}) = E_0^i r_0 \frac{e^{jk|\overline{r'} - \overline{r_T}|}}{|\overline{r'} - \overline{r_T}|} e^i_{(\overline{r'})}$ (23)

Since $\overrightarrow{E^i}(\bar{r})$ is a function of distance, the value of $\overrightarrow{E^i}(\bar{r})$ is different at different location. Therefore, $\overline{r_T}$ has to be taken into consideration. From above equations, we can calculate the distribution of current and magnetic current on the surface *S* and then we can get the equation of scattered field:

$\overrightarrow{E^s} = \oint[-j\omega u_0 g_0 \overrightarrow{J_s} - \frac{j}{\omega\varepsilon_0}\nabla \cdot \overrightarrow{J_s}\nabla g_0 + \overrightarrow{M_s} \times \nabla g_0]ds$ (24)

Since equation (21), (22) are too complex to solve by analytic method. Therefore we apply numerical method to get an approximate solution. Set nodes r_i (i=1~N) on the surface of V_2.

$u^h(\mathrm{r}, \bar{r}) = \sum_i^m P_i(r)a_i(\bar{r}) = P(r)a(\bar{r})$ (25)

For each nodes assign influence of domain d_i and introduce weight function $W_i(\mathrm{r}- r_i)$.

$u^h(\mathrm{r}, \bar{r}) = P(r)[P^T w(r)P]^{-1}P^T w(r) = \sum_{i=1}^n \varphi_i(r)u_i$ (26)

1.3. Fast imaging acquisition for sensor optimization

For the pervious scanning system, the initial scanning time for a small area is still very long. A scan of 190 mm x 100 mm area with step size 0.635 mm will cover 48,000 spatial locations. The scanning system applies step by step scanning method will stop at each spatial location and calculate spatial value by averaging 3000 samples. Therefore, to complete an entire scan the system will stop 48,000 times and process 144 million samples during the scanning. It will result in a very long operating time. Another disadvantage of step by step scanning system is the strong vibration since the step by step scanning system repeats moving and stop at each spatial location. It not only increases the scanning time but also introduce more noise and inaccuracy.

For a better scanning speed and performance, a continuous scanning method which avoid disadvantages mentioned above is developed. In the continuous scanning system, motor will continuous moving until reach the end of each column instead of stop at each spatial location.

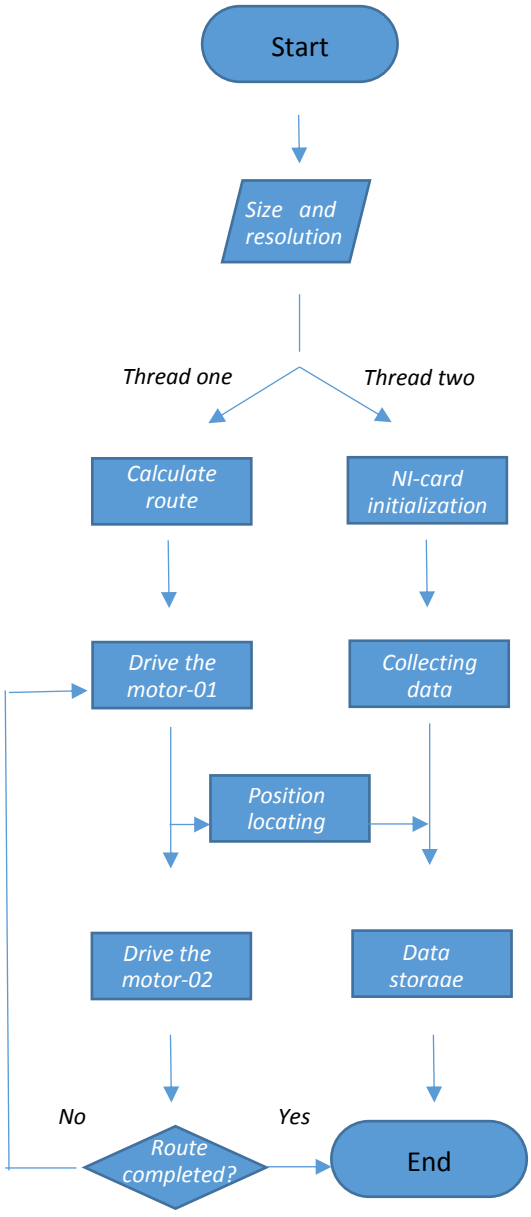

Figure 1-5 Flow chart of the two thread

As Fig.1-5 shown above, a python code which controls two step motors and collects data at same time has been programmed. This code contains two threads. Thread one calculates the route of the motors according to the size of the scanning sample and drives the motors. Thread two collects the data read from NI-DAQ card and records the position current scanning.

After inputting the length and width of the sample and deciding the resolution of the scan, the thread one will calculate the route of the entire scan. The route will cover the sample and the distance between each line is decided by the resolution. In the meantime, thread two will initialize the NI-card such as the communications protocols and sampling rate. Higher sampling rate will give a better result but also require more computational capabilities. When calculation of the route is completed, thread one will drive the motor01 to move the sample and read the feedback from motor01 to determine the position. Thread two keeps collecting the sampling data. Non-stop scanning increase the difficulty of locating point. Therefore, a global variable has been set as the bridge of the two threads to improve the scanning accuracy. Every time the motor01 return a message of status, thread one will check the motor position according to the route plan. The information of location will transmit to thread two via the global variable. When one line has been scanned, thread one will drive the motor02 in order to scan the next line until the route is completed. Thread two will average the samples and store the data into a matrix. At the end of the scan, the matrix will be plot as an image with 'hot' color map and the sampling data before averaging will be saved as raw data.

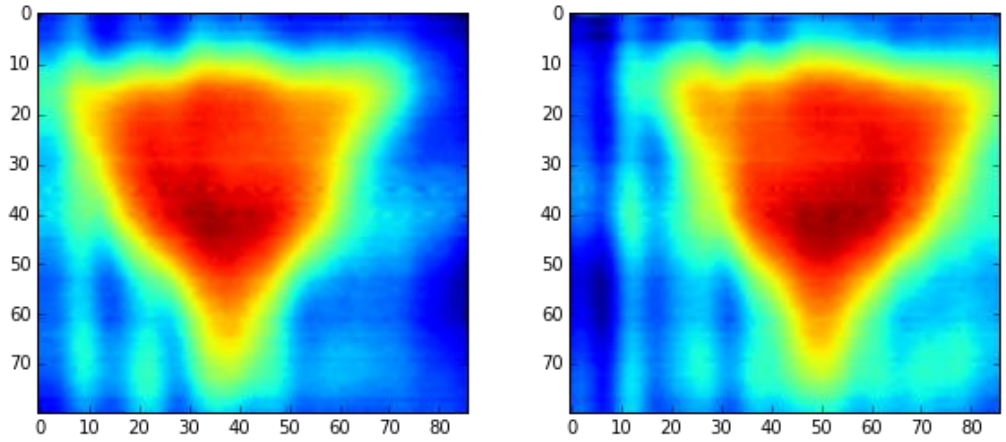

Figure 1-6 Continuous scan results of 2x2 inch2 area: (left) data collected from forward moving and (right) data collected from backward moving.

As Figure shown above, it is the scanning result of a 2x2 square inches area with triangle with the sampling frequency as 100 KHz. It takes 0.86 s for the step motor01 moving over this 2 inches, therefore, 86000 samples will be acquired for each column. The step size of step motor02 in 200 steps per inches. The size of triangle's raw data is 86000x80 since the setup of this result is acquired data every 5 column. By taking mean of every 1000 data, the size becomes 80x86. It takes about 5 minutes for this entire 2x2 square inches scan.

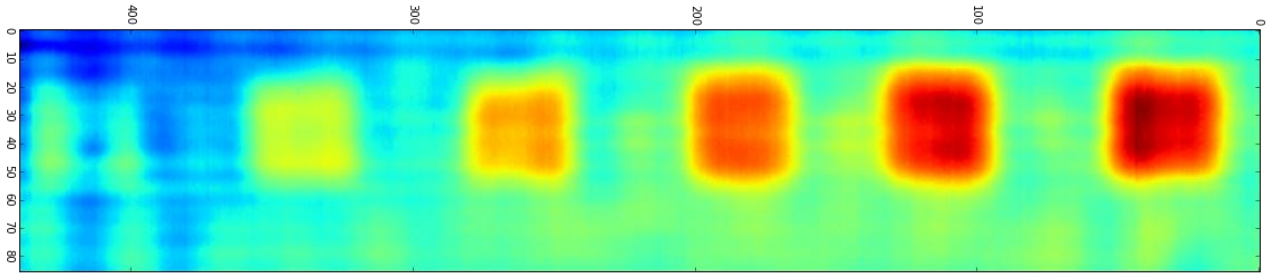

(a). data collected from forward moving

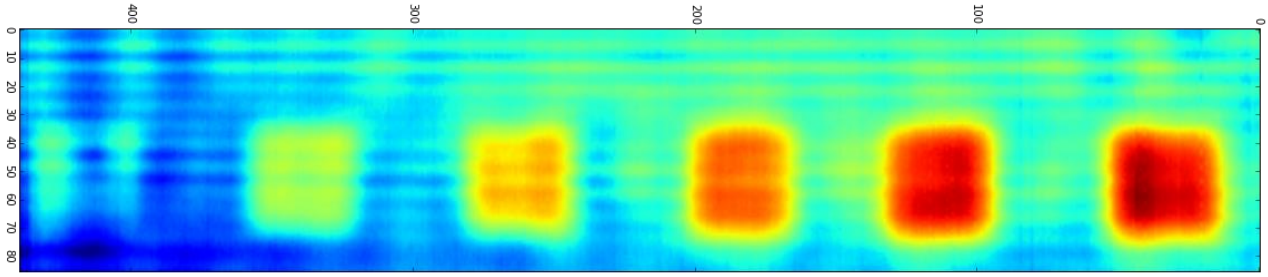

(b). data collected from backward moving

Figure 1-7 Continuous scan results of 2x11 inch^2 area

As Fig. 7. shown above, it is the result image of a 2x11 square inches area. The squares shown in the image are with identical size (1x1 inch^2) and different depth. The depth of the squares from left to right are 1mm, 2mm, 3mm, 4mm, 5mm, 6mm. The size of raw data is 86000x440. By taking mean of every 1000 data, the size becomes 86x440. It takes about 20 minutes for this entire 2x11 square inches scan.

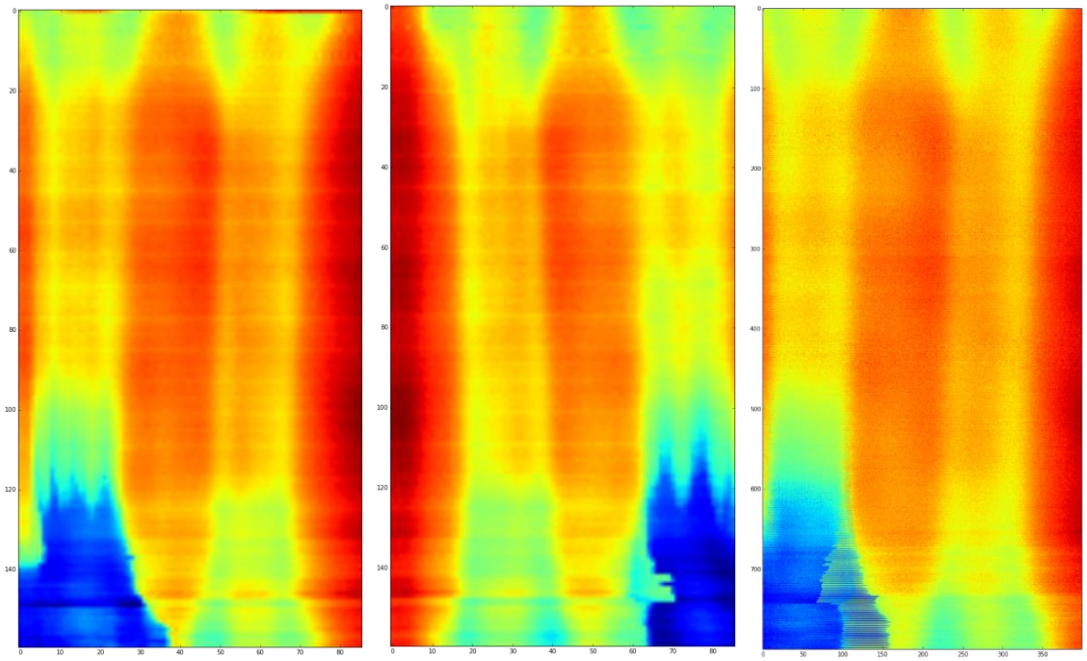

(a). data collected from forward moving (b). data collected from backward moving (c). data collected from step by step

Figure 1-8 Continuous scan results and step by step results of 2x8 inch2 area

The (a) and (b) in Fig. 1-8 are the result image of continuous scan which took about 7 minutes. Image (c) in Fig. 8. is the result of step by step scan which took more than 2 hours.

1.4. Compressive sensing based NMHI

Another way to reduce the scanning time is reduce the sampling rate. Compressive sensing technique, which is the efficient way for signal acquisition is applied to the NMHI system to improve the imaging efficiency for the proposed micro-electromagnetic sensing system. According to the compressive sensing, the original signal be recovered from under sampled data points, by modeling the sampling problem into the underdetermined system of non-linear equations with some prior knowledge of original signal. The prior knowledge for microwave signal is that it shows sparsity in DCT domain. So, the problem can be solved by minimizing the system of non-linear equations using any of the minimization algorithms like basis pursuit, orthogonal matching pursuit, etc.

For this CAAP15 project, CU team has successfully applied the orthogonal matching pursuit (OMP) for solving the underdetermined system of equations. We acquired just the 50% of original signal shown in Fig.2.10 and able to reconstruct the original signal back shown in Fig.2.11.

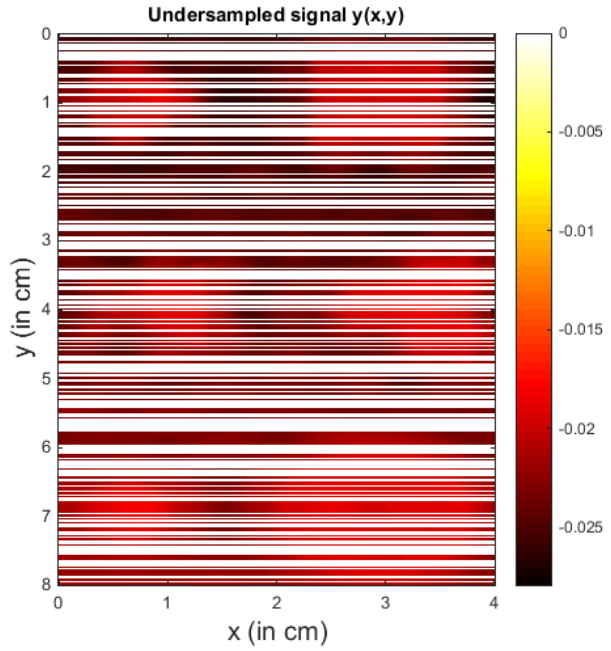

Fig.2.10. 50% Under-sampled Data

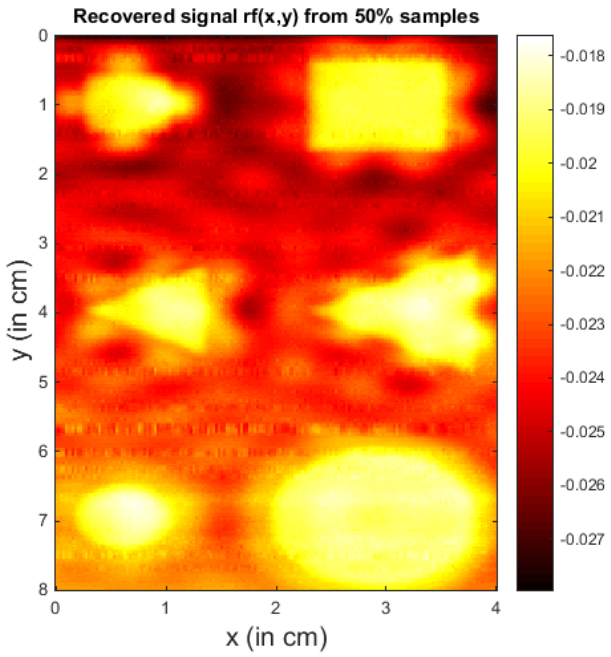

Fig.2.11 Recovered using orthogonal matching pursuit

1.4.1. Method 1: The minimization using OMP algorithm:

The orthogonal matching pursuit algorithm tries to satisfy the error-constraints.

$$\mathrm{x} = \underset{x}{\operatorname{argmin}}\|x\| \, , such\ that\ \|y - Ax\|_2^2 \leq eps$$

where,

y is acquired undersampled signal

A is measurement dictionary

x is the sparse signal

The greedy-OMP selects the atoms with high correlation with current residual at each iteration (step 4) and projects the signal over the span of selected atoms.

$$\gamma = {A_I}^{+} res$$

which, can be solved by using Cholesky factorization and leads to practical implementation.

$$\gamma = (A_I' A_I) A_I' res$$

$A_I' A_I$ is a symmetric and positive definite matrix, which is updating with every iterations.

The cholesky factorization is simply represented as $R'R = A_I'A_I$, where R is the upper triangular matrix.

\\ Implemented Algorithm Steps:

1. Set, $x = 0\ and\ res \leftarrow y$
2. $iter = 0$
3. **while,** $\|\boldsymbol{res}\| > \boldsymbol{eps}$ **, do**
4. $\hat{\imath} := argmax_i|A_i'res|$
5. $I = (I, \hat{\imath})$
6. find, $cholesky\ factorization\ R\ of\ A_i'A_i$
7. $\gamma := Solve\ for\ c\ \{RR^Tc = A_i'res\}$
8. $res = y - A_I\gamma_I$
9. $iter = iter + 1$
10. **end while**

The minimization problem could have number of minima's available; reaching to global minimum is always hard. Using different minimization techniques and different set of constraints results in variation of finding minima. Orthogonal Matching Pursuit algorithm is leading the solution to one of its local minima or a limit point. The thought of finding other minima's with different constraints could have lead us to better solution, so one more minimization algorithm is applied to the same problem with different formulation of constraints called Proximal Gradient Algorithm [2]. The results are shown in Fig. 2.12.

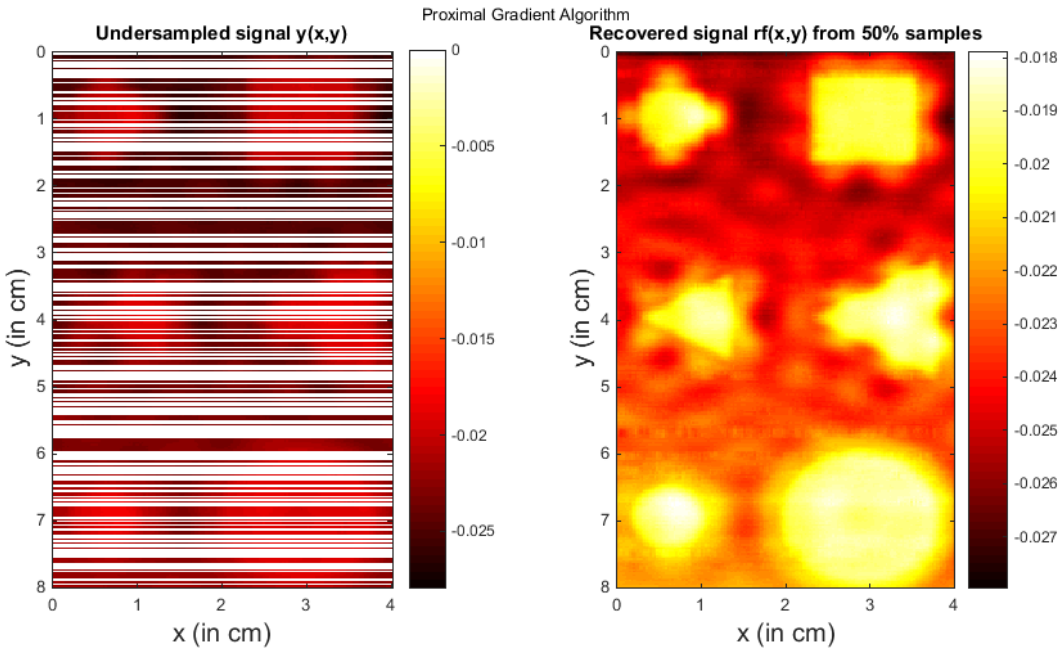

Fig.2.12 Results from Proximal Gradient Method

1.4.2. Method 2: The minimization using Proximal Gradient Algorithm:

The orthogonal matching pursuit algorithm tries to satisfy the error-constraints.

$$\min_x \frac{1}{2}\|Ax - y\|_2^2 + \mu\|x\|_1$$

where,

y is acquired undersampled signal

A is measurement dictionary

x is the sparse signal

\\ Implemented Algorithm Steps:

1. Set, $\mu > 0, t = 1, \tau = eigenvalue\ of\ A'A$
2. $iter = 0$
3. **while,** $\|\boldsymbol{Ax - y}\| > \boldsymbol{eps}$ **, do**
4. $Y^{iter} = X^{iter} + \frac{t^{iter-1}-1}{t^{iter}}\left(X^{iter} - X^{iter}\right)$
5. $Set, G^{iter} = Y^{iter} - \tau^{iter^{-1}} A^*(AY^{iter} - b)$
6. $Set, X^{iter+1} = S_{\tau^{iter}} G^{iter}$
7. $Compute\ t^{iter+1} = \frac{1+\sqrt{1+4\left(t^{iter}\right)^2}}{2}$
8. $iter = iter + 1$
9. **end while**

1.5. Scanning images deconvolution

Another issue for the pervious NMHI system is not able to acquire a clear image directly. The scanning images are blurred in the axial direction by the contributions of point spread function. The results of scanning include not only the propriety of the materials but also the pattern of the antenna. Therefore, an image enhancement method using deconvolution is studied.

Deconvolution is a computationally intensive image processing technique existing in a broad range of signal and image processing fields. It becomes necessary when we want to deburr image for a better performance or further processing. The high-frequency information usually contains the texture characteristic of the target. Due to the point spread function is the low-pass filter, the high frequency of image is suppressed and even lost. Since the image textures are important visual information for the human eyes to detect damaging location, the aim of deconvolution is to reconstruct the high-frequency part. However, the observation noise will be amplified, which means that the deconvolution results may vary from the real solution. Therefore, the deconvolution method should compromise between the performance of the scanning reconstruction and noise amplification.

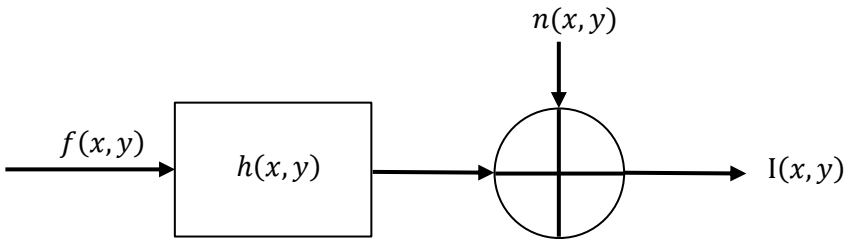

Figure 1-9 model of degraded image

The degraded images can be expressed as follow:

$$\mathrm{i}(\cdot) = h(\cdot) * f(\cdot) + n(\cdot)$$

I(t) is the image we acquire from the scanning, $h(x, y)$ is a pulse response of the linear system which is also known as point spreads function, and $n(t)$ represents noise. $f(x, y)$ is the physical quantity without distortion that we want to solve. If one of the functions $h(x, y)$ or $f(x, y)$ is known, we can use Weiner filtering or iterative restoration to recover the other function. The problem is termed as blind deconvolution if neither $h(x, y)$ or $f(x, y)$ is known and only the output image i(x, y) is available.

1.5.1. Point spread function estimation

In order to solve the deconvolution and get the f(x, y), we first find an estimate of the Point spread function. The first estimate is based on the pattern of the antenna. We first generating a matrix to approximate the point spread function by the following equation:

$$E_\theta \cong -j\eta \frac{I_0 l e^{-jkr}}{4\pi k r^3} sin\theta$$

The size of the matrix is measured the blurred part around square on the scanning image.

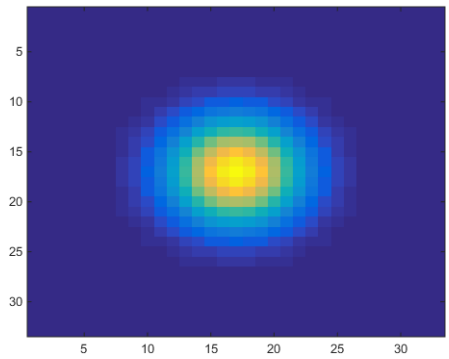

Figure 1-10 The estimation of the point spread function

Since the estimation contains some very small value or even zero, and matrix is in the denominator during the calculation, we use the Weiner filtering to solve the deconvolution instead of divide directly.

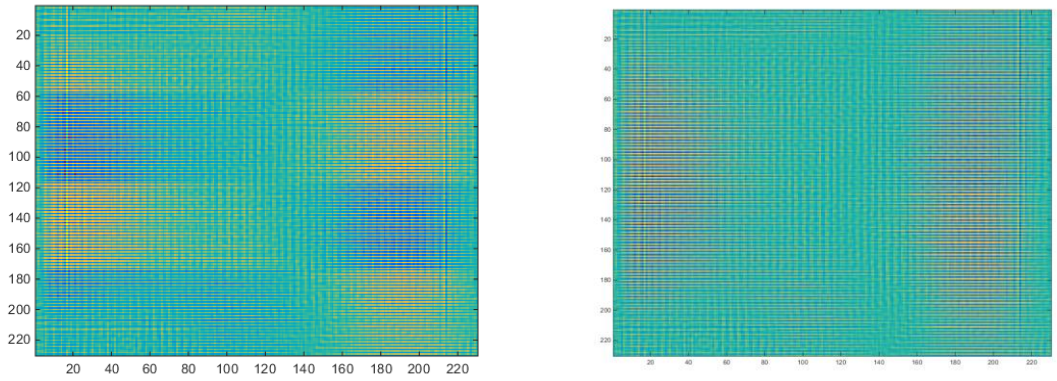

Figure 1-11 results of the deconvolution

To a certain extent, we can see the square in the figure 3. However, it is unclear and still very blurry. Another approach is estimating the point spread function by deconvoluting the f(x, y) from the i(x, y). Although f(x, y) is unknown and need to be solved, we can get an approximation $f'(x, y)$ by observing the scanning object. Then the point spread function estimation $h'(x, y)$ can be solved by the following equation if we ignore the noise.

$$h'(\cdot) = \text{ifft}(\text{fft}(\text{i}(\cdot))/\text{fft}(f'(\cdot)))$$

In the equation, fft and ifft represent fast fourier transform and inverse fast fourier transform respectively.

We scanned a PA board with a 1-inch by 1-inch square hole six times and stored the data as $i_k(x, y)$, k $\in$ [1,6]. The scanning system acquires 200 data per inch which corresponding to 200 pixels in the image.

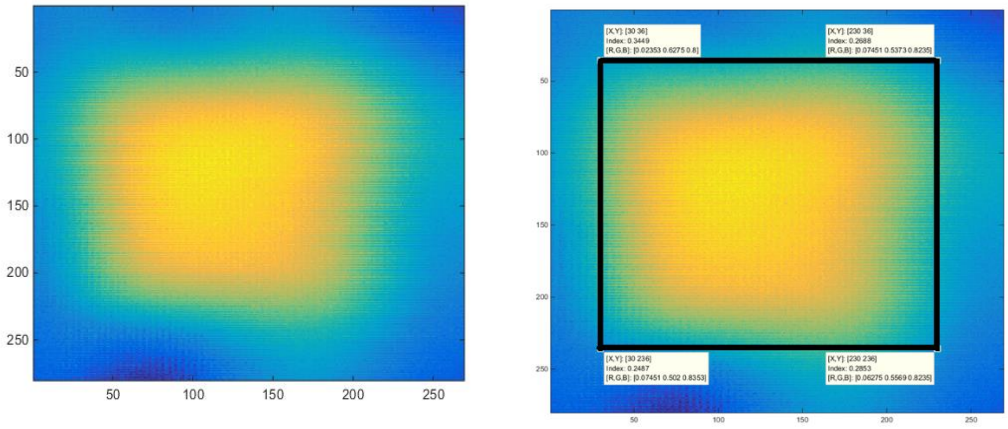

(a) (b)

Figure 1-12 Scanning image and the approximation of the object vertexes

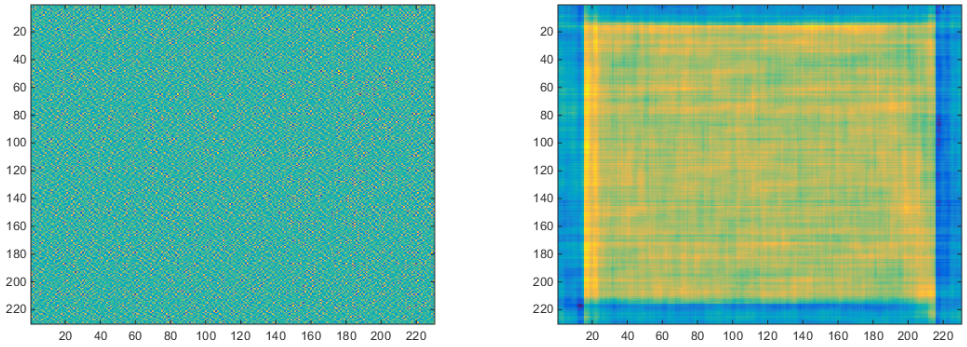

(a) (b)

Figure 1-13 Reconstructed PSF and reconstruct image using the $h'(x,y)$

We draw a 200 by 200 square on the corresponding location in the Matlab as the $f'(x,y)$. Then $h'_k(x,y)$ can be solved by equation. By averaging $h'_k(x,y)$ we can get the estimate of the point spread function. However, the result is not accurate since the poor knowledge about f(x,y). The f$'(x,y)$ we used may have a big difference from the actual physical quantity. The estimate of the point spread function need to be improved since the pattern should be central symmetry and have the greatest value at the center.

1.5.2. Blind deconvolution

Blind deconvolution is very complicated since we have to infer both the original object and the point-spread function. There are many methods and can be divided into two categories, statistical approach and deterministic approach. We study both two methods and in this quarter we implemented one of the statistical deconvolution algorithm on the near-field microwave microscopy system.

Richardson–Lucy deconvolution algorithm is a statistical approach which based on the Maximum Likelihood and developed from Bayes's theorem.

$$\mathrm{P}(x|y) = \frac{\mathrm{P}(y|x)P(x)}{\int \mathrm{P}(y|x)P(x)dx}$$

The $\mathrm{P}(x|y)$ is the conditional probability of the event x when event y has happened. If we take the $P(x)$ as the physical quantity f(x) we want to solve, $\mathrm{P}(y|x)$ as the point spread function $h(y,x)$located at x and $P(y)$ as the scanning image $i(y)$, we can get the equation

$$f_{j+1}(x) = \int \frac{h(y,x)i(y)dy}{\int h(y,z)\, f_j(z)dz} f_j(x)$$

The j in the equation is the iteration number. If the point spread function is known, the f(x) can be solved by the following equation

$$f_{j+1}(x) = \left\{\left[\frac{i(x)}{f_j(x) \otimes h(x)}\right] \otimes h(-x)\right\} f_j(x)$$

Since we already know the scanning image i(x) and the point spread function $h(x)$, all we need to do is iterating the equation until convergence with an initial guess of the $f(x)$.

In the blind deconvolution both $h(x)$ and the $f(x)$ is unknown and need to be calculate in the previous iteration.

$${h_{j+1}}^{k}(x) = \left\{\left[\frac{i(x)}{{h_j}^{k}(x) \otimes {f}^{k-1}(x)}\right] \otimes f^{k-1}(-x)\right\} {h_j}^{k}(x)$$

$${f_{j+1}}^{k}(x) = \left\{\left[\frac{i(x)}{{f_j}^{k}(x) \otimes h^{k}(x)}\right] \otimes h^{k}(-x)\right\} {f_j}^{k}(x)$$

We have implement this algorithm with the testing data. The value range of the scanning data is around -0.003. Therefore, in order to get the data prepared for the following process, we should First normalize the scanning data.

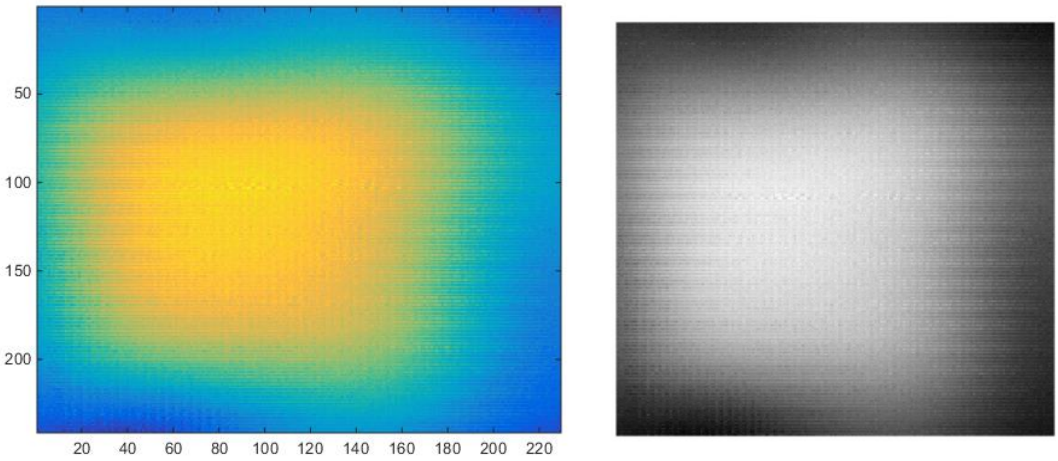

Figure 1-14 Scanning result and normalized grayscale image

Then we should make an initial guess about the size of the point spreads function. The size of the point spreads function is critical and will have more effect on the result of the deconvolution. It can be determined by measuring the blurred part around a noticeably sharp object on the scanning image.

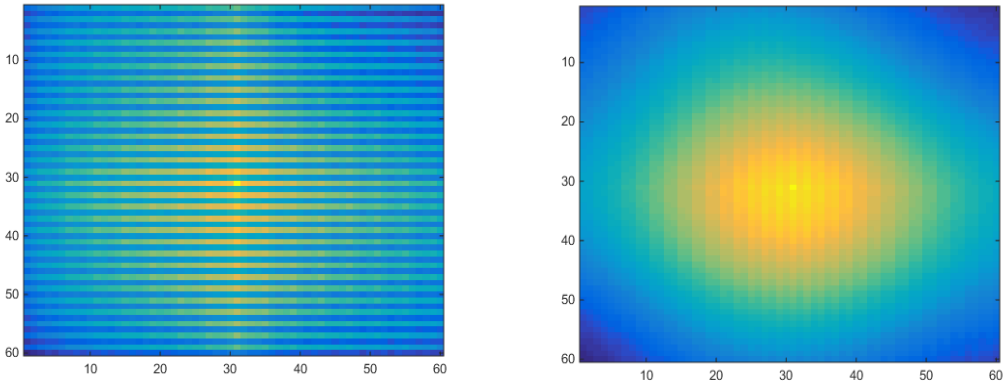

(a) (b)

Figure 1-15 (a) restored point-spread function (b) restored point-spread function from down-sampled data

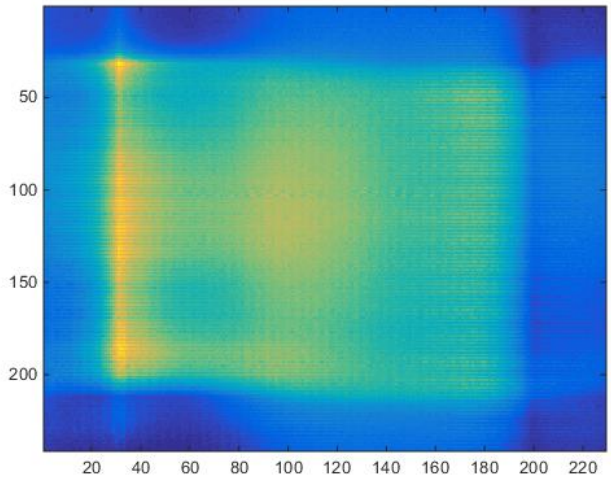

Figure 1-16 deblurred image

In order to improve the result of the deconvolution, a weight matrix has been generated by applying the edge detection. This will let the deconvolution process ignore the high contrast areas and the noise reduce relate to the contrast can be reduced.

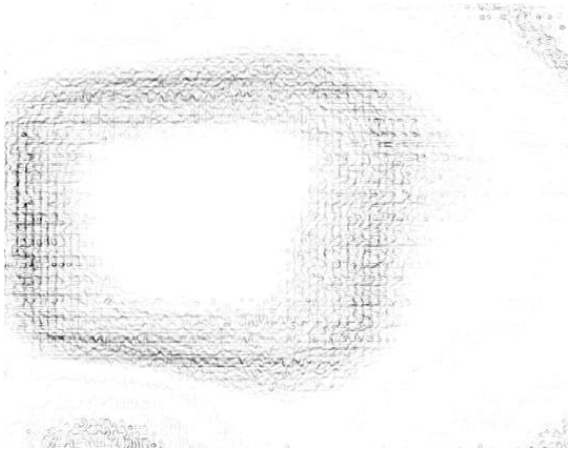

Figure 1-17 result of edge detection

The size of the weight matrix is same as the image. The high-contrast areas have been assigned the zero value and the corresponding pixels in the scanning result will be excluded from the deconvolution processing. The high-contrast areas can be detected by edge detection.

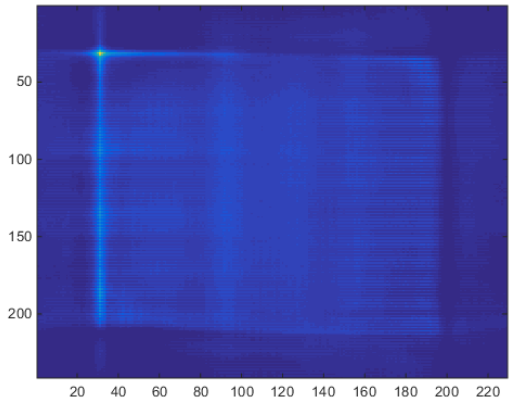

Figure 1-18 deblurred image using weighted method

(a) (b) (c)

Figure 1-19 black and white image of (a) scanning result (b) deblurred image (c) deblurred image using weighted method

In order to have a more obvious contrast, the image is converted to a black and white image. From the figure 1-19 it can be seen that the result of the deconvolution suits the actual shape of object better than the original scanning result.

1.6. Strain estimation using NMHI

Strain measurement is one of the essential elements in materials or structural testing. Knowing the distribution of strain and its value at the critical zones of the structure lead to important indicators for evaluating the strength and life of the structure. Damage initiates in a structure by permanent deformation accompanied by elastic and plastic strains. Plastic strain occurring in the structure indicates an alarming situation that cannot be neglected. In this paper we consider the detection of deformation involving residual elastic strain and plastic strains. We limit our work scope to a very large deformation occurring in the dielectric materials.

The current strain measurement methods for dielectric materials can be divided into contact types and non-contact types. The contact-based methods include the ultrasonic method is one of the most mature and widely used technology. However, the use is complicated on the structure with special geometry and requires skilled personnel to perform the NDE. Also, contact based ultrasonic probes involve application of gel and consumes lots of time. The non-contact modes includes photo elastic method, DIC(Digital image correlation), X-ray, noncontact ultrasound, capacitive and microwave techniques. The DIC

technique is a cost-effective and full-field optical measurement method, which obtains the strain data by relating different digital images taken at various stages of test and tracking blocks of pixels in the images. Although DIC offers accurate strain information of the OUT (object-under-test), it requires continuous data acquisition during the deformation. Thus, it is limited to small structures for real time monitoring and is not applicable to NDE. The X-Ray system is hazardous expensive and not practical for field testing. the ultrasound involves expensive sensing system and the inspection speed is limited.

Therefore, a strain estimation method of dielectric material using NMHI technique is investigated, followed by a multi-modal correlation analysis between DIC and NMHI data.

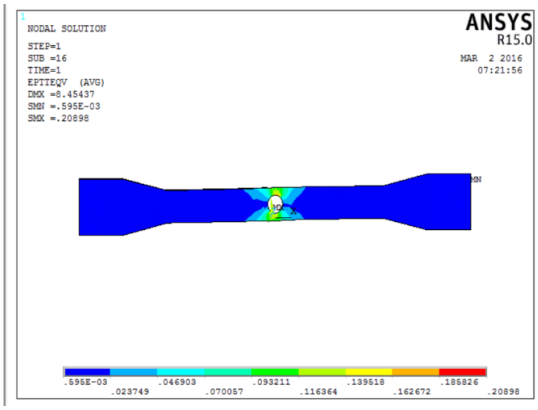

NS_0.7 von Mises strain

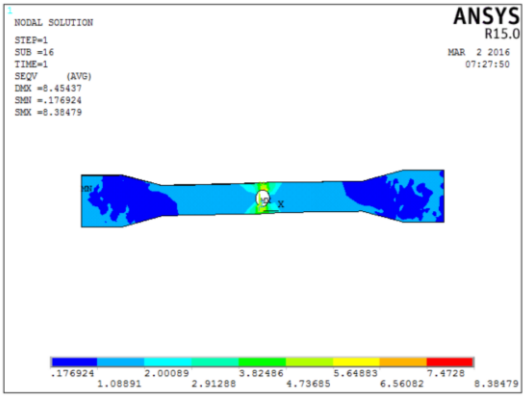

NS_0.7 von Mises stress

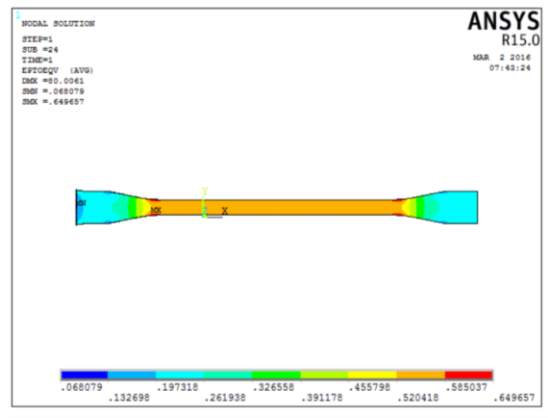

FS_0.7 von Mises strain

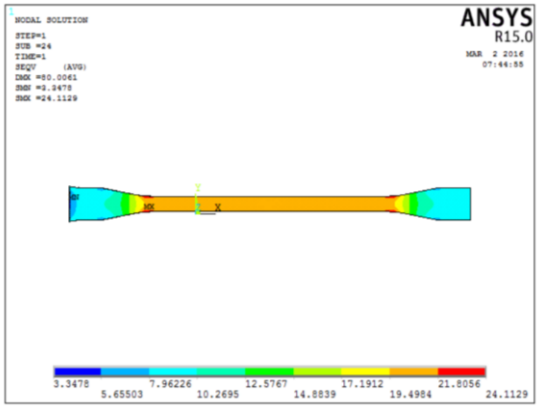

FS_0.7 von Mises stress

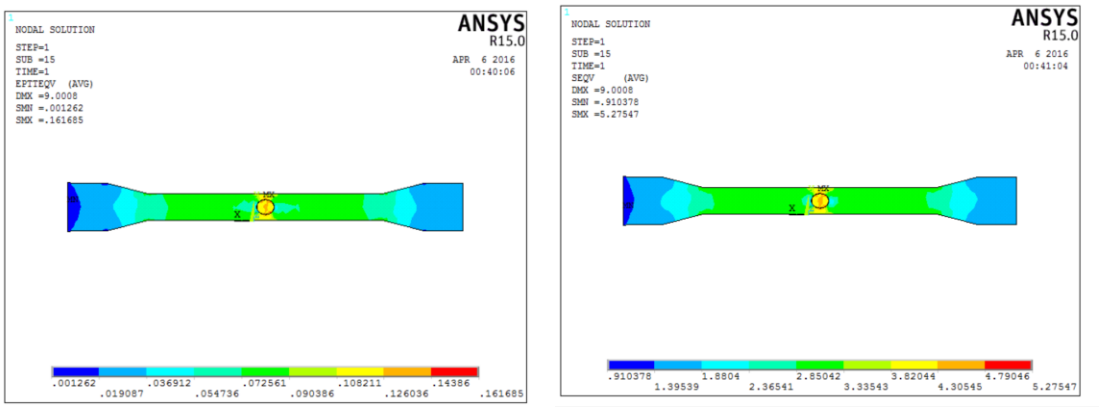

NS_0.3 von Mises strain NS_0.3 von Mises stress

Figure 1-20 von Mises strain and stress simulation

FS is short for full specimen, which means there is no hole on the specimen. NS is short for notched specimen, there is a small round hole on middle of the specimen. 0.7 stands for the percentage of maximum value of displacement when specimens are elongated. For example, if specimen is about to fracture when displacement is 5 cm, 0.7 means specimens are stretched to 3.5 cm.

For the NS specimens, we select section line along the hold root. The 1-D plots of the Von Mises strain have been shown below. As we can see in the picture, the strain reach its peak at the center, where is the location of the hole root. The strength of structure is less then rest part of the specimen due to the hole.

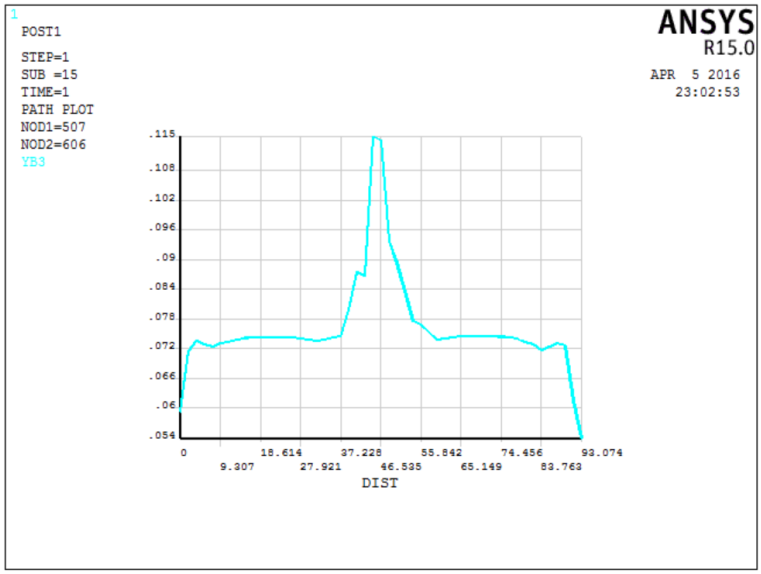

(a) NS_03

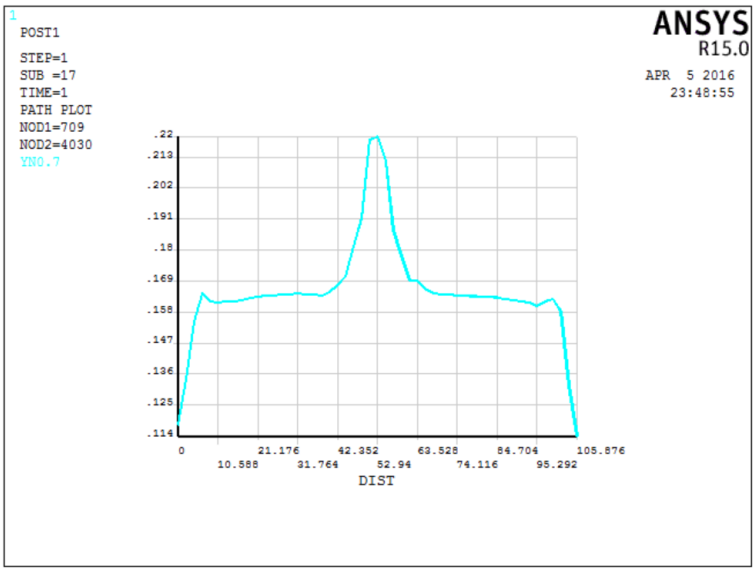

(b) NS_07

Figure 1-21 1-D plot of the von Mises strain

Then we conducted the multi-physics simulation. Use the output of the mechanical simulation as the input of e-field simulation. We select section line along the hold root. The 1-D plots of the E-field have been shown below.

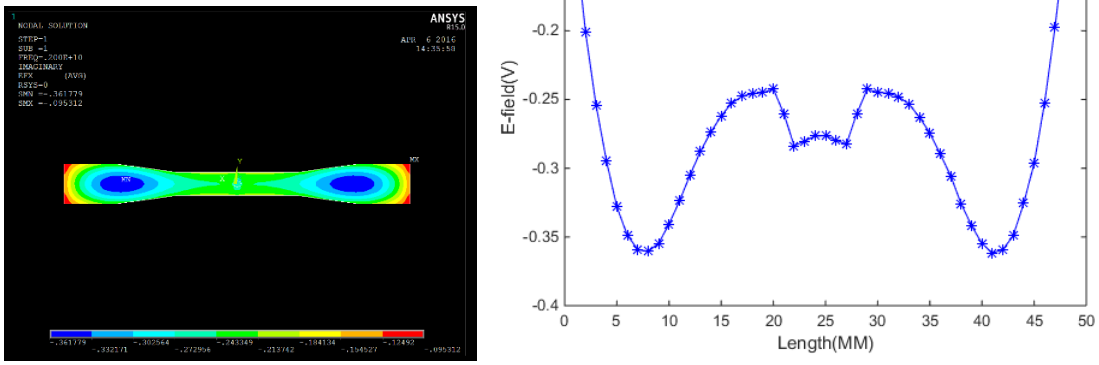

Figure 1-22 Multi-physics simulation of the E- field on the specimen

ASU did tensile testing on the full specimens and notched specimens. We scanned the specimens by nonstop scanning system, in order to compare and correlate the DIC (mechanical properties) and NMMI (micro-electromagnetic properties). The blue stars stands for the data from near field scanning, and the red dash line is the average of scanning data. The solid blue line is the DIC result.

For the notched specimens, we can see that both of the red lines and blue lines are similar to the simulation result. The trends of red lines and blue lines are similar except the middle part where the hole located.

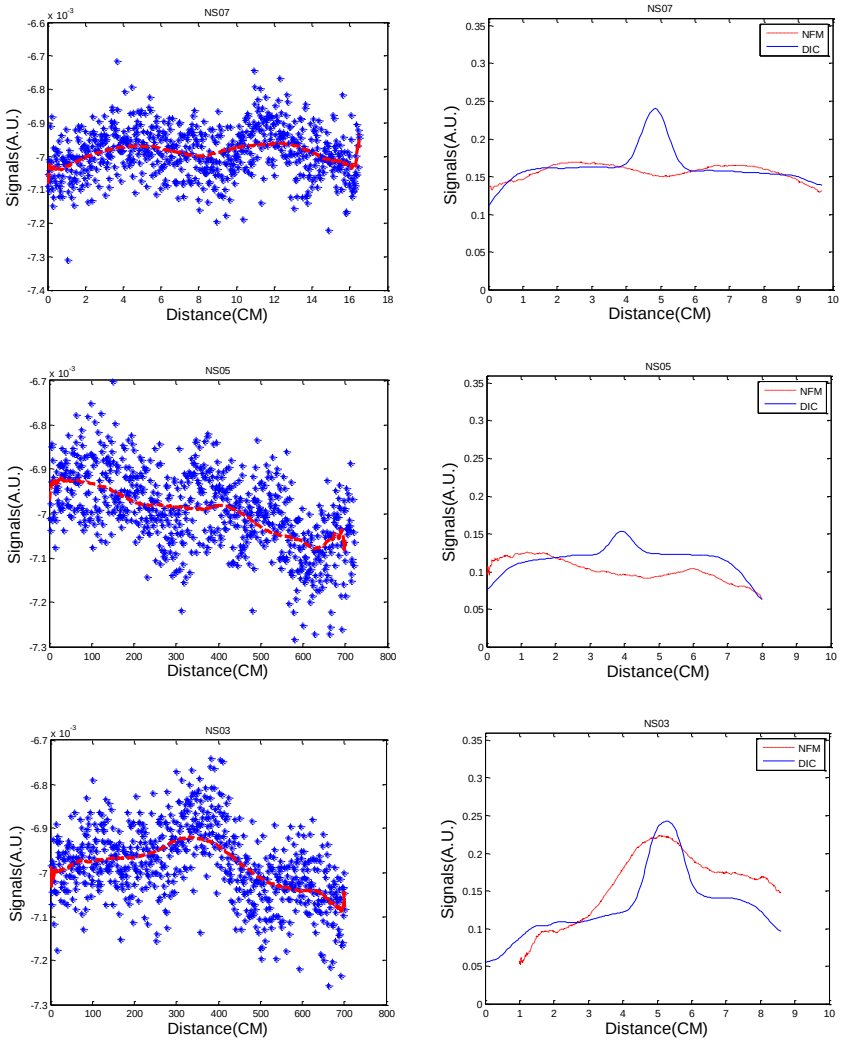

Figure 1-23 scanning results and correlation of the notched specimens

For the full specimens, we can see the trends of the red lines and blue lines are similar. They matched best in FS07 and they matched better in FS05 than FS03.

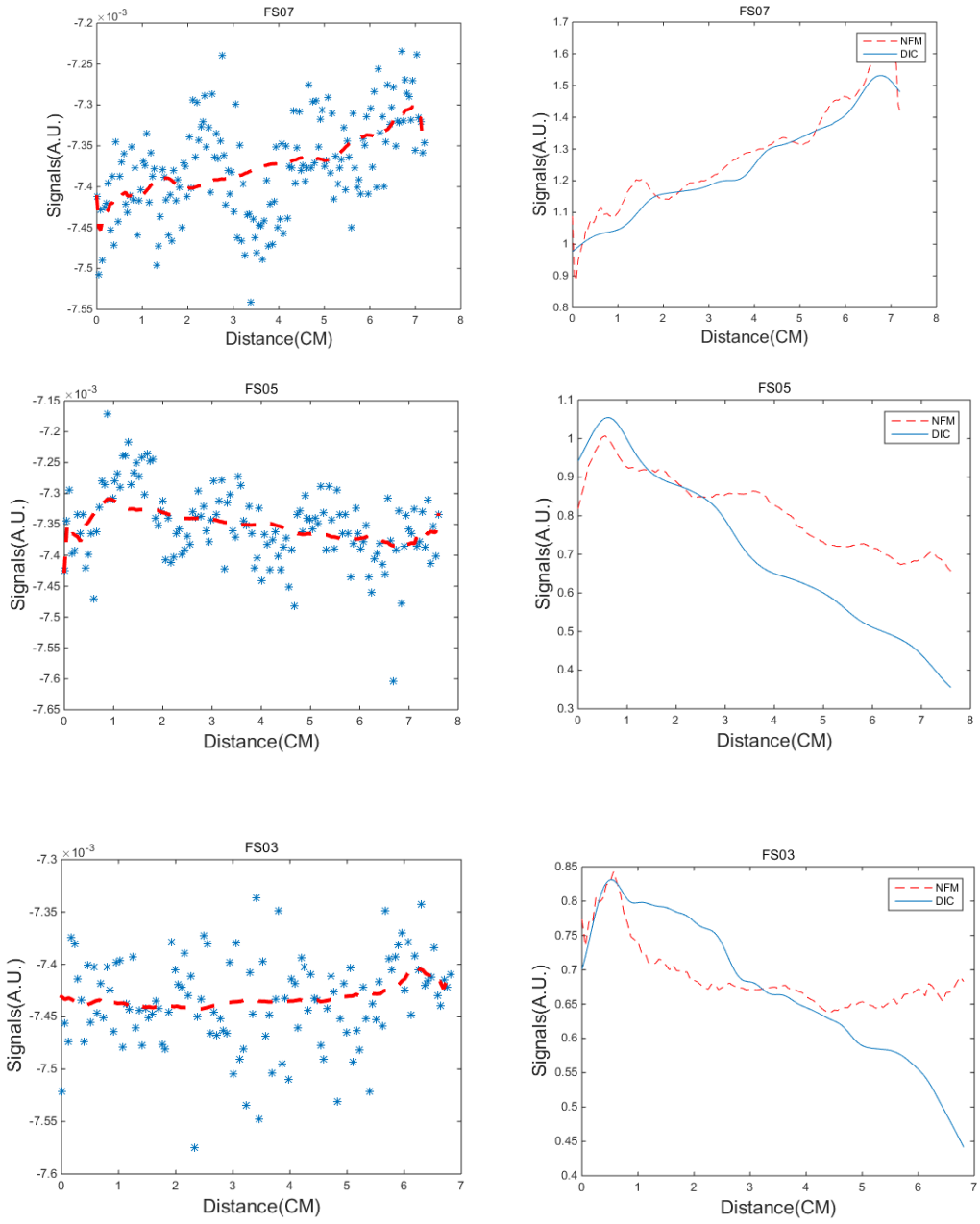

Figure 1-24 scanning results and correlation of the full specimens

As shown in the Fig. 1-25 (a), the curves which represent NMHI data measured from specimen decrease with the Von Mises strain. The best agreement is shown in the plot of 70% elongation whereas discrepancies between the two estimates are seen in 50% elongation. For the 30% elongation, there is significant deviation between the two approach, but they exhibit similar trends. It can be seen that NMHI data has better agreement with DIC under larger elongation or when the strain is higher. This is reasonable since more strain will result in larger change in the dielectric properties. The data in Fig. 1-25 (b) represents NMHI's and DIC's measured strain data for NS. The NMHI data doesn't follow a close trend with DIC's data at center due to the presence of an extra drilled hole on to the specimen. The drilled hole perturbs the fields of NMHI probe and gets significantly more responsive to the shape of physical structure than its dielectric properties. It can be seen that NMHI data follows the stress at the edges as it is the scanning data away from the hole.

CHAPTER 2 Magnetic Barkhausen Noise system development and optimization

MBN is a promising nondestructive electromagnetic method for detecting properties of the ferromagnetic materials. Carrying out information about the microstructure and properties of steels, Barkhausen Noise has been used as a basis for effective Non Destructive Testing methods, opening new areas in industrial applications. It shows excellent performance in evaluating mechanical characterizations and electromagnetic properties of steel by virtue of sensitive to microstructure changes. Based on analysis of some typical features of MBN such as the root-mean-square (RMS) value, the peak value, position and half-width value of profile curve, the relationship between MBN signal and microstructure (grain boundary, grain size, composition), hardness, applied and residual stress, fatigue and damage, and plastic and elastic deformation have been investigated. Ktena et al. compared interlaboratory results about the relation- ship of MBN and grain size and the strain showed that MBN decreases with increasing grain size and increases with strain, consistently. Franco et al. showed linear correlations between different MBN parameters and hardness measurements in the steel SAE 4140 and SAE 6150 with different excitation signal frequency. Stewart et al. analyzed the different parameters of MBN with applied stress include tension and compression and determined residual stress near the edge of the weld with the conclusion

2.1. Preliminary experimental design and setup

The Barkhausen Noise is a magnetic phenomenon produced when a variable magnetic field induces magnetic domain wall movements in ferromagnetic materials. These movements, not continuous but discrete, are caused by defects in the material microstructure, and generate magnetic pulses that can be measured by a coil placed on the material surface.

2.1.1. Design of the experiment

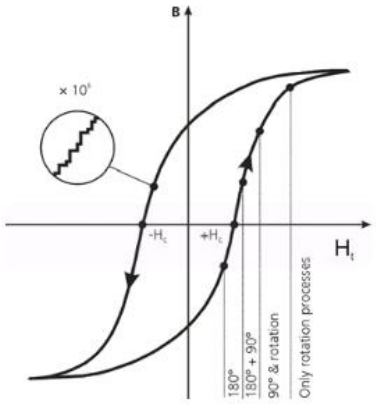

The flow chart of experiment is shown in the Fig. 1. The waveform generator is used to provide the input sin signal with the frequency of 100Hz and the voltage of 1V. Power amplifier has been used to amplify the signal generated by waveform generator. The amplified signal as the excitation signal flow into the excitation coil (55) wrapped around the shape iron. The small signal picks up from the induction coil pass through the low power amplifier and band-pass filter with the pass band 5KHz-200KHz to get the useful Barkhausen noise signal which frequency between 10KHz-100KHz for steel and get rid of the excitation signal and

ambient noise. Then we can use NI PCI device to acquire and store the data in computer for the data processing later. The Fig. 2-2 shows the picture of sensor and the circuit of amplifying and filtering.

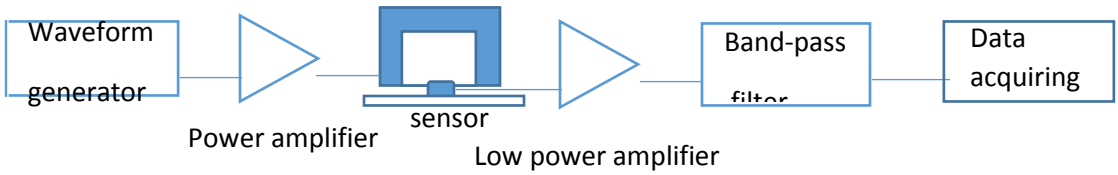

Figure 2-1 design of the experiment

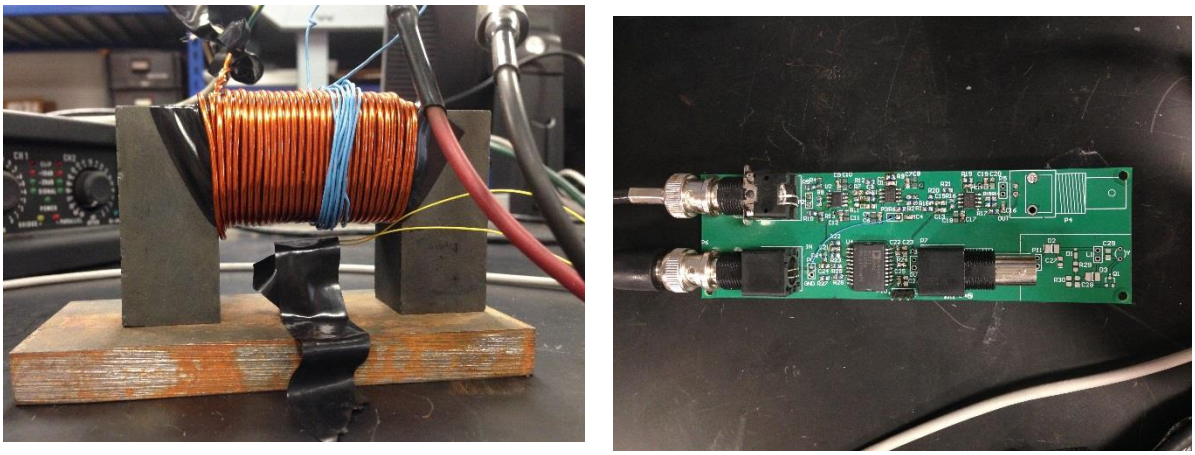

Figure 2-2 sensor and the circuit of amplifying and filtering

2.1.2. Data Acquiring and storing

The processed analog signal can be acquired by NI PCI device combining with LABVIEW sampling program to convert the analog signal into digital signal for further processing in computer. The LABVIEW program diagram is shown in Fig. 2-3. The sampling program consists of establishment of the physical channel, setting of sample clock, reading the sample data and writing the data to file. For the part of setting of sample clock, considering the maximum frequency of the signal and the speed of read and write of the data acquisition equipment, we choose the frequency of 200KHz as sampling rate. For sample mode, we choose continue sampling so that we can get continue image on front panel until we turn off the button. To get the frequency spectrum of the signal directly from front panel, we can carry on the FFT transformation on the original signal. Fig.2-4 shows the front panel when the input is a 100Hz sin signal.

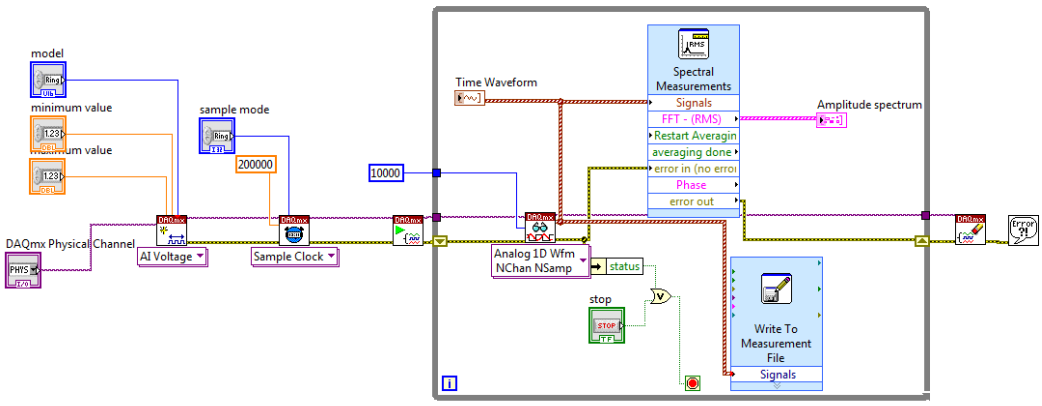

Figure 2-3 LABVIEW program

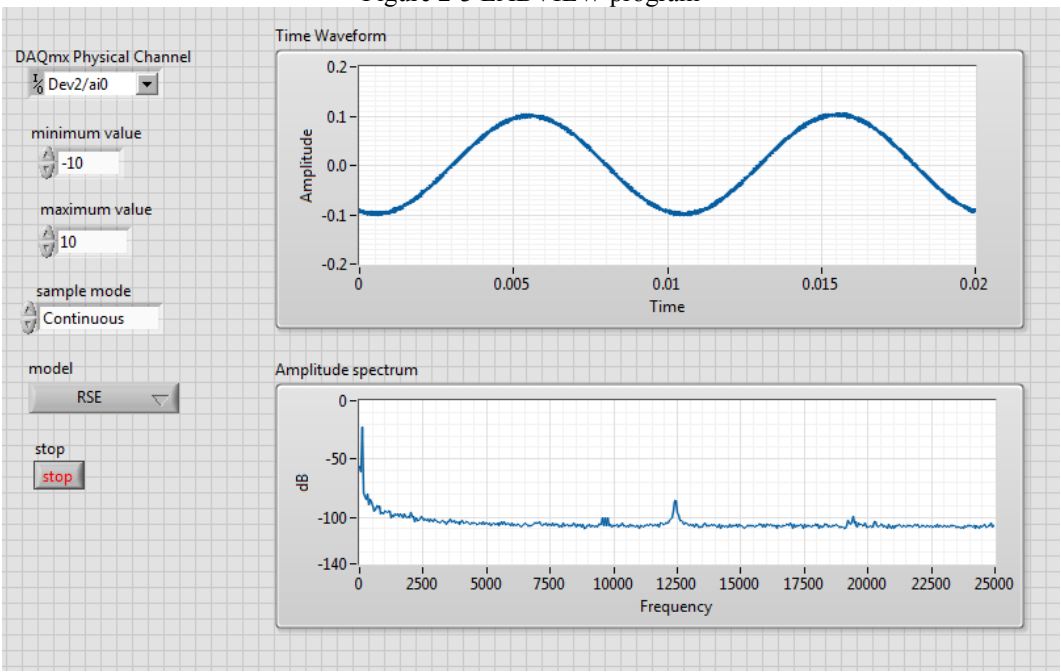

Figure 2-4 front penal of LabView

2.1.3. Data processing with MATLAB

Profile curve refers to the complete outline of the Barkhausen noise in half of the period. The properties of profile curve such as the peak value, the peak time and half-width-value contains many useful information about the microstructure and properties of metals.

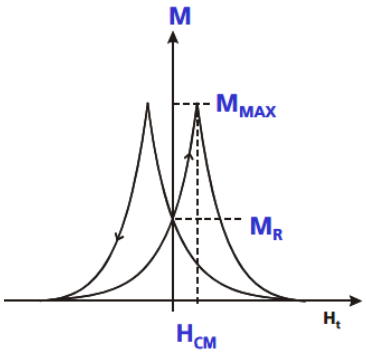

Figure 2-5 Barkhausen noise profile curve

The value of root-mean-square as the most popular methods to show the intensity of the Barkhausen noise is intimately linked with the properties of metals. The expression for calculating the RMS of the noise is shown in below.

$$\Psi_X = \sqrt{\frac{1}{n}\sum_{i=1}^{n} X_i^2}$$

Comparing the waveform from the front panel of the LABVIEW with the acquired data processed by MATLAB, we can find that there is no much different between the two. The signal presents a good periodicity.

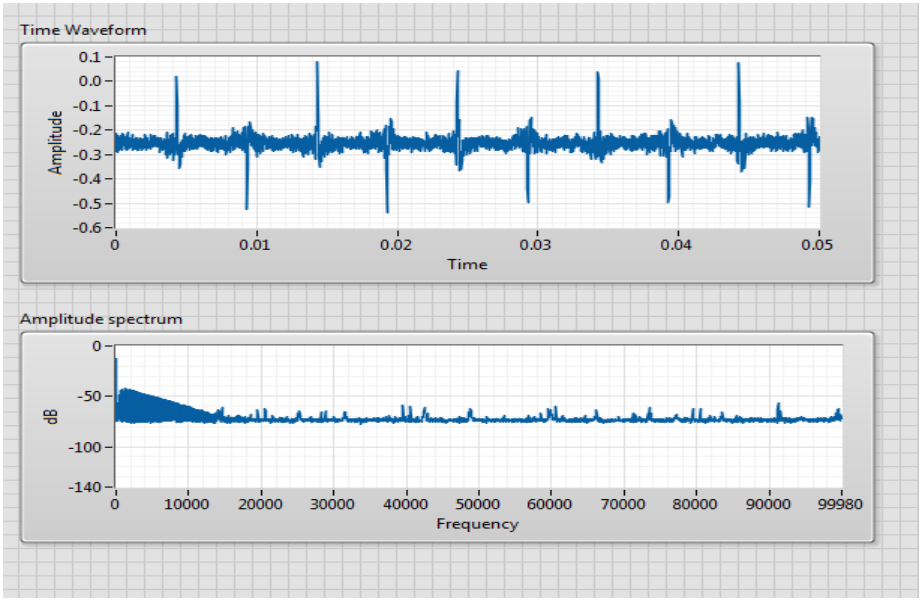

Figure 2-6 waveform from front panel of LABVIEW (excitation signal 100Hz 1V)

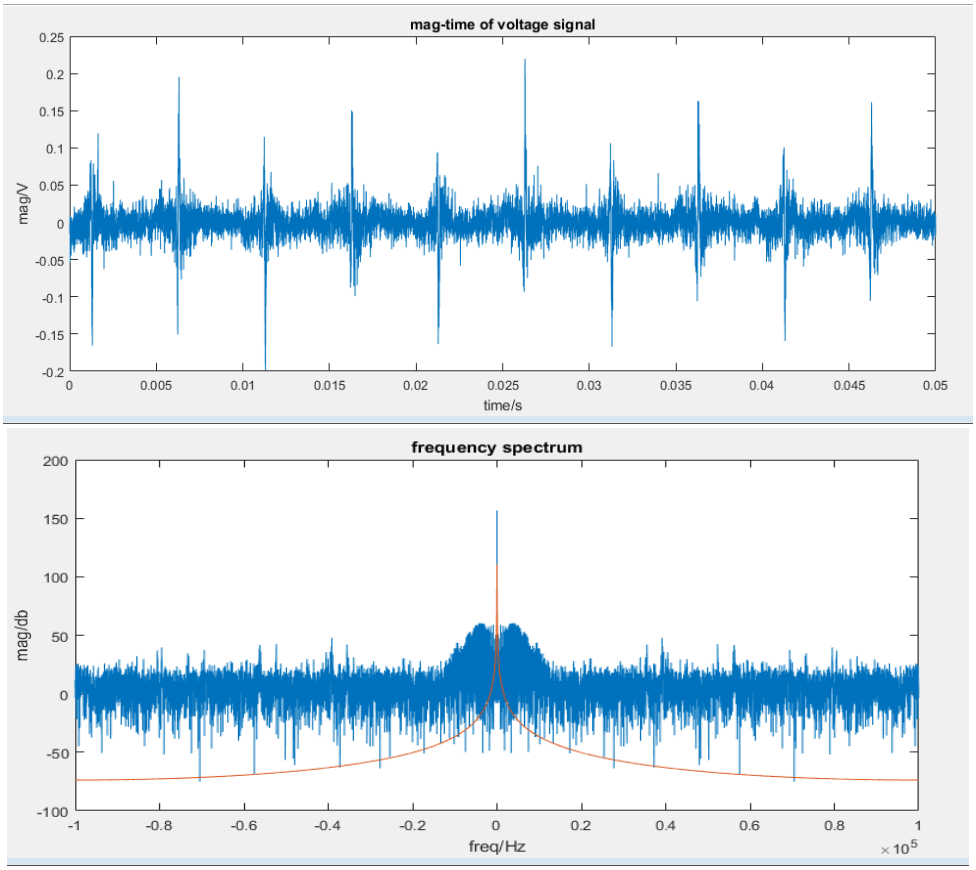

Figure 2-7 Waveform from MATLAB (excitation signal 100Hz 1V)

To get rid of the Gaussian White Noise of the signal and to get a complete signal of one period, we can add 5 periods signal up to get the average signal for one period. The code of MATLAB is shown below.

```
%to get the average of every period of the signal
s=L/2000;      %to calculate the number of period,L is the total number of data
syms a b       %define two variables a,b
a=zeros;       %define one zero array
a=y(1:2000,:);
b=zeros;
%add the data of every periods to array a
for (c=1:s-1)
    b=y(2000*(c)+1:2000*(c+1),:);
    a=b+a;
end
figure
plot(x(1:2000,:),(a-mean(a))/s)  %to get the average of the signal
title('average for 5 periods')
ylabel('mag/V')
xlabel('time/s')
```

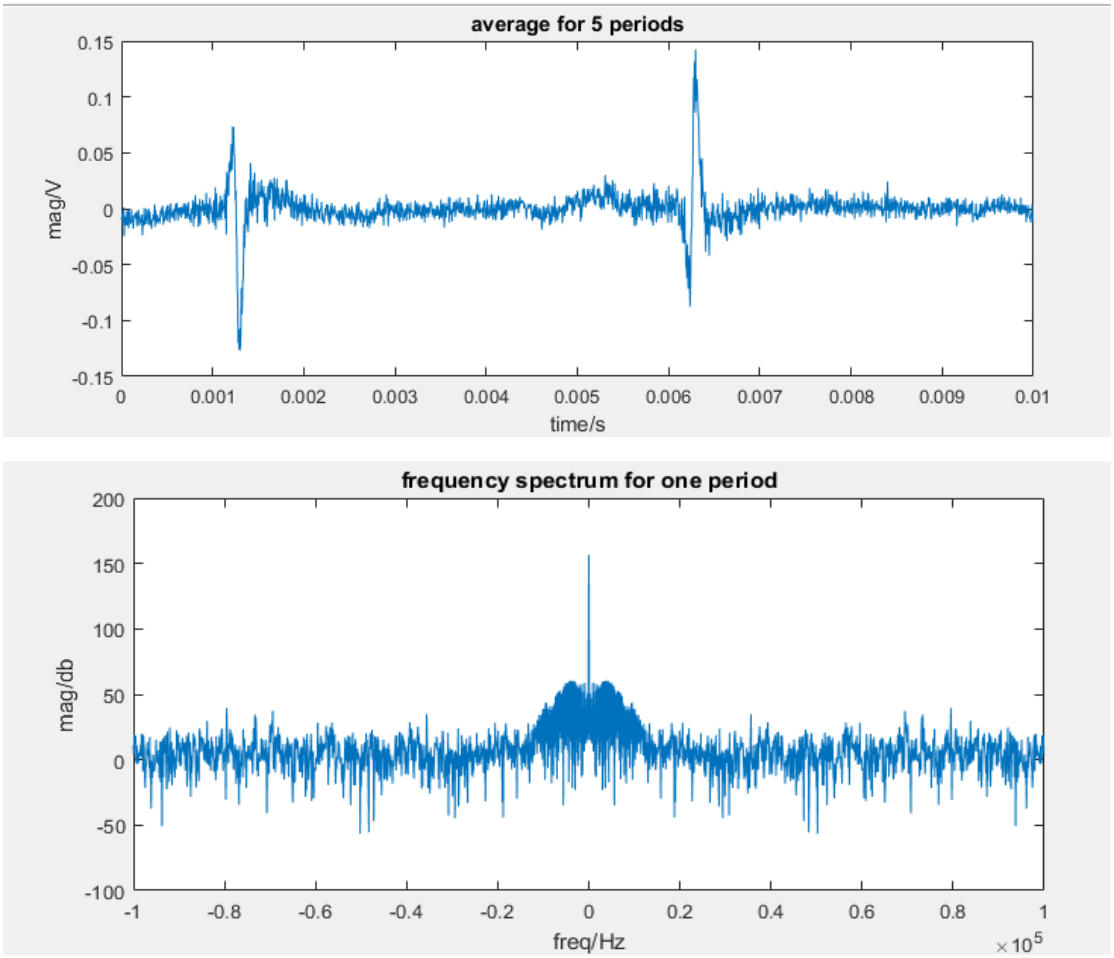

Figure 2-8 one period waveform (excitation signal 100Hz 1V)

From Fig. 2-8, we can find that the waveform looks much better than the original one. It is much smoother compared with the waveform in Fig. 8 for the Guassian White Noise has been removed from the signal.

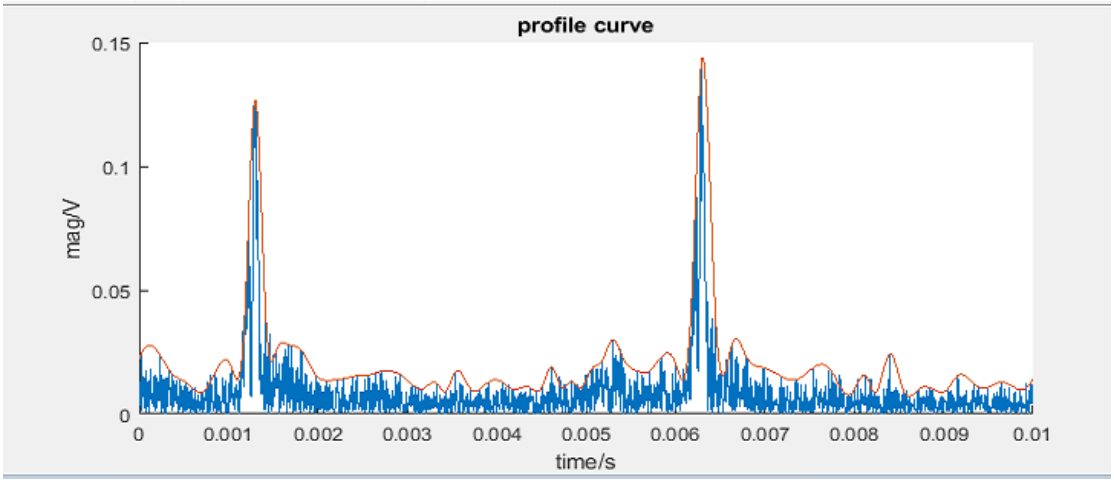

Figure 2-9 profile curve of absolute value of the signal

2.1.4. Influence factors

Comparing the waveform of the signal we get with the Barkhausen noise from other paper(Fig.2-10), there is a little different between the two. Even though the signal we get expresses a good periodicity like the waveform in Fig.2-10, the signal has only one obvious oscillation.

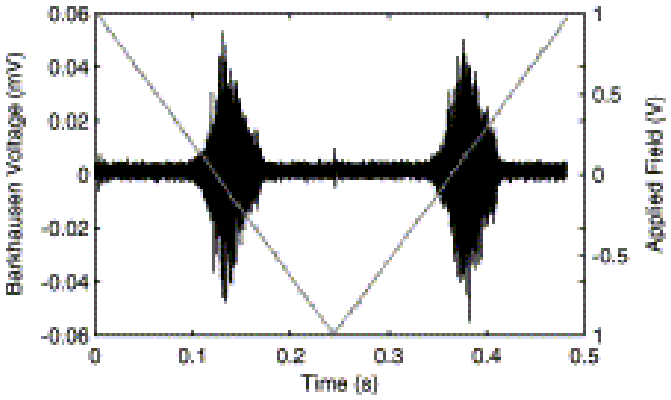

Figure 2-10 Barkhausen noise from other paper

The figure 2-11 shows the Barkhausen noise with different frequency of excitation signal. We can find that when the frequency of the excitation signal lower, there will be two peaks in half of one period. When the frequency of excitation signal little higher than 100Hz, the Barkhausen noise do not have much change compared with the 100Hz. But when excitation signal much higher than 100Hz, the Barkhausen noise will disappear.

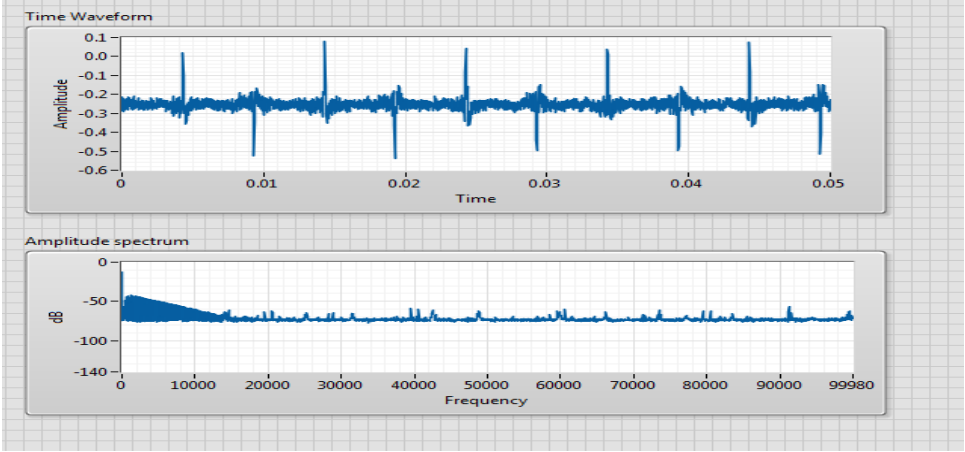

(a) Excitation signal (100Hz 1v)

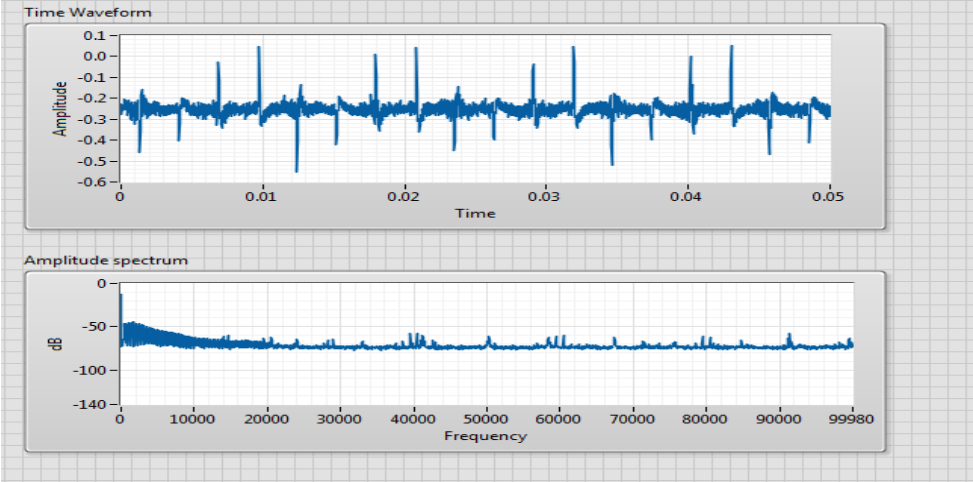

(b) Excitation signal (80Hz 1v)

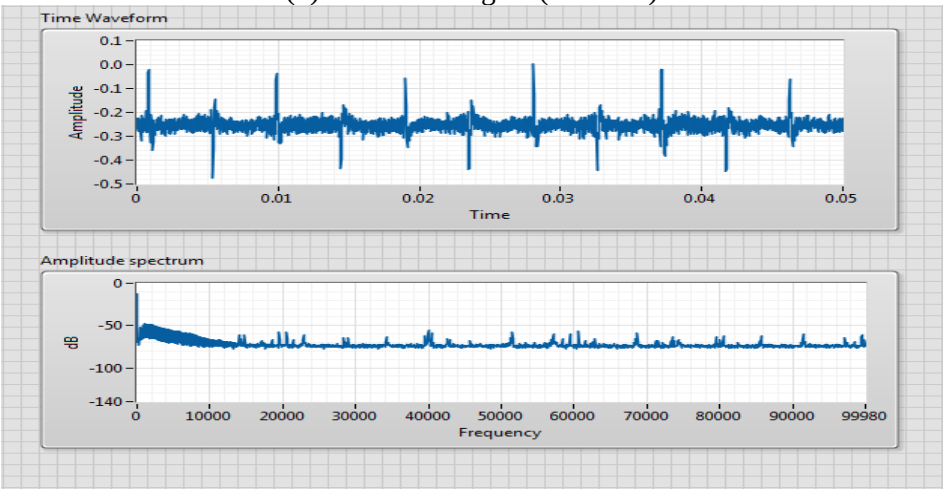

(c) Excitation signal (120Hz 1v)

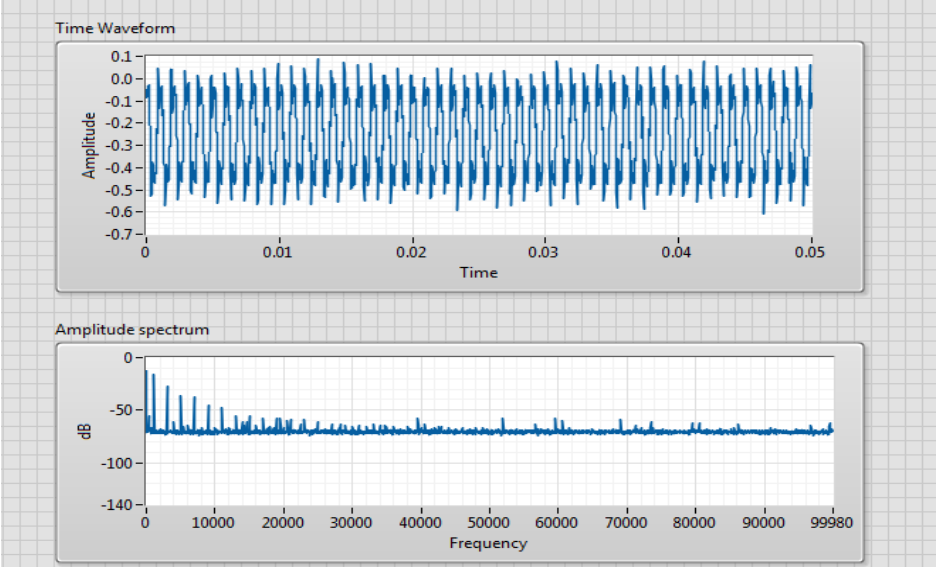

(d) Excitation signal (1KHz 1v)

Figure 2-11 Barkhausen noise with different frequency of excitation signal

2.2. Magnetic spins simulation

In a canonical ensemble, the average of the physical quantities can be expressed with Boltzmann distribution weight.

$$\text{avg} < \text{A(x)} >= \frac{\int e^{-H(x)/K_B T} A(x) dx}{\int e^{-H(x)/K_B T} dx} \qquad (1)$$

Where H(x) is Hamiltonian, the K_β is the Boltzmann constant and T is the Kelvin temperature. The x is the vector of the phase space which representing the degree of freedom of the system. The Ising model is one of the important theoretical models in statistical physics which can be used to describe the magnetic properties of anisotropic ferromagnetic materials. This method able to calculates the desired mean nature from the system's Hamiltonian. The Ising model use a finite lattice to simulate the state of the spin which represent the little magnetic moments. There are two possible state of the spin, +1 or -1, which represent the direction of the spin. It is very hard to compute all the state of the system; therefore, Monte Carlo method is employed to calculate the approximate solution.

$$\overline{A(s)} = \frac{\sum_{i=1}^{N} \text{A}(s_i) e^{-H(s_i)/k_B T}}{\sum_{i=1}^{N} e^{-H(s_i)/k_B T}} \qquad (2)$$

The eq. (2) is a simple sampling method in the Monte Carlo method which carried out with an average distribution, and each sample is completely independent. In order to improve the calculating efficiency, importance sampling is applied. Instead of sampling the phase space uniformly, the phase space point S_i is selected by the probability $P(\text{X}_i)$. The average state of the system is estimated based on these state samples according to the known probability distribution. Therefore, we get:

$$\overline{A(s)} = \frac{\sum_{i=1}^{N} \text{A}(s_i) e^{-H(s_i)/k_B T}/P(s_i)}{\sum_{i=1}^{N} e^{-H(s_i)/k_B T}/P(s_i)} \qquad (3)$$

Where $P(\text{X}_i)$ should satisfy：

$$P(\text{X}_i) \propto e^{-\frac{H(s_i)}{k_B T}} \qquad (4)$$

Then, eq.(3) can be express as a simple summation:

$$\overline{A(s)} \approx \frac{1}{N} \sum_{i=1}^{N} \text{A}(s_i) \qquad (5)$$

In order to simulate the interacting magnetic spins with a changing external magnetic field, a simplified two dimensional Ising model is approximated by Monte Carlo method. A lattice system contains 4 by 4 Ising spins with periodic boundary conditions is shown below.

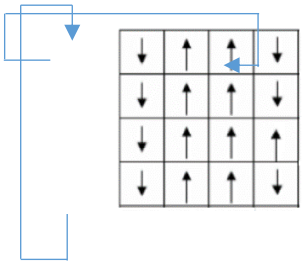

Figure 2-12 Schematic representation of the 4 by 4 Ising spin lattice with periodic boundary conditions.

The simplify Ising model is given by the Hamiltonian

$$H = -J \sum_{<i,j>}^{N} s_i s_j + B \sum_{n=1}^{N} s_n \qquad (6)$$

Consider a L by L Ising spin lattice system, N is the total number of the spins which equal to L *L. J is the interspin interaction, s is the spin state with value <1 or -1>, B is the external magnetic field. <i,j> are the nearest neighbor spins. One state of the system can be described as

$$\overrightarrow{S_k} = (S_{k,1}, S_{k,2}, \ldots\ldots, S_{k,i}, \ldots\ldots S_{k,N}) \qquad (7)$$

Where k is the k[th] step within the Monte Carlo step. First, an initial state $\overrightarrow{S_0}$ is random generated. Then, let $\vec{S}_{k+1}^{(0)}$ equal $\overrightarrow{S_k}$.

$$\vec{S}_{k+1}^{(0)} = \left(S_{k+1,1}^{(0)}, S_{k+1,2}^{(0)}, \ldots.\ , \mathrm{S}_{k+1,i}^{(0)}, \ldots..\mathrm{S}_{k+1,N}^{(0)}\right) = \overrightarrow{S_k} \qquad (8)$$

A temporary state $\vec{S}_{k,\mathrm{i}}^{*}$ is used to determine whether the spin would flip. Assume the spin 1 is flipped.

$$\vec{S}_1^{1*} = \left(-S_{1,1}^{(0)}, \mathrm{S}_{1,2}^{(0)}, \ldots.\ , \mathrm{S}_{1,i}^{(0)}, \ldots..\mathrm{S}_{1,N}^{(0)}\right) \qquad (9)$$

If $\Delta\mathrm{H} \leq 0$ then $\mathrm{S}_{1,1}^{(1)} = S_{1,1}^{*}$. If not, a random number ξ is generated to compared with $\exp(-\Delta\mathrm{H}/K_\beta T)$. If $\xi \leq \exp(-\Delta\mathrm{H}_N/kT)$, $S_{1,1}^{(1)} = \mathrm{S}_{1,1}^{*}$. Otherwise, $S_{1,1}^{(1)} = \mathrm{S}_{1,1}^{(0)}$. In other word, the probability of the spin flipped is:

$$P(S \to S^*) = \begin{cases} e^{(-\Delta\mathrm{H}/kT)}, & \Delta\mathrm{H} > 0 \\ 1, & \Delta\mathrm{H} < 0 \end{cases} \qquad (10)$$

Then, $\overrightarrow{S_{k+1}}$ can be find by calculate all the $S_{k,i}^{(i)}$.

$$\Delta H\left(S_{k+1,i}^{*}, \mathrm{S}_{k+1}^{(i-1)}\right) = H\left(\mathrm{S}_{k+1}^{1*}\right) - H\left(\mathrm{S}_{k+1}^{(i-1)}\right) \qquad (11)$$

One Monte Carlo step is completed when all N spins have been calculated. The averaging magnetization is then calculated as

$$\overline{\mathrm{M}} = \frac{1}{N}\sum_{i=1}^{N} S_i$$

A MATLAB code which implements above algorithm is developed. Some of the simulation results are shown below. The N = 400*400. The period of the alternating magnetic field is set as 10000 MCS. After the generating the initial states, first running 5 periods to reduce the effect of the initial random states.

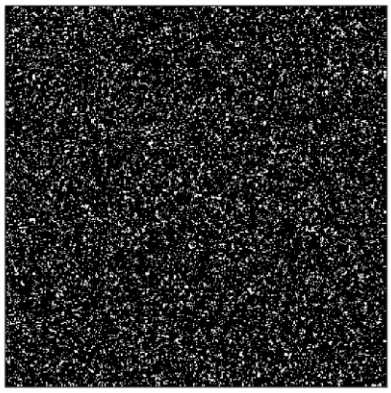

Figure 2-13 Spin array domain configuration

The spin array domain configuration has been shown above. The states of the spin have been to black and white in the lattice system. Each block corresponding to the twofold state of the spin in the system.

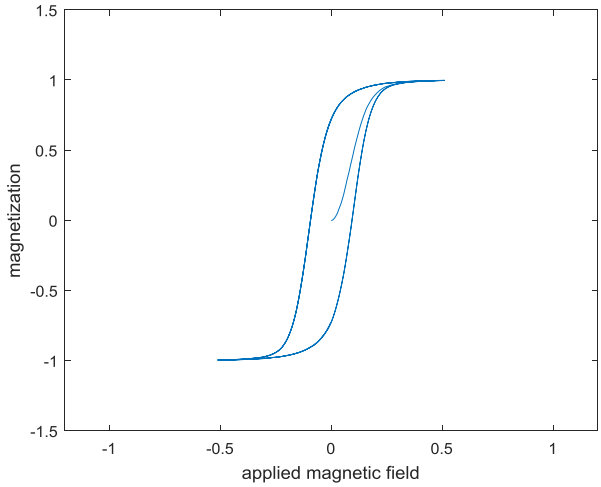

Figure 2-14 Mean magnetization, M, versus external field when J = 0.7

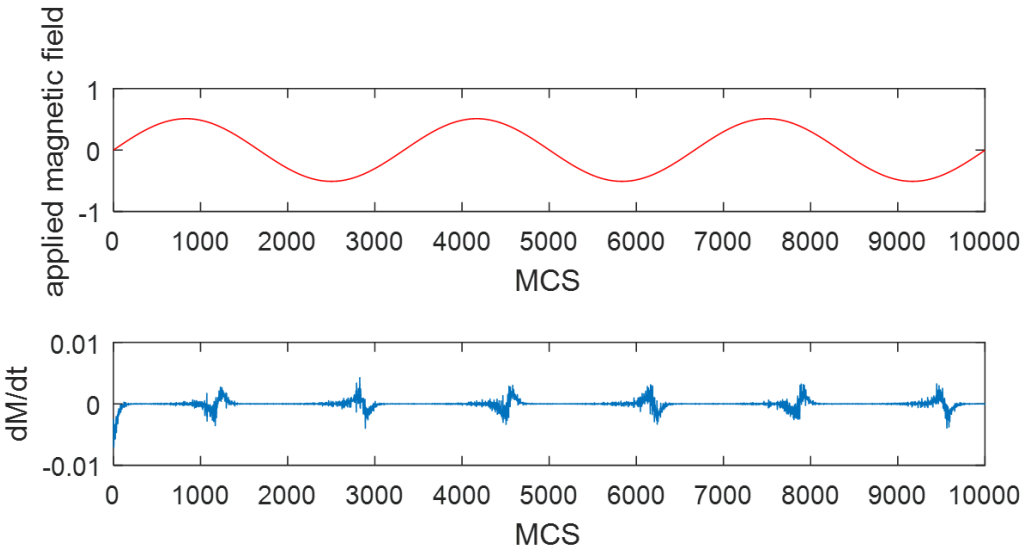

Figure 2-15 applied magnetic field and simulated BN

The figure 2-15 above shows a simulation result for the differentiation of the magnetization under applied magnetic field. The magnetization experienced discrete changes with respect to time is considered as the MBN. The profile of the simulated MBN is shown below.

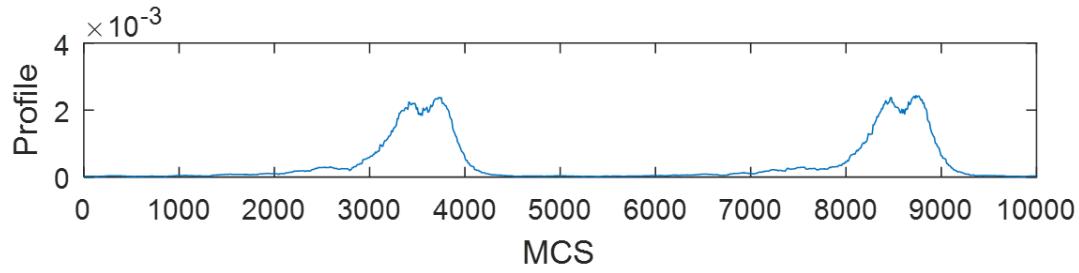

Figure 2-16 root mean square of simulated MBN

MBN shows good promise in mechanical properties evaluation include stress. In order to study the effect of the strain on the magnetic domain in the simulation, the interspin interaction *J* is assigned with different values. As strain increases, the *J* becomes smaller. Consider when the strain is applied to the material, J is reduced since the magnetic domains are more separated. The result is from the simulation of 400 by 400 spins. One period is simulated by 10000 MCS and the applied with sinusoid external magnetic field. The simulated MBN results have been shown below.

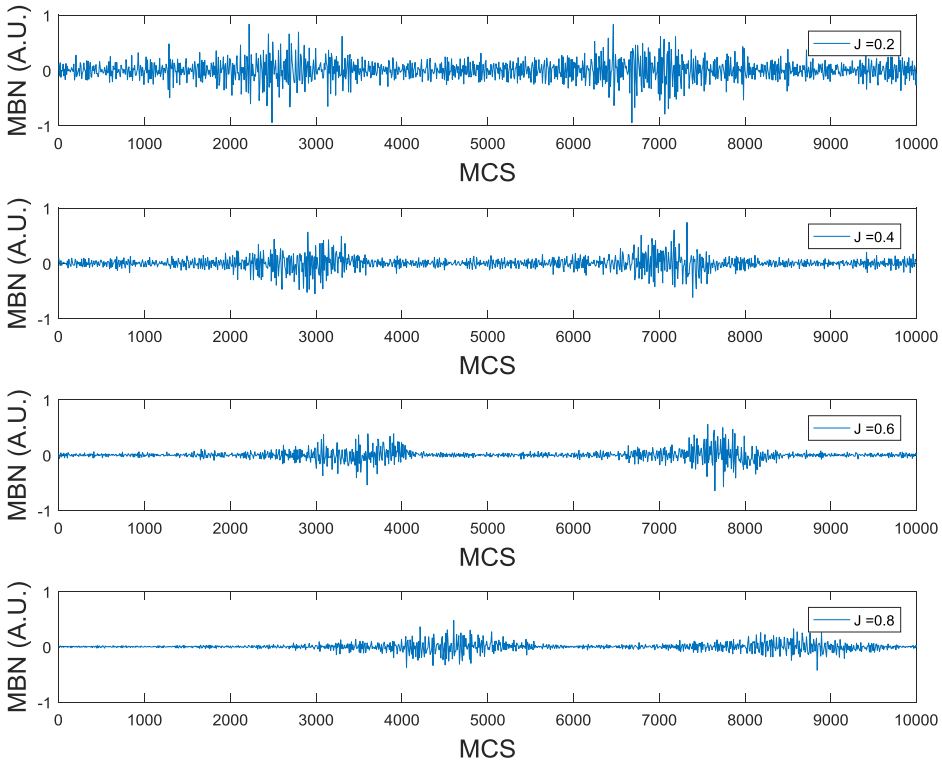

Figure 2-17 Simulated MBN with different interspin interaction assigned

The results shown in the fig.2-17 are the averaging from 5 periods. From the results, we can see the trend obviously that MBN amplitude decrease as *J* increases. In order to compare and correlate the MBN and J, a plot showing root mean square (RMS) against J is displayed in following figures. The root mean square voltage is an informative parameter of MBN which represent the power of the MBN signal.

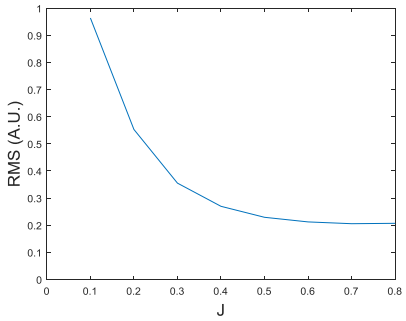

Figure 2-18 RMS of the simulated MBN with different inter-spin interaction assigned

The result shows reasonable trend, RMS decreases as J increases. The experiment will be done in the future to have a better understand of relationship and improve the simulation.

Pinning such as dislocations, disorders, voids on the domain walls will affect the magnetic properties of the materials. The simulations with and without void have been studied. By assigning zero spins, we create two void areas in the simulation. The result is from the simulation of 400 by 400 spins applied with sinusoid external magnetic field. The simulated MBN results have been shown below.

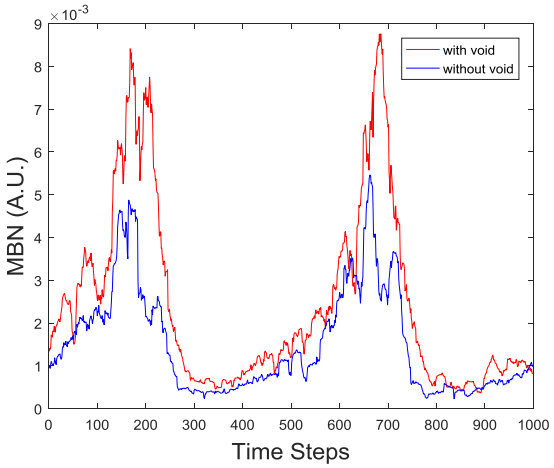

Figure 2-19 Simulated MBN profile with and without voids

The results shown in the fig.2-19 are the averaging from 10 periods. As shown in the figure, the pinning introduced in the simulation result in higher value of the profile.

In order to have a better understand on the simulation results, optimization method NSGA has been employed. NSGA is a non-dominated sorting-based multi-objective evolutionary algorithms to find the optimal solution. The rule of NSGA is shown in the following figures.

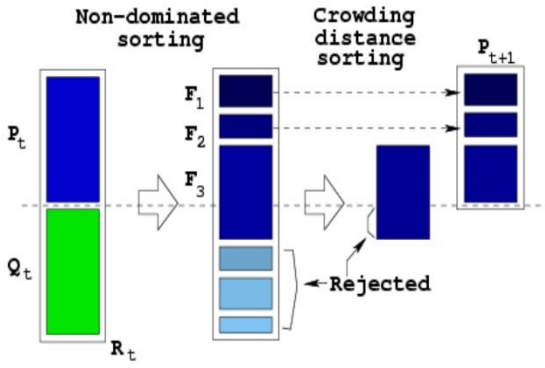

Figure 2-20 NSGAII algorithm

P_t/Q_t are the parents/offspring of generation *t*. All elements in P_t and Q_t compete with each other for non-domination. Optimal-front is the set includes all the non-dominated elements. The elements in the optimal-front F_1 (if $||F_1|| \leq ||P_{t+1}||$) are selected into the next generation. This procedure repeats until ||F1|| + ||F2|| + … + ||Fk|| ≥ ||Pt+1||. If ||F1|| + ||F2|| + … + ||Fk|| > ||Pt+1||, extra elements are rejected based on the crowding distance sorting.

To study the relationship between the peak value of the simulated MBN and the maximum energy change during the simulation, following optimization has been solved by NSGA:

- **Maximize:** $f_1 = Max(envelope(\frac{d^2M}{dt^2}))$
  $f_2 = Max(\frac{dE}{dt})$
- **Subject to** **J :[0 1.5];**
  h :[0 0.8];
- **No constraint**

The optimization is solved with 100 generations and each generation has 60 population. The probability of crossover of real variable is 0.9 and the probability of mutation of real variable is 0.5. The code is working to find the minimize, therefore, we are solving the minimize of the **-f_1 and -f_2.** The result is shown below:

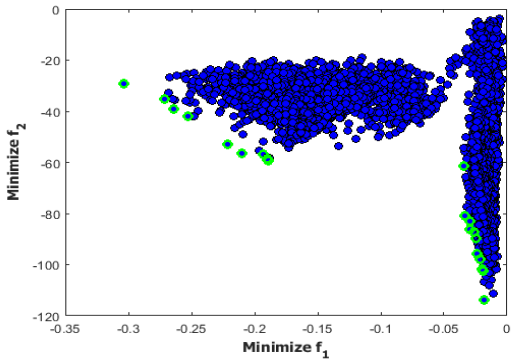

Figure 2-21 All the population of 100 generations

To reduce the calculation time, the number of the spin is selected as 10 by 10. As shown in the figure, the points are clearly divided to two parts. The points in the left part have better value of f_1 and the points in the right part have better value of f_2. The green circled points are the Pareto front. From the plot, we can see the relationship between the peak value of MBN and the energy change in the simulation.

2.3. Experiment setting and optimization

As the flowchart shown in the figure 2-22, the coil wind around U-shape core will be used to excite low-frequency alternating magnetic field and the pick-up coil putted in the center of two poles of core will be used to capture Barkhausen noise emitted by the pipe sample due to the discontinues movement of the domain wall. The signal picked up by the coil sensor will pass through a high-pass filter to filter out the

low frequency excitation signal and an amplifier circuit to amplify the weak Barkhausen noise signal to millivolt level.

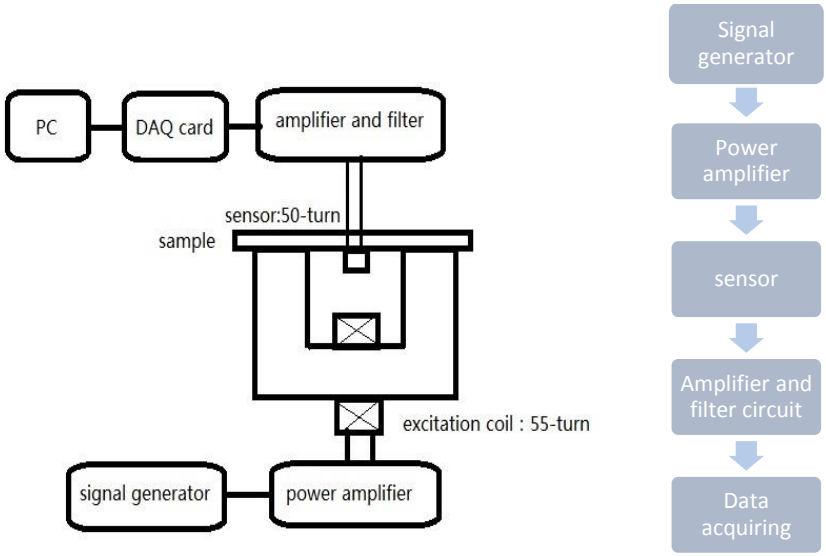

Figure 2-22 Flowchat of the experiment setting

Mainly focusing on the study of the characters of pipeline, we are using the following two pipeline as our sample. And the corresponding information about the size of the pipelines have been shown in the figure 3.

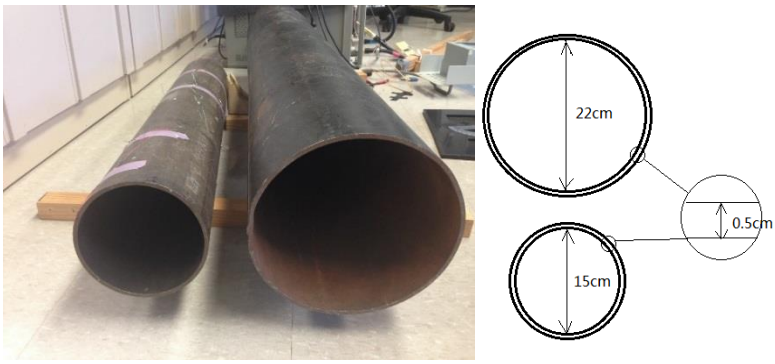

Figure 2-23 Pipeline sample and size information

The signal in figure 2-24 shows a smooth profile and nice shape after some adjustments in the position of the sensor and making the sensor core stick closely to the sample.

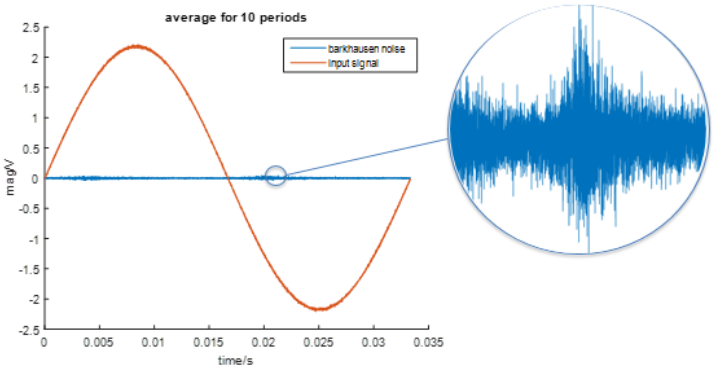

Fig. 5 new barkhausen noise measured

2.3.1. MBN profile extraction

We are using the root mean square(RMS) to get the profile of the Barkhausen noise. It is mainly because that Barkhausen noise like signal, signal can fluctuate violently in local regain. By using RMS, we can extract more smooth profile and provide more global information. The figure 6 show below are the Barkhausen noise of pipeline with different diameters and their profile. The graph only half period of the signal for the reason that the Barkhausen signal is symmetric during one period. One peak is easy for the parameter extraction in the following part.

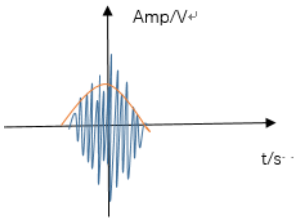

one peak of signal is

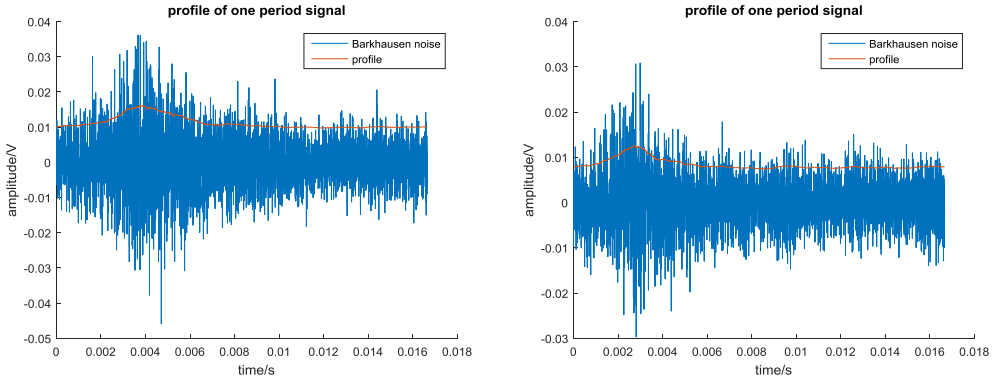

(a) (b)

Figure 2-24 The profile of pipeline with small diameter(a) and with large diameter(b)(30hz)

To further get the parameters related to the profile which are peak value, peak position and peak width, we need to use find function in the MATLAB to check the maximum and minimum points and mark their values and position on the graph. For the half width value, we still cannot find an efficient way to get it directly, but we can get the number on graph by hand. And to make the profile looks more smooth, we use polynomial to fit the profile we get before.

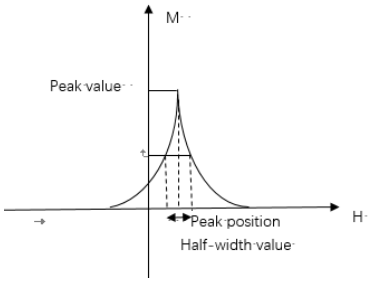

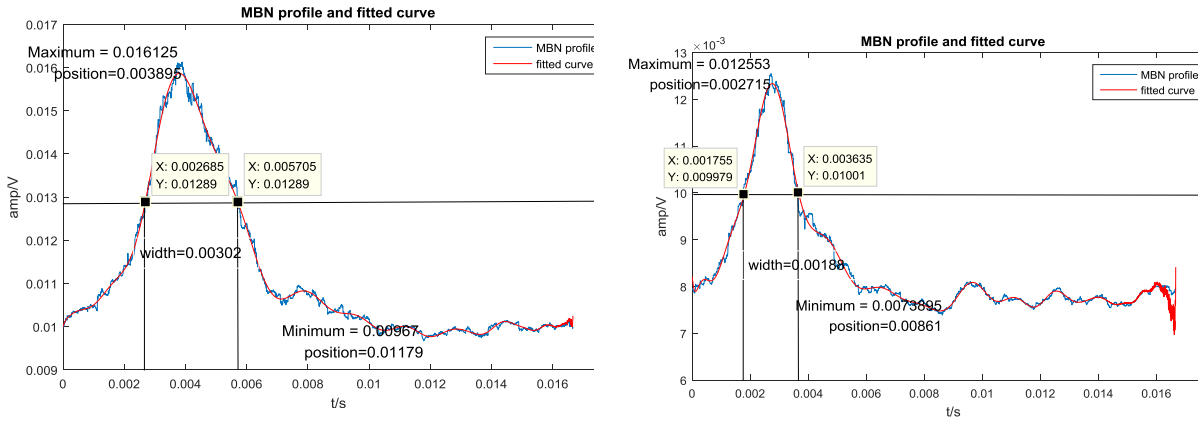

(a) (b)

Figure 2-25 Parameters of Barkhausen noise profile

2.3.2. Applied excitation field study

Several studies in the literature show the use of different magnetic excitation frequencies, typically ranging from 0.05 to 125 Hz for the measurement of the MBN. Different frequency will have various effect on the Barkhausen noise we measured. A proper frequency will decrease the measure noise and increase the sensitivity of the measurement so that we can get more accuracy information from the signal we get.

To compare the profile of the Barkhausen noise with different excitation in one graph, we should make some adjustments of the way we draw the graph. In the previous work, we draw the profile of Barkhausen noise versus time. It is not proper when the excitation frequency is a variable. So we choose the applied voltage as the x-axis which has the following relationship with the time as shown in the figure 8. And when we just change the frequency, the maximum and minimum of the applied voltage will be the same, so that we can draw MBN profile versus applied voltage in the same scale.

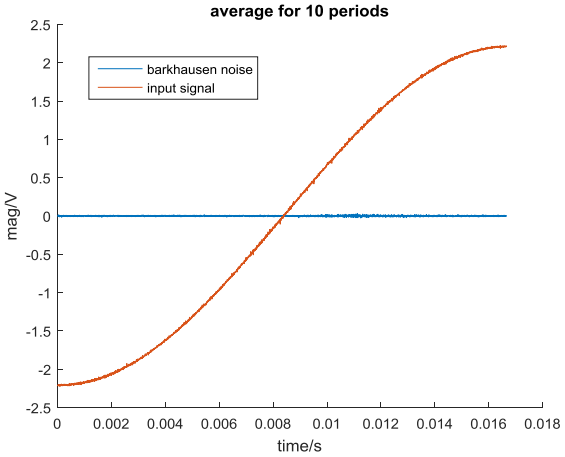

Figure 2-26 applied voltage change with time

The relationship between the profile of Barkhausen noise with their excitation frequency in different samples are shown in the figure 9 below. The trend in the graph is consistent with the paper of V. Moorthy and further proves the validity of our result.

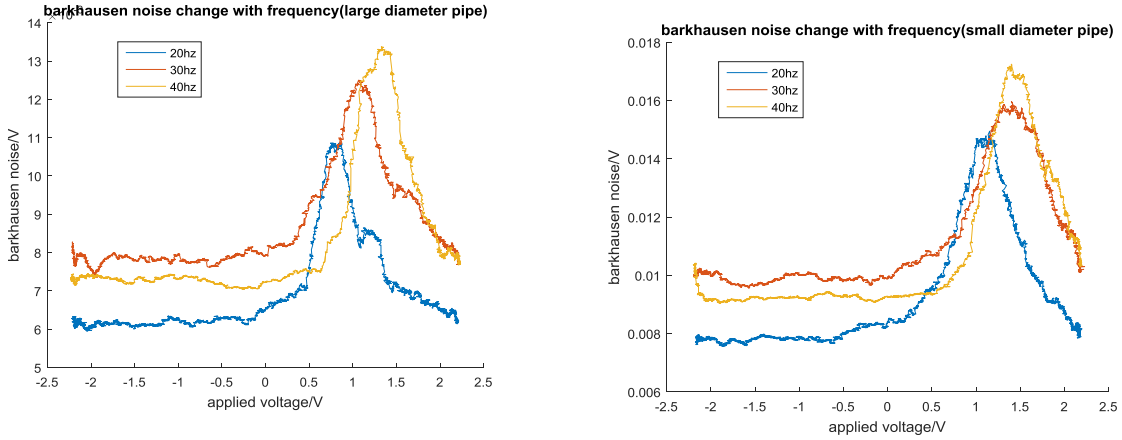

Figure 2-27 Barkhausen noise change with frequency

We can get the following rule: The increasing frequency will increase the number of domain wall and increase the intensity of the Barkhausen noise. From the graph, we can find that the peak value of MBN profile increase from 20Hz to 40Hz in both large diameter pipeline and small diameter pipeline. At high frequency, the surface tends to undergo demagnetization faster than the subsurface of ferromagnetic test material because of the eddy current damping and reduction in magnetization range. From the graph, we can find that the second peak of the large diameter pipeline which is considered as the response of the hard region near the surface of sample disappear as the increase of the frequency. The graph shows behind also reveal some differences in the structure of two kind of pipeline.

The applied voltage will also have influence on the strength of the magnetic field and further affect the saturation depth of the field into the samples. The voltage value shows on the graph is the V-peak of the applied voltage.

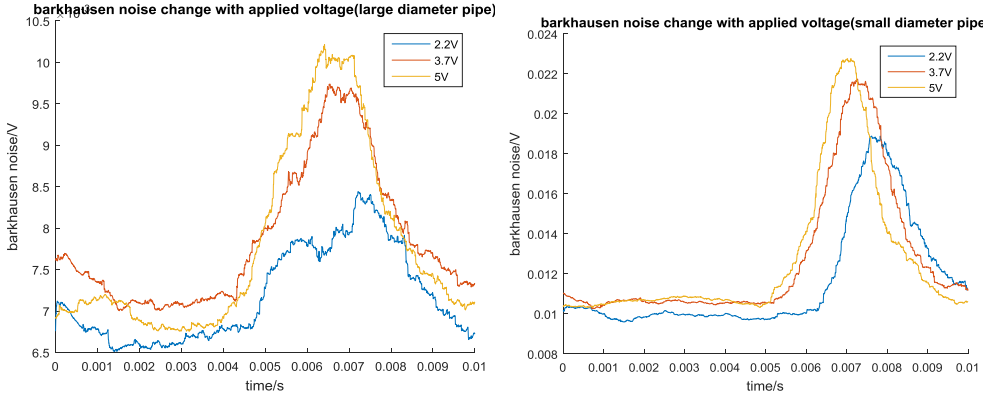

Figure 2-28 Barkhausen noise change with applied voltage

The following rule can be gotten from the observation:

a) When the applied voltage decrease, the peak value of the barkhausen noise will decrease and the peak position will move to higher voltage.

b) The small diameter pipeline have the relatively active movement of the domain wall than the large diameter pipeline for the reason than the peak value of the small diameter pipeline is always larger than large diameter ones in the same experiment setting which shows some difference between two materials.

2.3.3. Magnetic field measurement

To get the corresponding relationship between the realistic magnetic field the sample experienced

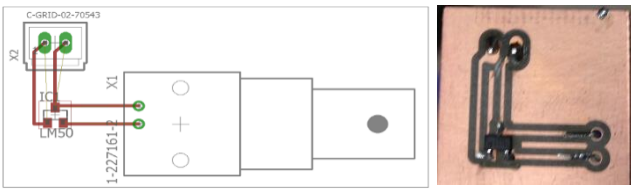

and the timing when Magnetic Barkhausen Noise generated, we introduce one hall sensor which can measure the magnetic flux directly. To hold the small sensor, we design a simple PCB and connect the components to the circuit (figure 7). The chip with three pins is our linear hall-effective sensor SS39ET from Honeywell. With supplied voltage amplitude 5 V, the relationship of the output voltage and magnetic flux with the units gauss has been shown in figure below. The sensor can measure a wide range of magnetic flux desity that between -1000 gauss to 1000 gauss and with a high sensitivity 1.4 mv/gauss.

Figure 2-29 design of the hall sensor circuit

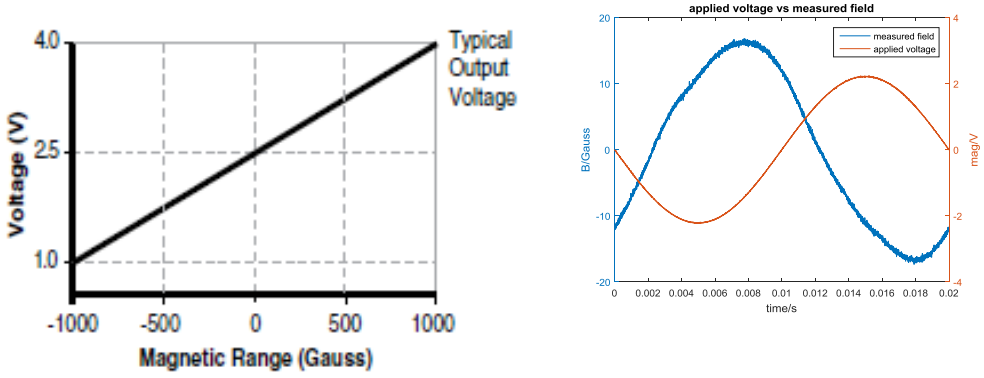

Figure 2-30 Transfer characteristics and the applied voltage vs. measured field by hall sensor

With the hall sensor, we can know the magnetic field between two poles directly. When we draw the magnetic field against time and applied voltage against time together (figure 3), we find that two signals are not in the same phase. There is a delay between the magnetic field measured between two poles and the voltage applied. And the measured field is not as smooth as the applied voltage signal. The figures above show draw applied voltage and the measured field with Barkhausen noise respectively. Barkhausen noise happens around the zero-crossing point of the measured field. This is consistent with our common sense that the maximal rate of change occurs at the zero-crossing point and the results from other papers.

Figure 2-31 applied field and measured field vs. Barkhausen noise

With the field measured by the hall sensor, we can have a consistent standard to draw the profile of

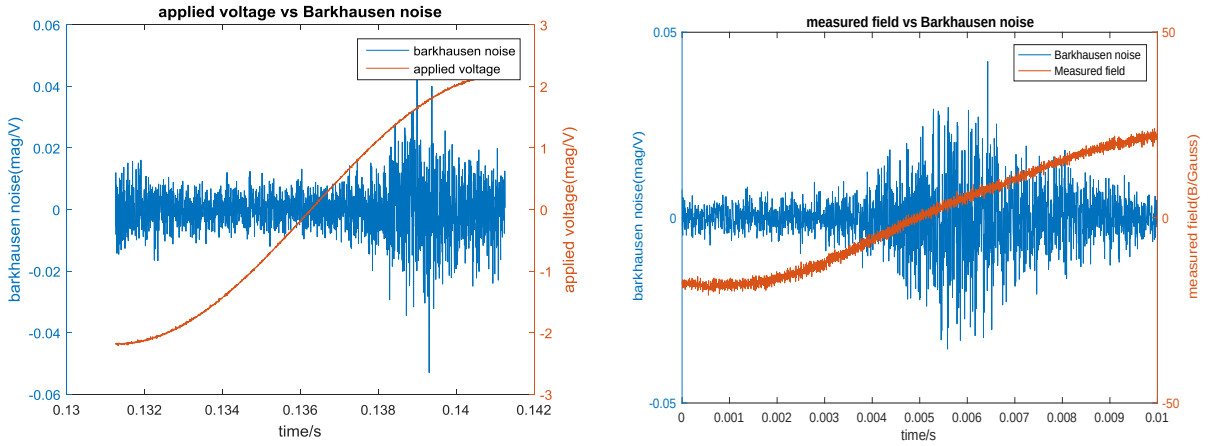

Barkhausen noise with different frequency of the input signal together. Whereas, because of the noisy signal from hall sensor, it is difficult to have a smooth profile of the Barkhausen noise. Even though we can see a rough shape of the profile and relative height between different profiles, highly noisy profile overwhelms a lot of important information. It is important to pre-processing the signal. By using moving average with window size 50 we can get a relative smooth sin signal and the signal processed matches with the original signal(fig 2-32).

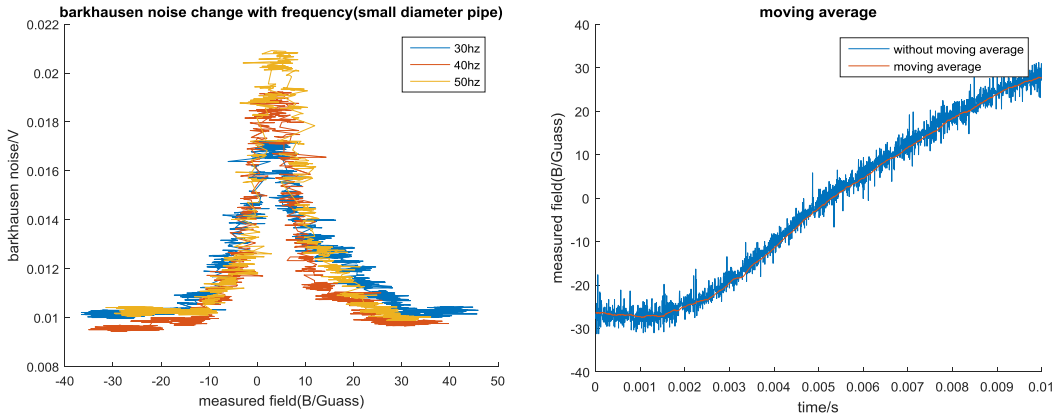

Figure 2-32 Barkhausen noise profile plot against measured field measured filed processed by moving average

With the processed signal, we can get smooth profiles. By comparing the barkhausen noise profile we get from moving average with the profile we get before. It is quite the same and preserves detail in the figure 2-33.

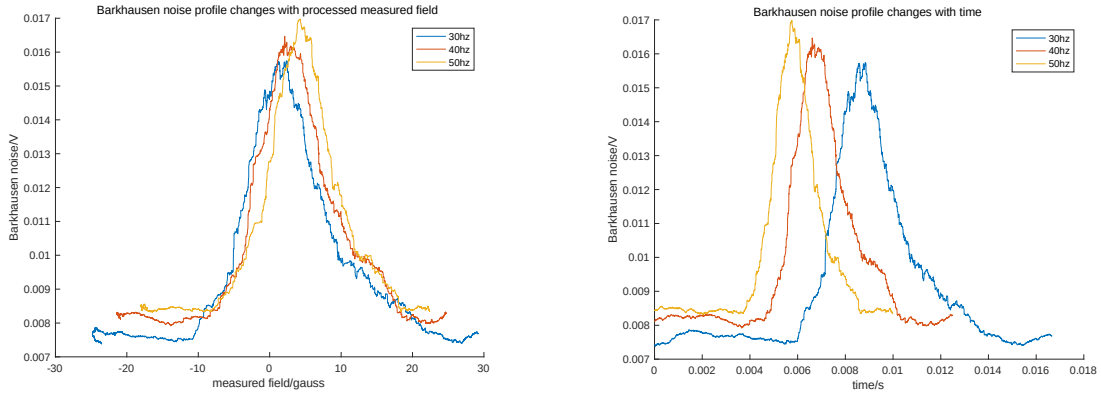

Figure 2-33 Barkhausen noise profile changes with processed measured field and Barkhausen noise profile changes with time

B (magnetic flux density) describes the field felt by objects and will change with different permeability. With the formula H=B / μ_0, we can calculate the magnetic strength which is the same when the hall sensor is close to the surface of the sample.

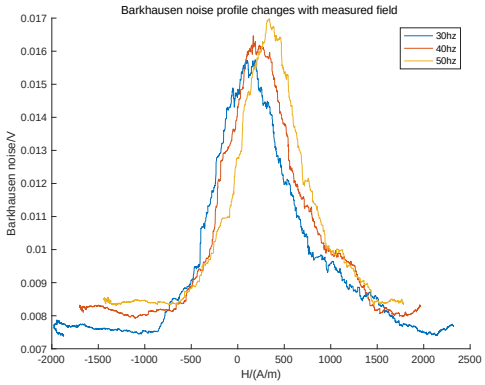

Figure 2-34 Barkhausen noise profile plot against magnetic strength

2.3.4. Depth information

According to the formula of electromagnetic skin depth δ

$$\delta = 1/\sqrt{\pi f \sigma \mu_0 \mu_r}$$

The Barkhausen noise transmitted from different region of material will have different frequency. The high frequency content of MBN is mainly attributed to the near-surface magnetization. Low frequency components will contain information from volumes of material at greater depth.

To filter out the Barkhausen noise in different frequency band, we use one butterworth bandpass filter with parameters maximum passband attenuation -3dB and minimum stopband attenuation -35dB. The sample rate for the experiment is 200000 point/s, the maximal frequency of the signal should less than half of the sampling frequency which is 1000000 Hz. We divide the bandwidth of Barkhausen noise into 5 or 10 parts equally. The stop edges for the bandpass filter are lower bandpass edge minus 500hz and higher bandpass edge plus 500hz.

Figure 2-35 frequency spectrum through bandpass filter(1-20khz) and MBN signal through bandpass filter(1-20khz)

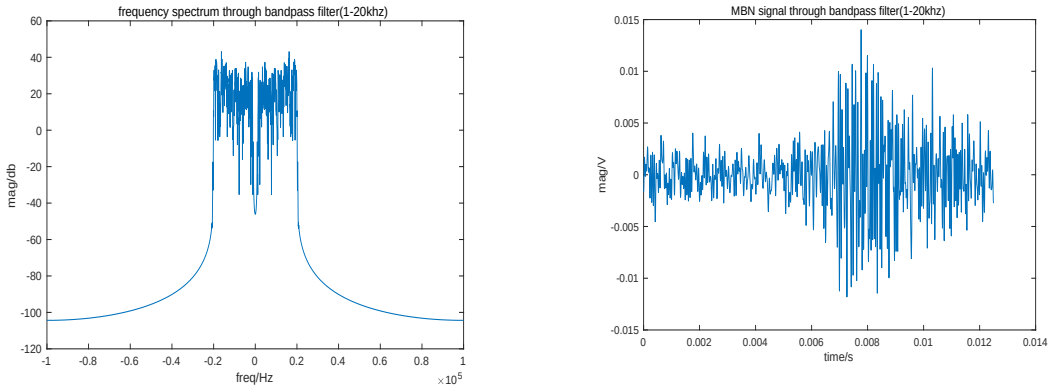

The figure 2-36 shows the profile of Barkhausen noise in different frequency range:

It is obvious that the second peak shows when the frequency range increase. According to the results in previous paper, the green line with higher frequency show profile of Barkhausen noise in near-surface region. It is consisted with the results in previous study.

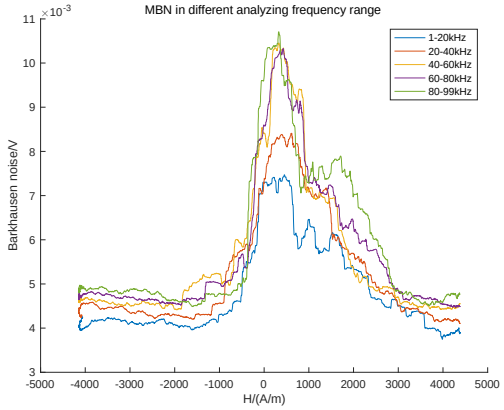

Figure 2-36 MBN in different analyzing frequency range

2.3.5. Extract parameters

With the profile we get from previous step, we can extract parameters such as first peak peak-value and second peak peak-value. By using the center frequency as the frequency to calculate the skin depth, we can get a table about the relationship between analyzing frequency band with the depth.

Table 1 Relationship between analyzing frequency band with depth

Analysing frequency/khz	Center frequency/khz	Depth/um	Analysing frequency/khz	Center Frequency/khz	Depth/um
1-10	**5**	283.6	**50-60**	**55**	85.51
10-20	**15**	163.7	**60-70**	**65**	78.65
20-30	**25**	126.8	**70-80**	**75**	73.22
30-40	**35**	107.2	**80-90**	**85**	68.78
40-50	**45**	94.53	**90-100**	**95**	65.06

The following figures show the variation trend of the peak value change along depth. Even with different excitation frequency, the shape could be different. For each curve in one figure, they all follow the same trend.

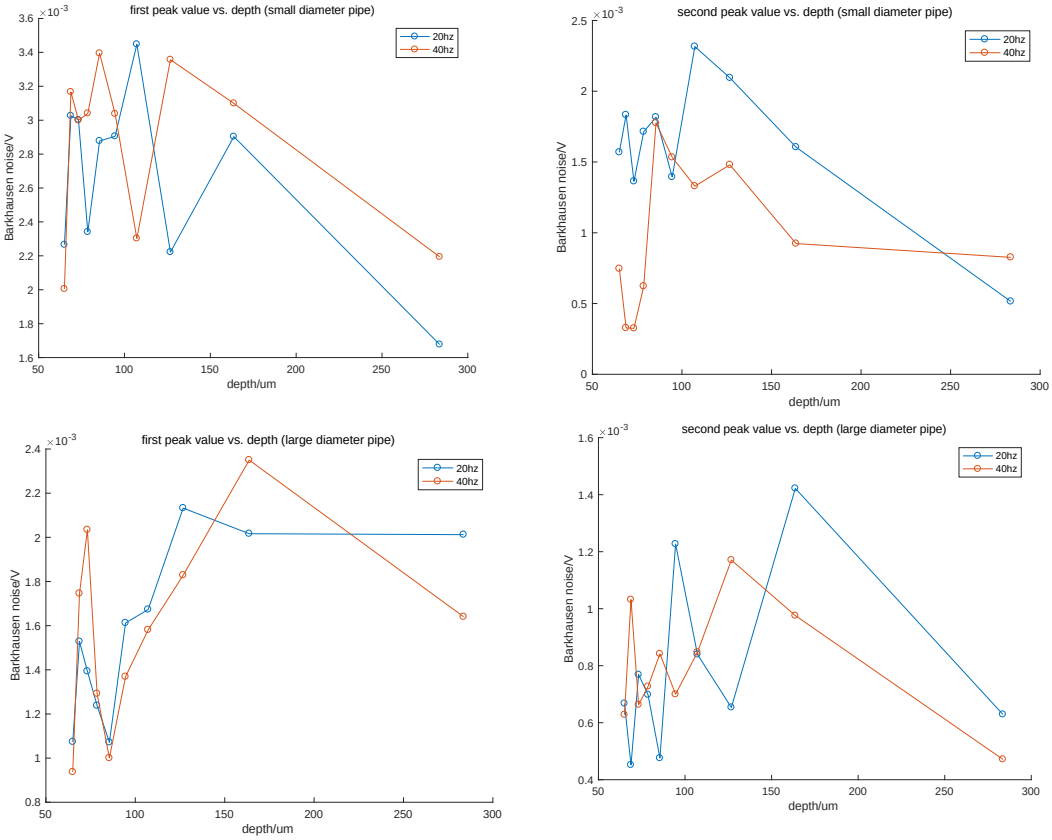

Figure 2-37 MBN signal peak vs. depth

2.4. Sensor optimization

Considering the sensitive, weak and noise-like properties of the Barkhausen Noise signal, a suitably efficient sensor is indispensable to achieve accurate measurement for the microstructure of material. One

of the most important part for the sensor design is the excitation part which is the core and excitation coil in our experiment. Previous work has investigated the relationship between the magnetic field with different single objectives like material of the core, the shape of core tips and distance between two poles. This kind of study can give us guidance when we are designing our experiment, but is still not enough when we have trade-off between two objectives. We introduce some advanced multi-objective algorithms such as NSGA Ⅱ and NSGA Ⅲ as efficient tools to investigate the relationship between magnetic field at the center of two poles with different shape of core. To get a better spatial resolution, the minimal size of the core should also be satisfied. What is more, the sensor mainly be used to detect the aging of steel pipelines in industry whose diameters might vary from 150mm to 500mm. The cylinder like sample (pipeline) make it difficult to couple with the flat pole of core (there is gap between poles and samples) and it is a big challenge to design a sensor which is good for all different samples (gaps might vary with the diameter of sample pipeline) (figure 2-38).

Figure 2-38 Ansys model and gaps between sample and core

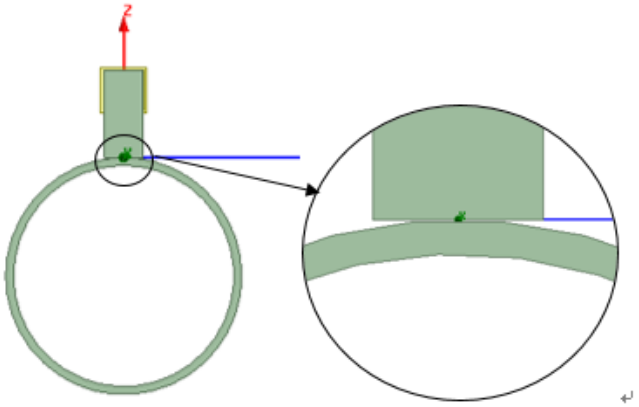

Acording to the previous discussion, two objectives which are important for the design of the sensor for a spacial sample. One is that we try to maximize the magnetic field at the center of two poles which is the position for the pick up coil to gain a relative strange signal. The second one is to minimize the overall effective area of the magnetic core to obtain a good spatial resolution (to get the information at small local area which is good for crack detection). What is more, I try to take the sample shape into consideration. To design a sensor which is good for both the worse situation, the pipeline sample with diameter 150mm (large gap between poles and sample), and the best situation, the flat sample (no gap).

For the variables, we choose the following defined a,b,c as our variables to control the shape of the core:

Figure 2-39 Definition for variables and objectives

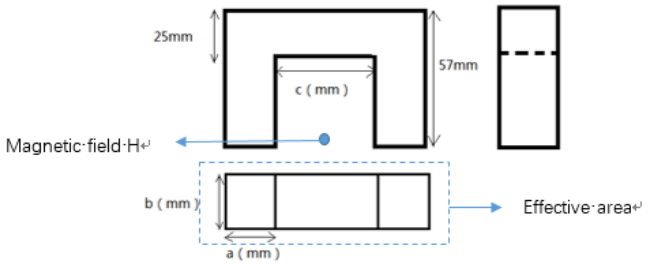

To calculate the magnetic field at the center of two poles, I build the 3D model in the AnsysEM software. To cut down the simulation time it takes, the original model has been replaced by half and using one symmetric boundary to gain the same result. But it still takes almost one minute for each population.

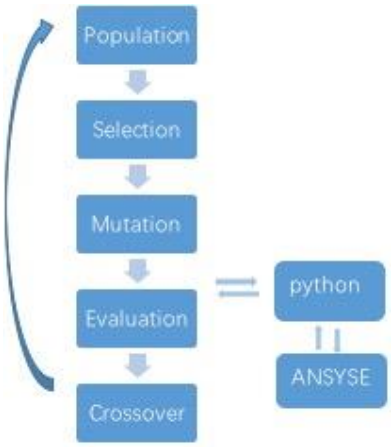

…One python code as an interface between MATLAB code and simulation software ANSYSEM can call ANSYSEM project and feed the population points into the variables to change the shape. of the core in model. And then the magnetic field value can be get from one txt file saved after simulation procedure.

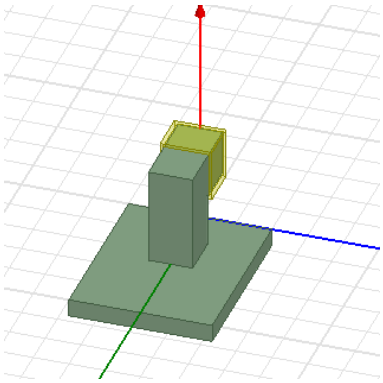

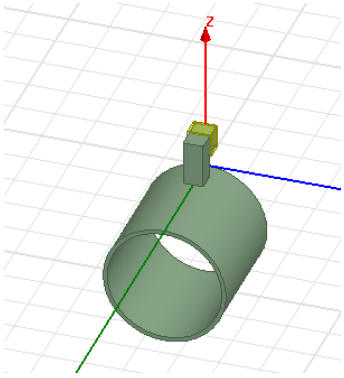

The following figure 2-41 shows the pareto fronts (any point in pareto front is not inferior than any other points in objective space) we get:

Figure 2-40 Ansys model with flat sample and pipeline sample

Figure 2-41 Pareto front get from NSGAⅢ

By using the L2 norm decision making method with idea point as reference point and with different weight . We can finally find one point:

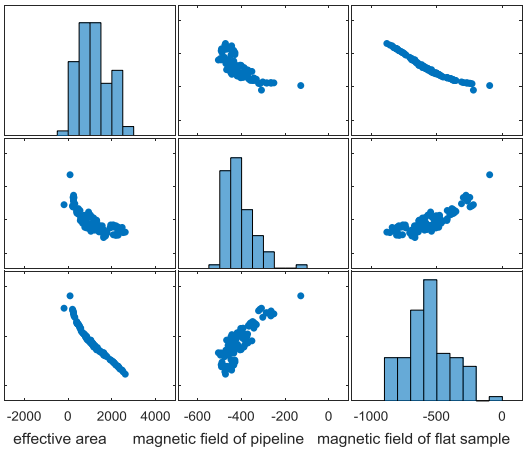

Table 2 Decision making with L2 norm with different weight

Wight	Effective area	Magnetic field of pipeline	Magnetic field of flat sample	a	b	c
(1,1,1)	876.60	-383.61	-537.21	14.10	17.6	21.49
(1,2,2)	1634.14	-461.04	-691.05	21.89	20.04	37.74
(1,3,3)	2377.17	-465.59	-831.19	22.65	23.48	55.91

By slightly change the weight, we can get different combination of objectives. From the table show above, we can see the solution with weight (1,2,2) is preferred which has a reasonable size of the core and relatively bigger magnetic field for both samples.

2.5. MBN grain size and carbon contents measurment

2.5.1. Material preparation

The experiments are performed on various types of mild steels obtained commercially, include 1008, ASTM 36, 1018 and 1026, with different shapes. Steel 1008, ASTM 36 and 1018 are plates with the same thickness of 0.1875 inches. Steel 1026 is the pipeline with outside diameter of 6 inches and a wall thickness of 0.188 inches.

To observe the microstructure on the surface of each sample, small pieces of the samples were cut and polished using silicon dioxide paste（0.5 μm）.The metallographic structure could be revealed by etching with the 4% Nital solution. Dark and bright regions represent the pearlite and the ferrite, respectively. The proportion of the dark region increases with the increase of the carbon content and has great influence on the MBN signal. Fig. 1 shows the microstructure observed under an optical microscope with the magnification of 2000X. The details of the chemical composition and microstructure are summarized in Table 3.

Table 3 Carbon content and grain size of steel samples

Samples	**Carbon Content (CC w%)**	**Grain Size(GS) (d/ μm)**
1008	0.04	39
A36	0.12	11
1018	0.19	10
1026	0.25	15

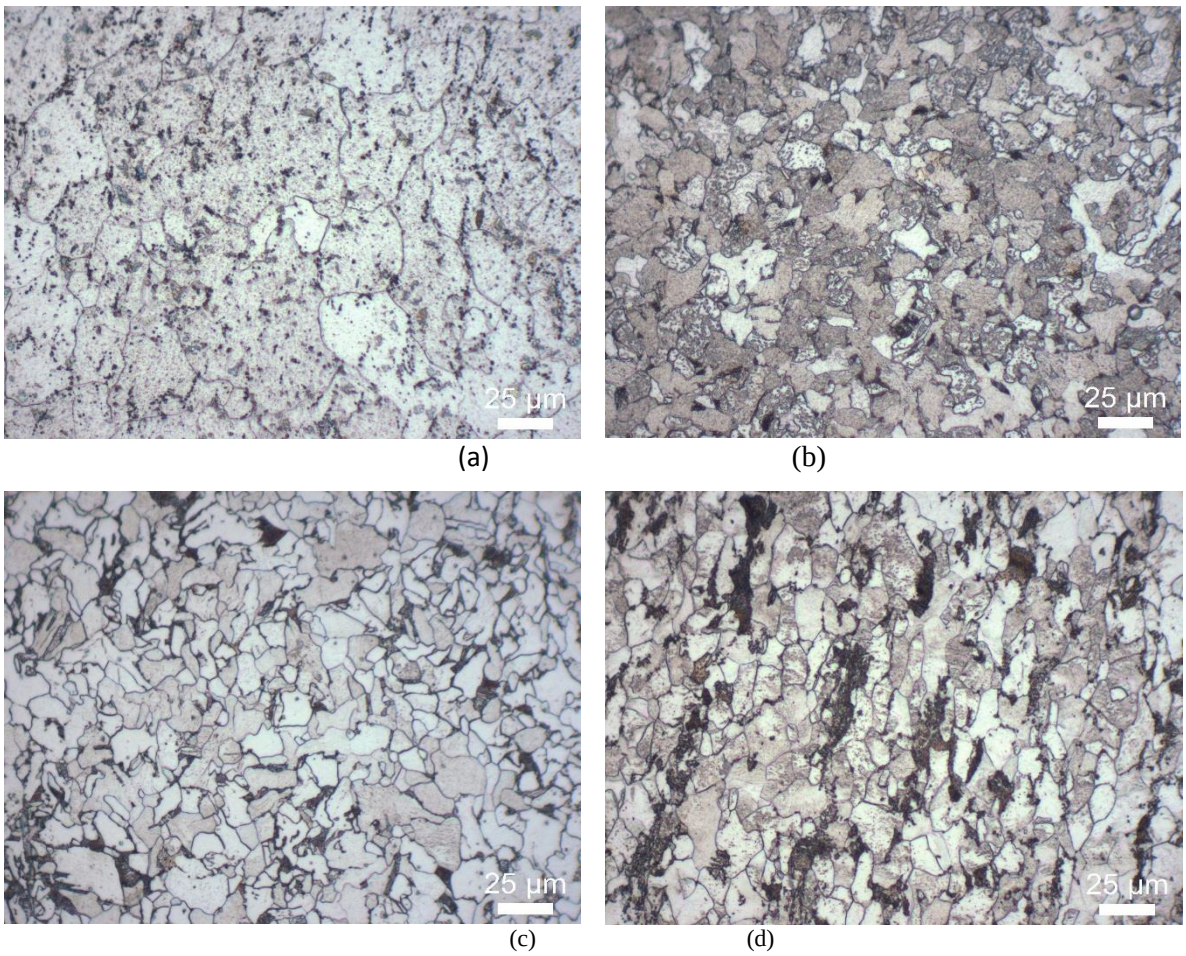

Figure 2-42 Optical micrograph of (a) 1008 (b) ASTM 36 (c) 1018 (d) 1026 samples

2.5.2. Simulation setup

In order to have a better understanding of the carbon contents' effect on MBN. A simplified three-dimensional Ising model which simulates the interacting magnetic spins with a changing external magnetic field is studied. To simulate Barkhausen noise with different carbon content, 3-D simulations have been performed on the spin lattice systems. Since more carbon content will result in a higher local coercive field [11], the spins within the region of interest are harder to change the status. The 'pinning' area is random selected and spins within the region are assigning with zero value. Since the relative atomic mass of iron is more than 4 times of carbon and each spin will affect 6 nearest neighbors, 1%, 3% 5%, 6% of 'pinning' are simulated for carbon content 0.04 wt%, 0.12 wt%, 0.19 wt%, 0.25 wt%. As shown in Fig. 2, an external field changes as a triangle wave with $\Delta B = 0.002$ and 100 Monte Carlo Steps(MCS) per field step. To reduce the uncertainty, the simulation results are taking the average of 10 periods of simulated MBN signal.

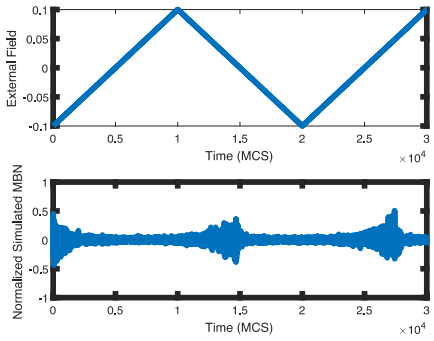

Figure 2-43 Simulated MBN with the external field

2.5.3. Experimental sensor

Based on the original experiment setup, to keep the relative position of excitation core and pick-up coil consistently, we design a holder to integrate the excitation part and pick up part with 3D printer. Fig. 2-44 shows the schematic and physical prototype for the holder.

(a) (b)

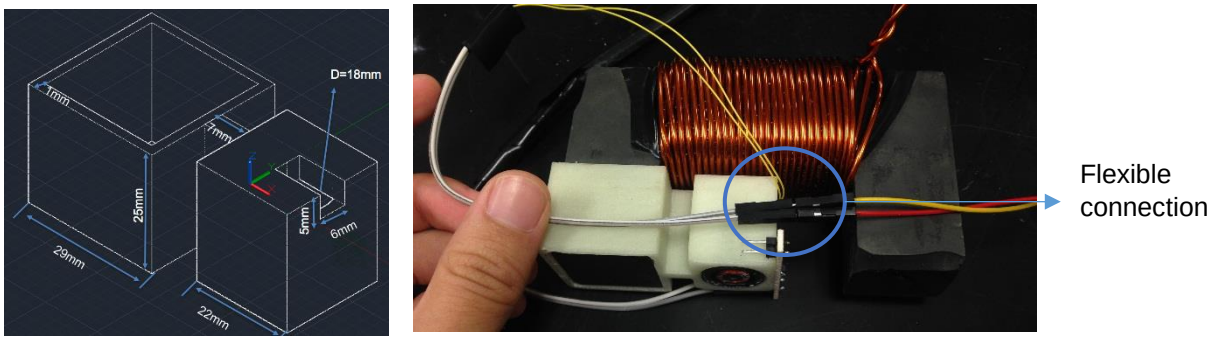

Figure 2-44 The schematic and physical prototype for the holder

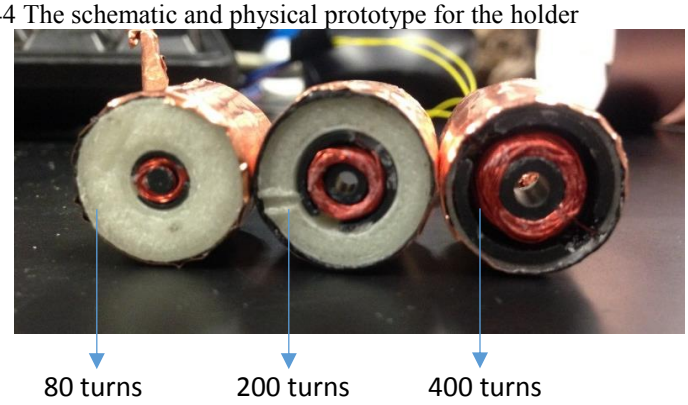

Figure 2-45 Pickup coils with different turns

To investigate the influence of pickup sensor, pickup coils with different number of turns (Fig. 2-45) has been introduced in the experiment. From the Fig. 2-44(b), the sensor and other parts of the experiment are flexibly connected for easy replacement.

MBN signals repeat every half period. To remove the white noise in the signal, an average of ten half-periods of MBN signals have been taken as the signal to be processed. The profile of the MBN signal is extracted as a plot of average RMS (root-mean-square) (calculated with the adjustable window size of 1/40 of the points per period) as a function of the magnetic field measured by hall sensor. In consideration of the random property of MBN, to get relative robust and reliable parameters, ten sets parameters obtained from a single measurement averaged and summarized as the parameters to be analyzed in the following steps. The frequency spectrum of the MBN signal has been determined from the Fast Fourier Transformation (FFT) of the time-domain signals using MATLAB. The profile of the intensity of the frequency response has been extracted by moving average with the window size of 1000.

2.5.4. Results and discussion

2.5.4.1. MBN signals for different of pick-up coils

To investigate the influence of the different number of turns of pick-up coils to the MBN signal, three different coils (80 turns, 200 turns, 400 turns) have been applied to measure the MBN emission with the same excitation signal. Fig. 2-46(left) shows the normalized MBN profiles, which have been divided by the peak values of the original profiles. There is no obvious shift in the peak positions of profiles for signal detected with different pick-up coils. All peaks overlap to each other. Whereas, with the increase of the number of turns, the signal-to-noise ratio (SNR) has improved dramatically. The noise can be defined as the area below the minimal value of the MBN profile.

Fig. 2-47(right) shows the normalized MBN frequency spectrum profile over bandwidth 0 to 100 kHz obtained from time-domain signals above. The frequency spectrum profile is used to show the intensity change along the bandwidth. Considering that the intensity changing with number of turns of pick-up coils, normalized profiles can put them into the same scale and make them comparable. For the same MBN signal, it is obvious that the sensor with the larger number of turns is more sensitive to the low frequency. The coil of 400 turns has higher intensity in bandwidth from 20 kHz to 60 kHz. The high-intensity frequency response of coil with 200 turns shift to bandwidth from 60 kHz to 100 kHz. For the 80-turn coil, the frequency response is almost flat over the whole bandwidth except some impulses related to noise.

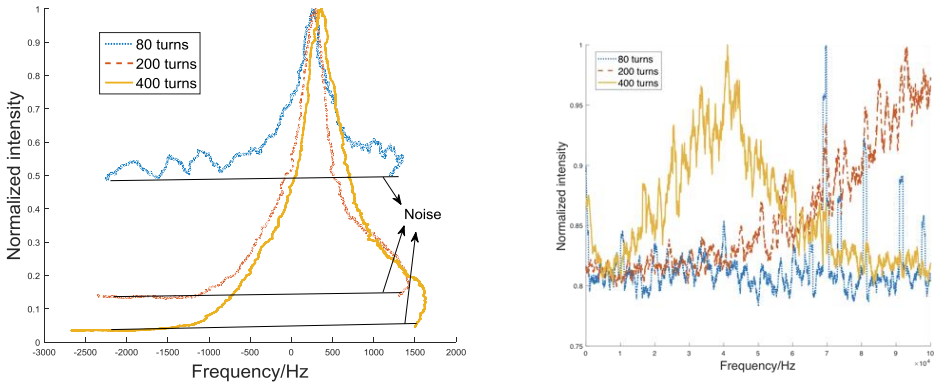

Figure 2-46 Normalized MBN profile and Normalized MBN frequency response profile

3.1 Grain size effect on MBN frequency spectrum

Grain size as a significant microstructural property have important influence on the MBN signals. Hall-Petch type relationship between the grain-size and the MBN power observed for polycrystalline iron was found. The relationship can be described as the formula MBN $= C_g \cdot {d_g}^{-1/2}$. Grain size have influence on the frequency spectrum of the MBN signal as well. The relationship between the length of the wall displacement between pinning obstacles and the local magnetic moment is described as following formula:

$$\delta\vec{m} = \vec{\beta}(\vec{S} \cdot \delta\vec{l})$$

$\vec{\beta}$ is a coefficient related to the type of domain wall and atomic magnetic moment. $\vec{S}$ is the face of moving Bloch wall. $\delta\vec{l}$ as the length between two pinning obstacles associated with microstructure morphology closely can be further expressed as $\delta\vec{l} = \vec{v} \cdot \delta t$. $\vec{v}$ is the average wall velocity and δt is the time interval between two pinned states. And then frequency content can roughly be characterized by f=1/δt.

With the decrease of the grain size, there are more pinning sets around grain boundaries. And this fact results in the short displacement length $\delta\vec{l}$ and further leads to the increase of the frequency content. Fig. 2-47 shows the frequency spectrum profile of samples. Peak positions for the frequency spectral trends have been marked in the graph. Steel 1008 with large grain size 39 μm has an obvious peak in the low frequency around 7.5 kHz. And then, the peak position of steel 1008 followed by the steel 1026, ASTM-36 and steel 1018 with grain sizes of 15 μm, 11 μm and 10 μm respectively. The similarity of the MBN spectrum profiles for the sample 1018 and ASTM 36 reveal the similarity in their grain size and microstructure.

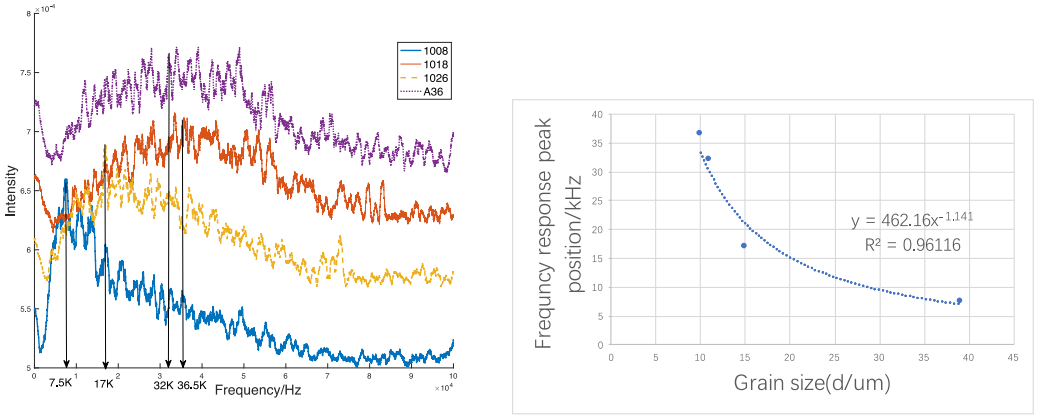

Figure 2-47 MBN frequency response profiles of samples and plot of the MBN frequency response peak position as a function of grain size

2.5.4.2. Carbon content

Profiles of MBN signal of samples 1008, ASTM-36 and 1018 in Fig. 2-48 show obvious slope changes in high magnetic field strength which can be taken as second peaks. For steel 1026, even though there is no sharp slope change from the profile, it can be explained by the reason that the second peak merged with the first one depending on the distribution of pinning strength of microstructural obstacles in response to a given range of magnetization which has been described in previous studies. For the property observed in the figure, two Gaussian curves have been used to fit two peaks in MBN profiles separately. The first peak in low magnetic field strength is related to the nucleation and annihilation of domain walls in grain

boundaries of ferrite and the second peak at higher amplitude position indicates the displacement of domain walls due to the second phase particles which are harder pearlites in samples . It is obvious that the shapes of profiles for different samples change slightly with the change of the relative position of two peaks. From (a) to (d) in Fig. 48, the gaps between two peaks (ΔG) defined as the difference of mean values of two Gaussian distributions become smaller with the increase of the carbon content. A plot of parameter ΔG and carbon content for four samples is given in Fig. 49. Most of the experimental results collected by multiple measurement lie in the 95% prediction bounds suggests that reliable of the data.

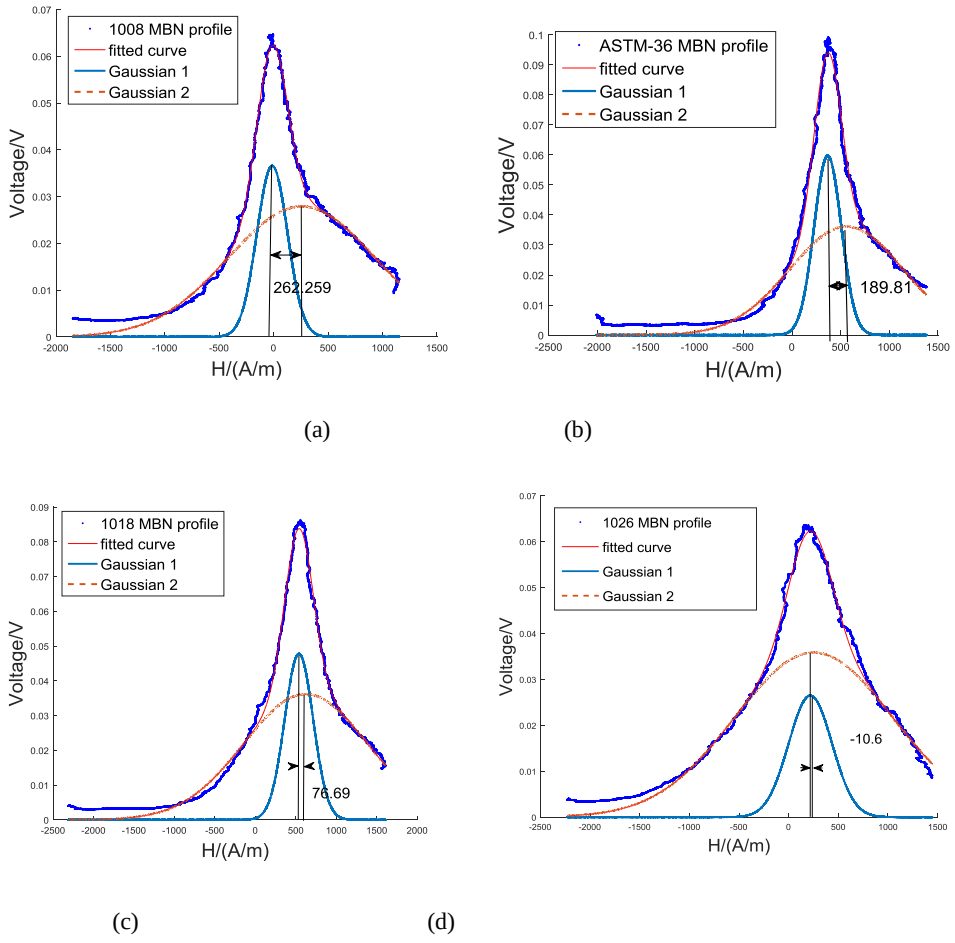

Figure 2-48 MBN profiles fitted with two Gaussian curves (a) 1008 steel (b) ASTM-36 steel (c) 1018 steel (d) 1026 steel

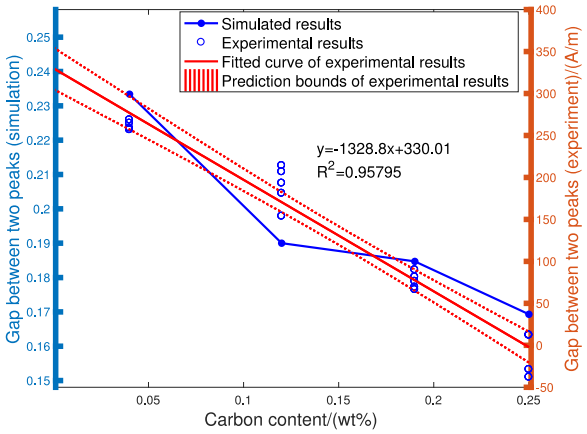

Figure 2-49 A plot of the separation between two peaks as a function of carbon content

2.6. MBN hardness measurement

Other than those parameters extracted in time domain, it is also important to study the results from the frequency response of the MBN signal, which provide a wealth of information. S. Yamaura et al. derived a new parameter, P 60 /P 3, to study the effect of grain size of pure iron specimens on the Barkhausen noise, where P 60 and P 3 are the spectrum intensities at 60 kHz and at 3 kHz respectly. M. Vashista et al. showed that the frequency response of the pick-up coils would change with the number of turns of the coil. The peaks of frequency response move to the lower frequency with the increase of the number of turns of pick-up coil. In this section, the sample has been annealed and normalized to get different microstructures to investigate and verify the relationship between the MBN frequency response and grain size and hardness of samples in the experiment. For frequency response for different samples, in contrast to the description in the previous paper that the frequency response of a pick-up coil does not change significantly with the different microstructure of test material, as grain size decreases, the position of peaks of frequency profiles increases.

2.6.1. Heat treatment of the steel

Parallelepiped samples were prepared from various types of mild steels obtained commercially, which include 1008, A36 and 1018 with different carbon contents of 0.04 wt%, 0.12 wt% and 0.19 wt% respectly. As Fig. 2-50 showing, those steels using in the experiment whose carbon contents less than 0.83% are mainly consisted with ferrite and pearlite. In order to change the microstructure of steels obtained off-the-shelf and investigate the influence of heat treatment to the Barkhausen noise signals, each kind of steels were normlized and annealed by heating the samples above the Ac3 around 50 ◦F to 150 ◦F to austenitize the original grains. The carbon contents of the samples are from 0.04 wt% to 0.19 wt %, acorrding to the Fig. 1, the corresponding austenitize tempreture are from 1600 ◦F to 1650 ◦F. Considering all the samples, we set the temperature with 1706 ◦F as show in the Fig. 2-51 (a) and Fig. 2-51 (b). The heat rate for the heat treatment also has influence on the austenitize temperature, the samples have been heated with a related slow ramp rate of 300 ◦F/ h to make sure a low austenitize temperature. To make the sample heated sufficiently, according to the thickness of the sample, the samples have been held in the temperature for one hour. The cooling rate, which is the only different between annealing process and normalizing process, is the most import procedure to control the grain size and grain phase of the steel. For annealing, the steels are cooled in the furnace with a relative slow rate of 225 ◦F / h to around 800 ◦F. This process will lead to a coarse-grain structure of the steel. The grain size will became smaller with the increase of the cooling rate. For normalizing, the samples are cooling in the air which has a relave higher cooling rate and lead to fine-grain structure. The grain phase of the steel after annealing and normalizing are still ferrite and pearlite. Whereas, martensite will present when the cooling rate increase

further, such as cooling in water or oil, which is known as quenching.Each kind of steels were normlized to get samples 1008 N, A36 N and 1018 N and annealed to get the samples 1008 A, A36 A and 1008 A with the vacuum furnace. To make the samples fully saturated, all steels were cutted into small piecies with dimensions of 100mm × 30mm × 4.76mm.

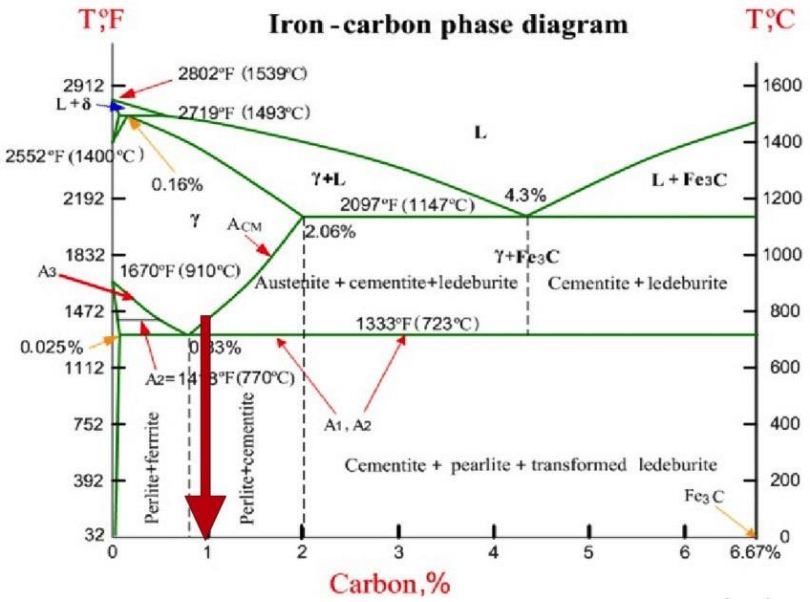

Figure 2-50 Iron carbon phase diagram

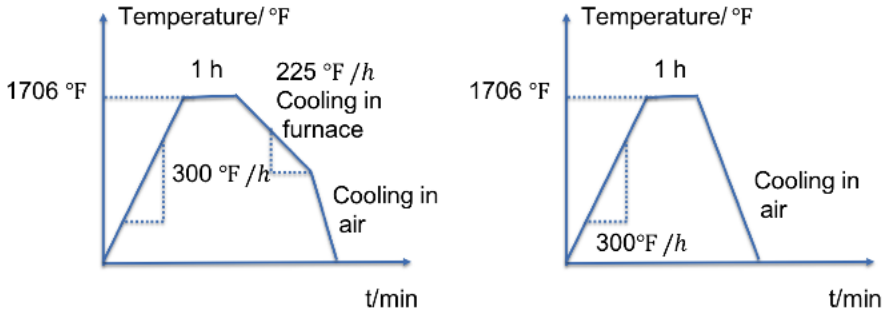

(a) annealing (b) normalizing

Figure 2-51 Heat treatment of the steel

2.6.2. Vickers Hardness Test

The Vickers hardness test method is very useful for testing on a wide type of materials, but test samples must be highly polished to enable measuring the size of the impressions. It consists of indenting the test material with a diamond indenter, in the form of a right pyramid with a square base and an angle of 136 degrees between opposite faces subjected to a load of 1 to 100 kgf. The full load is normally applied for 10 to 15 seconds. After loading, when we move the indenter away and there is a small indent under microscope. By using screw micrometer, the diagonal length can be measured accordingly.

The HV number is determined by the ratio F/A, where F is the force applied to the diamond in grams-force (gf) or kilograms-force (kgf) and A is the surface area of the resulting indentation in square micrometers mm^2 or square millimeters μm^2. A can be determined by the formula.

$$d = \frac{d_1 + d_2}{2} \tag{1}$$

$$A = \frac{d^2}{2\sin(136^\circ/2)} \approx \frac{d^2}{1.8544} \tag{2}$$

$$HV = \frac{F}{A} \approx \frac{1.8544F}{d^2}\left[\frac{kgf}{mm^2}\right] \approx \frac{1854.4F}{d^2}\left[\frac{gf}{\mu m^2}\right] \tag{3}$$

The F in equation 1 stands for the load force, which is set by yourself. The d is represented the

average of two the diagonal line of the indent. Vickers hardness values are generally independent of the test force. The Fig. 2-52(a) shows the diagram for the Vickers Hardness test and the shape of the indent. And Fig. 2-52 (b) shows the tester we are using.The micro-hardness of the samples are obtained with Vickers Hardness Tester with load 200gf . According to equation 1 and 3, we can calculate the Vickers Hardness for different samples. The tests have been conducted on every sample for five times, and the final hardness is obtained by taking average of results of five times.

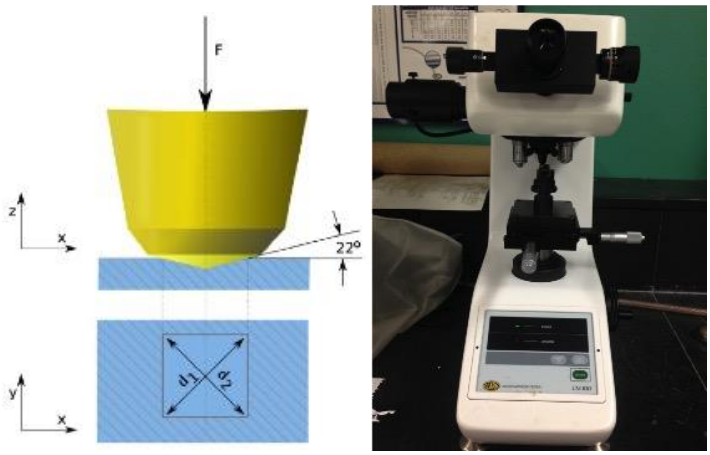

(a) (b)

Figure 2-52 The diagram for Vickers Hardness Test and Vickers Hardness Tester

2.6.3. Microstructure

To observe the microstructure on the surface of each sample, small pieces of the samples were cut and polished with diamond paste (6 μm and 0.2 μm).The metallographic structure was revealed by etching with the 4% Nital solution. Bright regions in the majority of the picture represent the ferrite grains and the dark ones spread in between are pearlite grains, which can be taken as the second phase particles. Fig. 4 shows the microstructure observed under an optical microscope with the magnification of 1000X. With the graph obtained from the microscope and the scale bar marked on the bottom right corner of the picture, we can predict the area for the whole picture. The grain number can be counted from the picture and the average grain size for ferrite grain can be calculated. The grain size, grain shape, Vickers Hardness and second phase percentage drastically changed after heat treatment. From the Fig. 2-53, we can find that the grain size for annealed sample is larger than normalized one, which is consisted with the conclusion before. And the second phase (pearlite, dark particles) proportion will change a lot during heat treatment. The details of the chemical composition, heat treatment process and microstructure are summarized in Table 4.

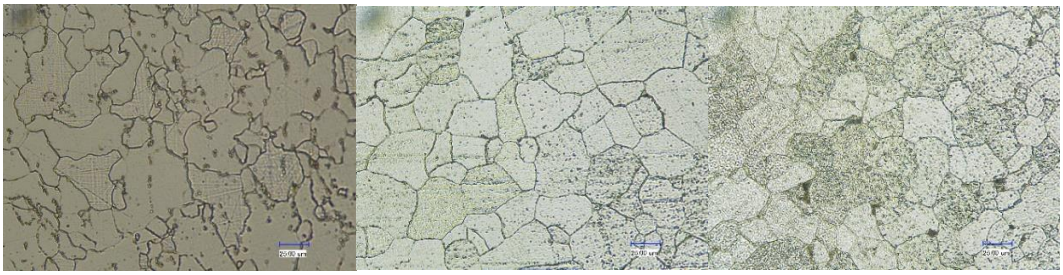

(a) 1008 (b) 1008 annealed (c) 1008 normalized

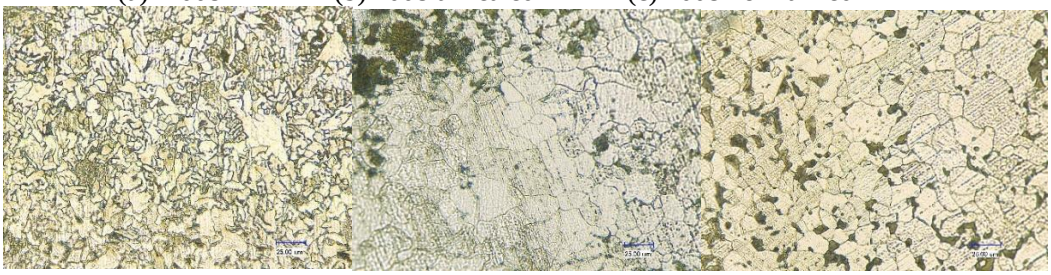

(d) 1018 (e) 1018 annealed (f) 1018 normalized

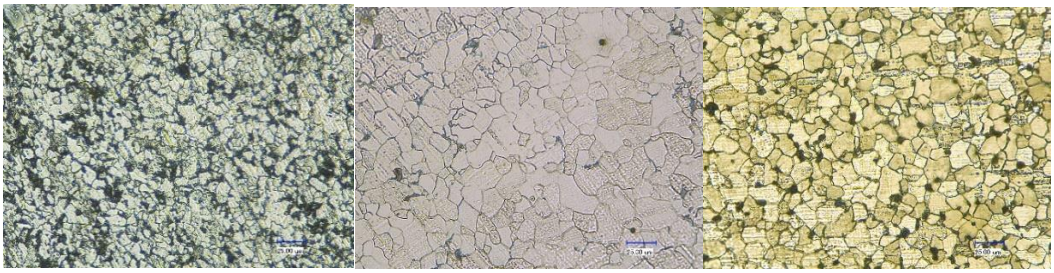

(g) A36 (h) A36 annealed (i) A36 normalized

Figure 2-53 Microstructure of steel samples with magnification of 1000X

Table 4 Carbon content, grain size, Vickers Hardness and heat treatment of steel samples

Samples	Carbon Content (CC wt%)	Grain Size (GS d/um)	Vickers Hardness	Heat treatment
1008	0.04	32	110.21	Without heat treatment
A36	0.12	11	172.19	
1018	0.19	10	185.33	
1008 A		40	95.06	Annealing: 1706◦F 1hr, 4hrs cool to 800◦F
A36 A		22.5	116.33	
1018 A		25	118.81	
1008 N		34	99.71	Normalizing: 1700◦F to 1750◦F, 1hr Cool in air
A36 N		16.5	120.7	
1018 N		22	133.43	

2.6.4. Grain size effect on MBN frequency spectrum

Grain size as a significant microstructural property has an important influence on the MBN signals. A Hall-Petch type relationship between the grain-size and the MBN power observed for polycrystalline iron was

found. The relationship can be described as the formula $MBN = C_g \cdot d_g^{-1/2}$[1]. Grain size also has an influence on the frequency spectrum of the MBN signal. The relationship between the length of the wall displacement between pinning obstacles and the local magnetic moment is described as the following formula:

$$\delta\vec{m} = \vec{\beta}(\vec{S} \cdot \delta\vec{l})$$

$\vec{\beta}$ is a coefficient related to the type of domain wall and atomic magnetic moment. $\vec{S}$ is the face of moving Bloch wall. δl is the length between two pinning obstacles associated with microstructure morphology closely, which can be further expressed as $\delta\vec{l} = \vec{v} \cdot \delta t$. $\vec{v}$ is the average wall velocity and δt is the time interval between two pinned states. Frequency content can roughly be characterized by f=1/ δt.

To simulate MBN with different Grain size, 2-D simulations have been performed on the spin lattice systems. The results have been shown below.

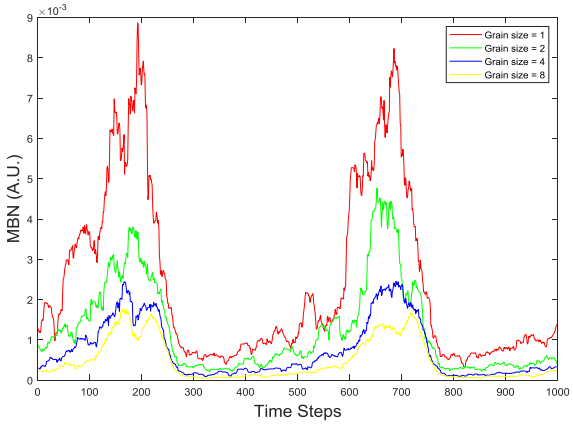

Figure 2-54 Simulated MBN profile of different grain sizes

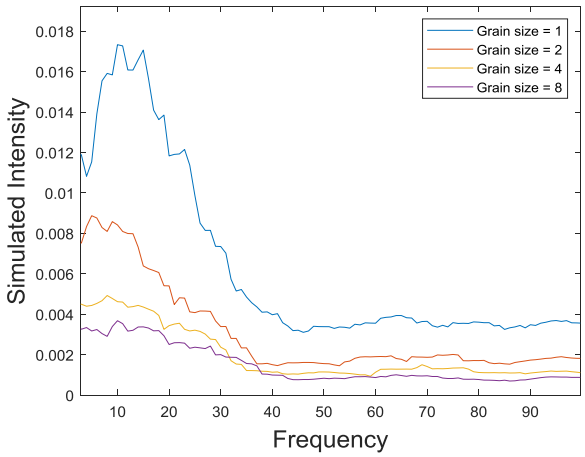

Figure 2-55 Simulated MBN frequency profiles of different grain sizes

With the decrease of the grain size, there are more pinning sets around grain boundaries and this fact results in the short displacement length $\delta\vec{l}$, which further leads to the increase of the frequency content. Fig. 2-56 shows the fitted frequency spectrum profile of samples with excitation voltage of 700 mv generated by signal generator.

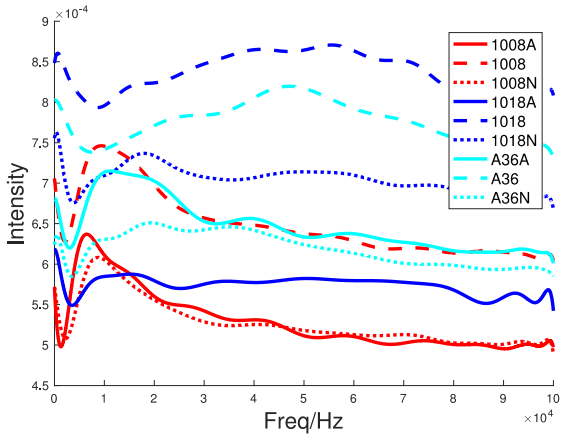

Figure 2-56 Fitted MBN frequency profiles of different samples

The lines in same color stand for the same samples with different heat treatment processes. Steel 1008 groups with large grain sizes from 32 μm to 40 μm have obvious sharp peaks in the low frequency regions. Whereas, the peak positions of steel ASTM-36 and 1018 with fine grains are moving to the high frequency ranges. From Table 4 and Fig. 2-53, the grain size for each kinds of samples with different heat treatment processes are following the same trend where samples after normalizing are larger than samples without heat treatment and smaller than samples after annealing. When we take a look at lines with the same color, the peak positions are increasing with the decrease of the grain size from annealed samples to samples without heat treatment.

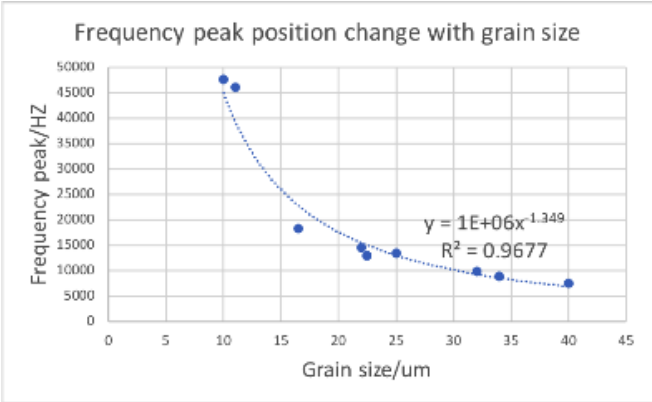

Figure 2-57 MBN frequency response peak position as a function of grain size

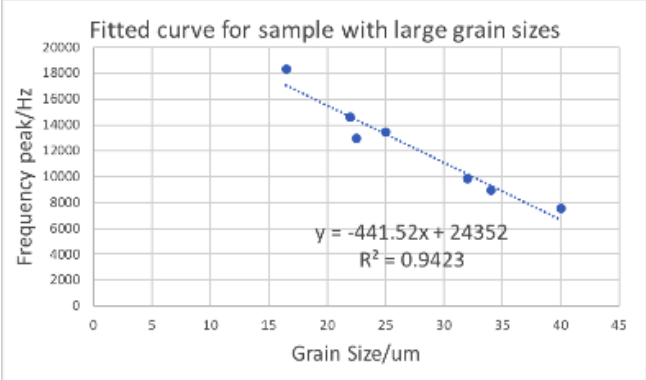

Figure 2-58 MBN frequency response peak position as a function of grain size

The relationship between grain size and main frequency content has been plotted in the Fig. 8. Each point in Fig. 2-57 is obtained by taking the average of results from multiple measurements to get reliable parameters. The relationship between grain size and frequency peak position are perfect fitted by the power function

$$Fpp = 1.0022 \cdot 10^6 \cdot Gs^{-1.349}$$

(Fpp stands for frequency peak position of MBN signal and Gs is grain size of the sample). The sensitivity of the parameter, frequency peak position, increases when the grain size of samples decreases. For those samples with fine grain, small changes in grain size will result in a large shift of the frequency peak, whereas those samples with coarse grain (larger than 15 μm), the frequency peak position has a good linearity with grain size. Fig. 7 shows the linear relationship between frequency peak position and samples with grain size larger than 15 μm.

2.6.5. Excitation signal effect on MBN frequency spectrum

It has been showed that the MBN time-domain profile will show two peaks for steels with two phase of particles when applied magnetic field is high enough. The first peak in low magnetic field strength is related to the nucleation and annihilation of domain walls in grain boundaries of ferrite and the second peak at higher amplitude position indicates the displacement of domain walls due to the second phase particles. The intensity of the second peak will increase as the applied magnetic field increases. The excitation signal also has influence on the frequency spectrum.

Previous works shows the results with excitation signal of 700 mV. When increasing the excitation signal from signal generator to 1.2 V, the frequency peak of samples normalized A36, annealed 1018 and normalized 1018 have been shifted to a higher frequency from the original position (Fig.2-57). Frequency profiles in Fig. 2-58 are from the same sample with different excitation signal amplitudes. They show two peaks for both profiles and the second peak intensity increases a lot with the increase of excitation signal. It is because that when the excitation voltage increases, the MBN signal that comes from the second phase particles, which are harder pearlites for low carbon samples, has been increased. Pearlite is a two-phased, lamellar structure composed of alternating layers of ferrite (88 wt%) and cementite (12 wt%). It usually has more pins and is difficult for magnetization. As a result, the frequency response for pearlite is in high frequency regions and this is consistent with previous works. This fact results in the increase of the second peak of the frequency profile for samples with large proportions of second phase particles. It can be further confirmed by the fact that samples normalized A36, annealed 1018 and normalized 1018 all have large proportions of second phase particles. The second peaks of the frequency spectrum are in the region from 40 kHz to 50 kHz and this overlaps with the frequency region of samples 1018 and A36. This explains why samples 1018 and A36 do not show a small frequency peak shift when excitation signal increases.

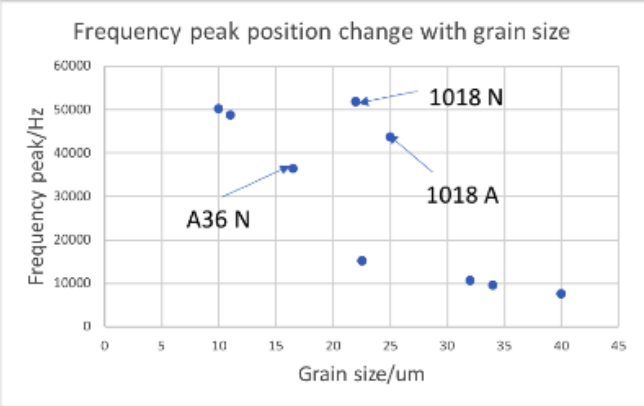

Figure 2-59 MBN frequency response peak position and grain size for each samples

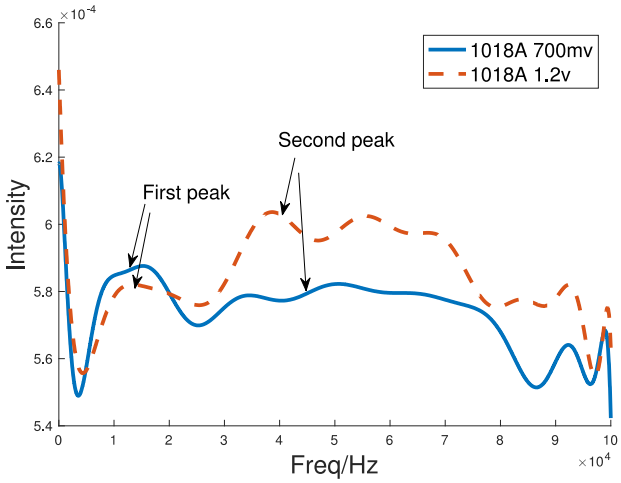

(a) 1018 annealed

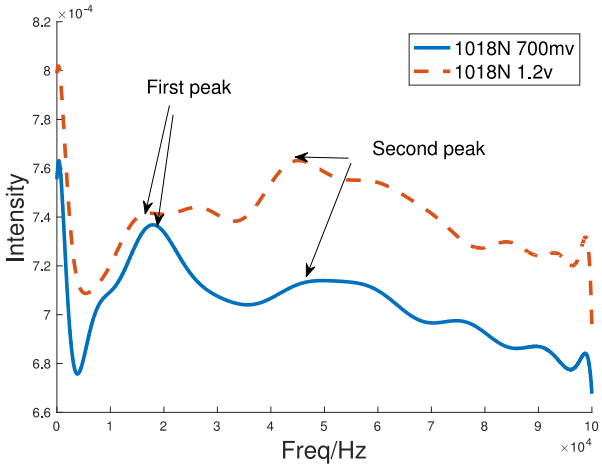

(b) 1018 normalized

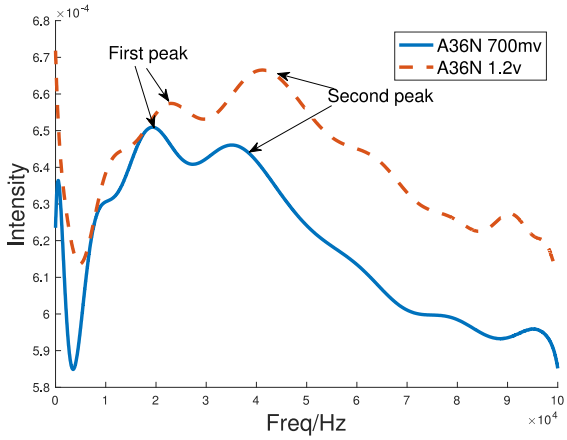

(c) A36 normalized

Figure 2-60 Fitted MBN frequency response peak profile for samples with different excitation signal

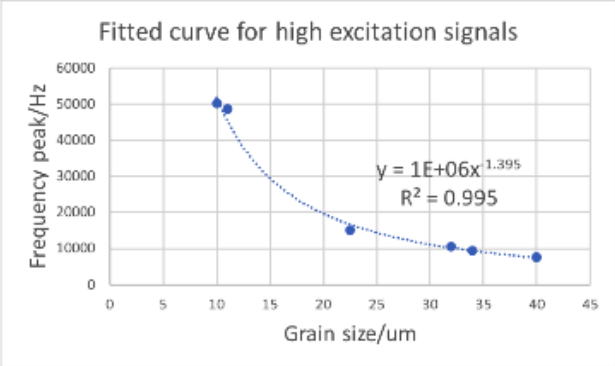

Figure 2-61 MBN frequency response peak position as a function of grain size (high amplitude excitation signal)

2.6.6. Predict hardness with parameter frequency peak position

The grain size has a strong effect on the mechanical behavior of the materials. For mild steel, the grain refinement can enhance the hardness. This grain-size dependence is described by the Hall-Petch relation.

$$H = H_0 + K \bullet Gs^{-1/2}$$

Where H_0 is the hardness of an indefinitely large, error-prone grain, and K is the Hall-Petch constant, which describes the grain boundary structure. Gs is the average grain size and H is the hardness of different kind of steel. The relationship between hardness measured by Vickers Hardness tester and grain size has been plotted in Fig. 2-60. The parameter H_0 and K can be predicted from Fig. 2-60, which are 10.237 and 531.32 respectly for mild steel.

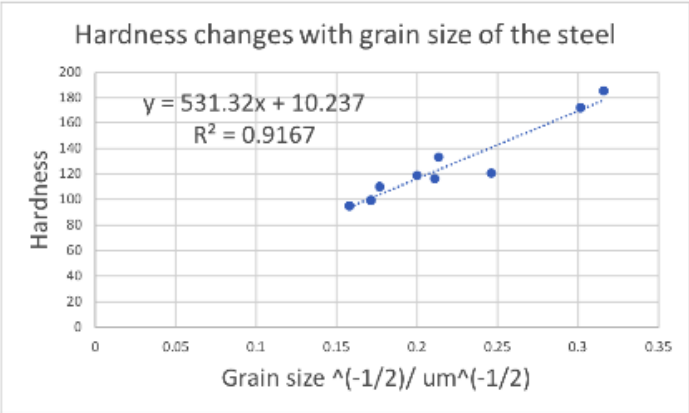

Figure 2-62 Hardness as a function of grain size

It is easy to obtain a relationship between hardness H and parameter frequency peak position Fpp. The relationship can be described as following equation:

$$H = H_0 + K \bullet (Fpp/1E + 06)^{0.371}$$

Fig. 2-63 shows values for prodicted hardness and hardness measured by Vickers Hardness Tester. The results show good accuracy for prediction and the errors are less than 10%.

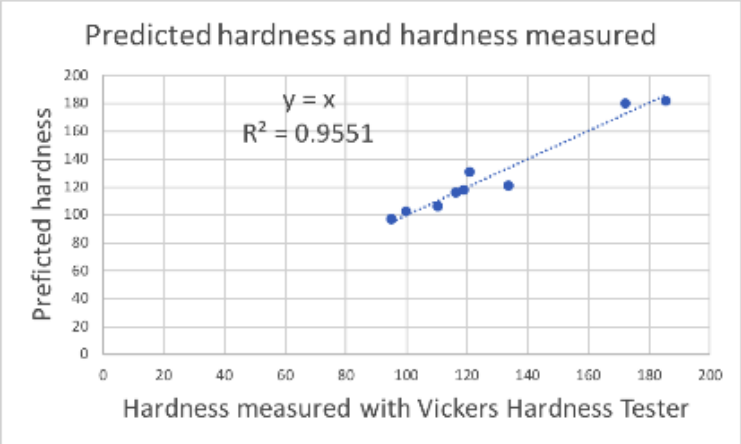

Figure 2-63 Predicted hardness and hardness measured by Vickers Hardness Tester

Table 5 Predicted hardness and corresponding error of steel samples

Samples	Vickers Hardness	Predicted hardness	Error
1008	110.21	105.99	-3.8%
A36	172.19	179.92	4.5%
1018	185.33	181.98	-1.8%
1008 A	95.06	97.08	2.1%
A36 A	116.33	116.27	-0.05%
1018 A	118.81	117.68	-0.9%
1008 N	99.71	102.72	3.0%
A36 N	120.7	130.82	8.3%
1018 N	133.43	121.05	-9.3%

2.7. Summary

MBN is a powerful tool to study and characterize microstructural properties of low carbon steels. The experimental work shows that the peaks of frequency responses of the MBN signals move to higher frequency with the decrease of grain size, which results from the decrease of the length between two obstacles with the decrease of grain size. In the experiment, the shape of profiles of MBN signals is changed with carbon content. By extracting parameter with two fitted Gaussian curves, a linear relationship has been revealed between gaps and carbon content of samples.

Sensor optimization has been introduced in the present study. Three coils with the different number of turns have been compared for sensitivity. The result shows that pick-up coils with a larger number of turns have higher SNR and are sensitive to lower frequency response.